# Numerical design and development of a probe-format graphite absorbed dose calorimeter for use in small-field radiotherapy

Benjamin Côté

Medical Physics Unit
McGill University, Montréal
October 2019

*A thesis submitted to the Faculty of Graduate Studies and Research in partial fulfillment of the requirements of the degree of Master of Science in Medical Physics*

# Table of content

# Abstract

The aim of this work is to adapt the previously developed graphite probe adsorbed dose calorimeter (GPC, a.k.a. Aerrow) to be able to perform accurate and precise dosimetry in the smallest irradiation field size used in external beam radiotherapy. Using a scaled-down version of the previous Aerrow, Aerrow-mini was designed with a cylindrical sensitive volume with a radius of 3 mm and a length of 5 mm making the volume equal to 0.146 $cm^3$. Dose deposition Monte Carlo simulations were performed to calculate $k_{Q_{clin},Q_{msr}}^{f_{clin},f_{msr}}$ and quantify the behavior at small fields. Using those results, the thermal insulating material was chosen to be the Airloy X103 at 0.4 $g/cm^3$, making the correction for small fields less than ± 1 % throughout all field sizes. After building a prototype in-house, the probe was used in isothermal mode to perform dose measurement. The shape of the probe signal was not as expected, further investigation was performed, but because of a lost connection on the heating side, the isothermal mode was disabled. Measurements were then performed using the adiabatic mode in a thermally stable environment phantom. Once again, unexpected shaped signals were measured. An alternative analysis method that uses the dose rate information to calculate the total received dose was proposed rather than the commonly used temperature offset technique. Dose measurements were performed with the Aerrow-mini and compared with an Exradin A1SL ionizing chamber with three beams: (1) 10 MV FFF beam at 2400 MU/min at 10 × 10 $cm^2$, (2) 6 MV FFF beam at 1400 MU/min at 10 × 10 $cm^2$, and (3) 10 MV FFF beam at 2400 MU/min at 2 × 2 $cm^2$. Dose difference of 0.4 %, 0.5% and 0.1 % were obtained for the beam (1), (2) and (3) respectively. Those results suggest the validity of the Monte Carlo model and the newly proposed way of isothermal analysis.

# Abrégé

L'objectif de cette recherche est d'adapter la sonde calorimètre au graphite précédemment développé (GPC, alias Aerrow) pour être capable d'effectué de façons précise et juste de la dosimétrie de petits champs en radiothérapie externe. Utilisant une version miniaturisée de Aerrow, Aerrow-mini a été conçu pour avoir un volume sensible cylindrique avec un rayon de 3 mm et une longueur de 5 mm, donnant un volume de 0.146 $cm^3$. Des simulations Monte-Carlo de déposition de dose ont été effectuées pour calculer les $k_{Q_{clin},Q_{msr}}^{f_{clin},f_{msr}}$ et quantifié le comportement en petits champs. Utilisant ces résultats, le matériau d'isolation thermique a été choisi : le Airloy X103 à 0.4 $g/cm^3$, menant à une correction pour les petits champs moins que ± 1 % pour l'ensemble des grandeurs de champs utilisés en clinique. Après avoir construit un prototype maison, la sonde a été utilisée en mode isothermal pour effectuer des mesures, mais à cause d'une perte de connexion dans un des circuits de chauffage, rendant le mode isothermique hors d'usage. D'autres mesures ont ensuite été effectuées en mode adiabatique dans un fantôme à environnement thermiquement contrôlé. Encore une fois, un signal avec une forme non attendue fut mesuré. Une méthode d'analyse alternative qui utilise l'information du taux de dose pour calculer la dose totale reçue a été proposée au lieu d'utiliser la technique commune de différence de température. Des mesures de dose ont été effectuées avec Aerrow-mini et comparées avec une chambre à ionisation Exradin A1SL pour trois faisceaux différents : (1) un faisceau à 10 MV FFF à 2400 MU/min à 10 × 10 $cm^2$, (2) un faisceau à 6 MV FFF à 1400 MU/min à 10 × 10 $cm^2$, et (3) un faisceau à 10 MV FFF à 2400 MU/min à 2 × 2 $cm^2$. Une différence de dose de 0.4 %, 0.5% et 0.1 % fut obtenue respectivement. Ces résultats suggèrent la validité du modèle Monte-Carlo et la nouvelle méthode d'analyse des signaux en mode isothermal.

# Acknowledgements

It is with the help and contribution of some people that this work was made possible and I would like to acknowledge them.

Firstly, I want to acknowledge the amazing supervision form both my supervisor Jan Seuntjens and James Renaud. Thanks for having made that project such a big learning experience. Your patient and precise insight were very much appreciated.

I would like to thank my student colleague for the great help and tip that some of them have provided. I would like to thank the clinical staff of McGill University Health Center, especially Joe Larkin and Bhaven Siva, for their help and assistance throughout the project. A warm thanks to Margery Knewstubb and Tatjana Nisic, the department secretaries, for their help with open arms.

I also would like to thank the FRQNT for providing funding for my project.

Last but not least, I would like to thank my friends and family for their endless patient, support and encouragement. I would not have done it whiteout you.

# Chapter 1 – Introduction

## 1.1. Cancer

With the constant improvement of modern medicine, we become increasingly equipped to treat disease, increasing the life expectancy as a result. Cancer is a disease that primarily affects older populations. In Canada, 89 % of new cases are diagnosed in people older than 50. Half of Canadians will get cancer in their lifetime and 1 in 4 will die from it[1]. Data has shown that through improvements to cancer treatment, the death rate is decreasing over time[1]. However, cancer is still the leading cause of death for Canadian[1], explaining the constant quest in the amelioration cancer treatments.

Cancer is not one disease, but a group of over 200 diseases. They are grouped under one word because they originate in the same way. Cancer can be described as a disease of an over-duplication of cells in which the function has partially or completely been altered. This alteration originates in the DNA code of the ill cells and can be genetic or can be induced by external factors like chemicals or ionizing radiation. A cancerous tissue often presents traits that it has lost control over its cell division rate. This loss of control can lead to the creation of a tumorous mass and can sometimes spread in the surrounding region of the body or spread further as metastases. It should be noted that some tumors are not cancerous and that there are some cancers that are not tumors. Cancer can be treated using different approaches; the main ones being surgery, chemotherapy, and radiotherapy[8].

## 1.2. Radiotherapy

Radiotherapy is the use of ionizing radiation to treat cancer. Radiation can lead to unrepairable damage in the DNA in the form of double-strand breaks that can lead to the death of the cell. In order to achieve the goal of killing the cancerous mass while minimizing the damage to healthy tissue, the delivered radiation dose needs to be known accurately. More radiation means a greater chance of killing all cancerous cells, but more radiation also means an increase in the severity of the damage to the surrounding healthy tissues.

The term radiotherapy includes many types of ionizing radiation and delivery methods. In external radiotherapy, different particles can be used, which can be grouped into two categories: directly ionizing and indirectly ionizing radiation. Directly ionizing radiation are charged particle that travel at high energy and can deposit their energy in the medium through Coulomb interactions causing ionization and excitation of the atoms. Directly ionizing radiation include electron, proton, and heavier ions. Indirectly ionizing radiation are particles that will interact with the medium, creating charged particle that deposit ionizing level of energy. For example, the photon, which is a massless uncharged particle, will interreact either through the photoelectric effect, the Compton effect or by pair production; all of which can result in the production of high energy charged particle.

Photon-based radiotherapy can be divided into categories based on the energy range. The higher the photon energy, the more penetrating the radiation. Between 10 keV and 100 keV, is referred to as the superficial X ray range, above 1 MeV is the megavoltage (MV) X ray range, and orthovoltage range lies in between those two. Superficial and orthovoltage X rays beam are commonly generated with an X-ray tube, whereas megavoltage beams

are generated by linear accelerators (linac)[2]. Megavoltage photon beams between 4 MV and 25 MV are typically used in the clinic for deeply situated tumors.

## 1.3. Dosimetry

As mentioned earlier, the amount of delivered radiation needs to be accurately known in order to treat the tumor while minimizing the side effects. This is where dosimetry plays a major role. Dosimetry is a sub-field of medical physics where the main aim is to precisely and accurately quantify the radiation dose delivered by a radiotherapy modality. The quantification of the doses plays a major role in many aspects such as machines calibration, quality assurance, patient risk assessment passing, and personnel safety.

### 1.3.1. Quantities and concepts

Before explaining how dosimetry is done in the context of radiotherapy, dosimetry quantities and concept need to be properly defined.

#### 1.3.1.1. Kerma

Kerma[2,9,10] is a quantity used to describe how much Kinetic Energy is Released per Unit MAss by indirectly ionizing radiation, such as photons. When a photon beam goes through a medium, photons will interact through different processes and deposit some or all their energy. The equation to calculate Kerma is shown below.

$$K = \int_0^{E_{\max}} \Psi_E(E) \left( \frac{\mu_{\mathrm{tr}}(E)}{\rho} \right) \mathrm{d}E \quad \left[ \frac{\mathrm{J}}{\mathrm{kg}} \right] \qquad (1.1)$$

Where $\Psi_E(E)$ is the energy fluence of the beam, and $\mu_{tr}(E)$ is the mass energy transfer coefficient, defined as the average energy transferred by photons to charged particles when passing through the medium.

When a photon deposits its energy, a portion will be transferred to electrons, which will in turn deposit the energy locally. Some energy is converted into radiation, which can be carried outside of the region of interaction. The fraction of the energy that corresponds to radiative losses is denoted by *g*. For this reason, Kerma can be separated into collisional Kerma $K_{\text{col}}$, which represents the fraction of the energy transferred to electrons, and radiative Kerma $K_{\text{rad}}$, which represents the fraction of the energy transferred to secondary photons.

$$K = K_{\text{col}} + K_{\text{rad}} \quad (1.2)$$

$$K_{\text{rad}} = g\,K \quad (1.3)$$

$$K_{\text{col}} = (1-g)\,K \quad (1.4)$$

The coefficient that represents the energy transferred to the medium is known as the mass energy transfer coefficient, $\mu_{en}$,. It follows from the equation shown below.

$$\frac{\mu_{\text{en}}}{\rho} = \frac{\mu_{\text{tr}}}{\rho}\,(1-g) \quad (1.5)$$

$$K_{\text{col}} = \int_0^{E_{\text{max}}} \Psi_E(E)\left(\frac{\mu_{\text{en}}(E)}{\rho}\right)\mathrm{d}E \quad \left[\frac{\text{J}}{\text{kg}}\right] \quad (1.6)$$

### 1.3.1.2. Absorbed dose

Absorbed dose, *D*, is define as the amount of energy imparted per unit mass by directly ionizing radiation in a finite volume[2] . The relation between Kerma and absorbed dose is

depth dependent, since an electron set in motion by a photon will on average deposit its energy at some distance within a finite range. A photon beam on the other hand will continuously deposit energy as soon as it enters a medium, setting in motion electrons. Those electrons will deposit dose over a certain range, and at those energies, it will travel towards the same direction as the photons. Because of this effect, the maximum dose will not be at the surface, but somewhere downstream where electrons build-up. The SI unit of absorbed dose is joules per kilogram, which has been defined as Gray [Gy].

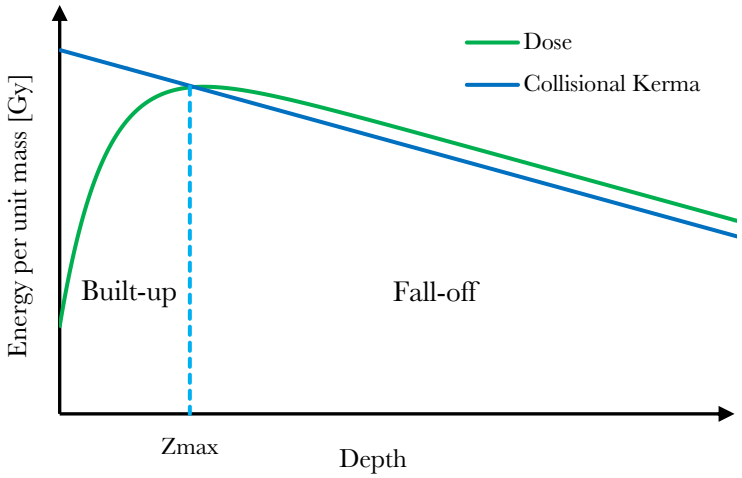


Figure 1.1: Relation between collisional kerma and dose as a function of depth showing the built-up region of the dose. Beyond the build-up region, the Dose will follow the collisional Kerma of the photons.

### 1.3.1.3. Percentage depth dose curves

As shown in figure 1.1, the absorbed dose from a MV photon beam as a function of depth has a characteristic shape: A build-up region leading to a maximum value, then a fall-off. When normalized to the maximum value, the curve in Figure 1.1 is referred to as a percentage depth dose (PDD) curve. Some points of relative interest on the PDD are the entrance dose (0 cm), the depth of the maximum dose (100 %), and the percentage dose at

a depth of 10 cm and 20 cm. These points specify information about the beam energy spectrum, or its quality, which is related to its penetrability. The quantity of interest in clinical dosimetry is dose to water because it approximates human soft tissue and is widely available in relatively pure form.

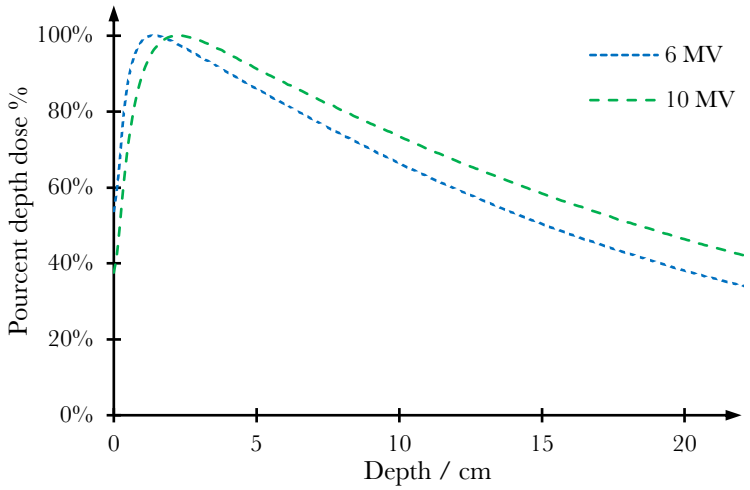


Figure 1.2: Depth dose curves for 6 MV and 10 MV beam for a square field of 10 × 10 $cm^2$. The maximum dose will happen at a depth around 1.5 cm and 2.4 cm respectively.

### 1.3.2. Radiation dosimeters

A dosimeter is an instrument that is used to measure absorbed dose through either a physical, thermal or chemical reaction, all of which have advantages and limitations. The precision and accuracy of a detector is often of central importance: Precision quantifies the repeatability of a measurement; a smaller spread in the measured quantity is associated with a higher precision, while on the other hand, accuracy quantifies the error between the measured and true value; a smaller error is associated with higher accuracy.

Dosimeters do not measure absorbed dose directly, but rather provide a measure of a surrogate quantity. For example, an ionization chamber gives a reading in coulombs, and

a radiochromic film is read out in terms of optical density. The variable used to represent detector reading is usually written as $M_{raw}$, raw specifically referring to the reading before any applied corrections, and simply $M$ when corrected. The dose absorbed by the detector in its sensitive volume can be written as $D_{det}$. The dose calibration coefficient that converts a corrected dosimeter measurement to the absorbed dose to a point in water, $D_w$, is typically written as $N_{D,w}$.[4,5]

$$N_{D,w} = \frac{D_{water}}{M} \left[\frac{Gy}{reading}\right] \qquad (1.7)$$

It is important to distinguish absolute, reference and relative dosimetry. Absolute dosimetry refers to primary standard dosimetry, where the most accurate measurements of absorbed dose are performed. Absolute dosimetry is typically done by national standard labs using one of three primary standard methods: ionometry, Fricke dosimeters, and absorbed dose calorimetry[3]. Reference dosimetry refers to the absolute measurement of absorbed dose in a clinical or hospital environment with ionization chambers that have a calibration coefficient ($N_{D,w}$) traceable to a primary absorbed dose standard. In clinics, relative dosimetry is also performed to acquire measurements relative to the reference point.

When characterizing a dosimetry system, many important parameters are considered:

- Environmental dependency refers to the sensitivity of the response to environmental variables such as temperature, pressure or humidity.
- Dose-rate dependency refers to the dependence of the dosimeter response to changes in absorbed dose rate.
- Linearity refers to the relationship (ideally directly proportional) between the dosimeter response and the imparted energy from absorbed dose.

- Energy dependence refers to the effect that a change in the energy spectrum will have on the response of the dosimeter.
- Directional dependence refers to the effect that a change in detector orientation will have on the response of the dosimeter.
- Spatial resolution and physical size refer to the spatial dependency of the detector. The physical size of the sensitive volume of the detector will largely determine the spatial resolution. The spatial resolution is the smallest distance over which the detector can resolve a difference in input signal.
- Usability refers to the ease of use of the dosimeter as well as the user dependency.

### 1.3.3. Primary absorbed dose to water standards

As mentioned previously, primary absorbed dose standards are developed and maintained by national metrology institutes (NMIs) and provide absolute readings of absorbed dose to water with the lowest achievable uncertainty[3]. In order to achieve a high accuracy, primary standards rely on quantities that are well understood and can be well characterized, and where the measuring device will have a known perturbation on the measurand. At present, there are three different accepted dose standards for MV photon beams: absorbed dose calorimetry, Fricke dosimetry, and ionometry. All three have a general relation to absorbed dose to water, as shown in the following equation:

$$D_w = c_d \, R_d \, f_{w,d} \qquad (1.8)$$

Where $D_w$ is the dose to water, $R_d$ is the detector reading, $c_d$ is the dose calibration coefficient, and $f_{w,d}$ is the dose conversion factor from the detector volume to water.[3]

#### 1.3.3.1. Absorbed dose calorimetry

Absorbed dose calorimeters operate on the principle that energy imparted by ionizing radiation in a medium will generate a rise in temperature, according to the idealized equation 1.9.

$$D_m = c_{p,m}\,\Delta T_m \qquad (1.9)$$

Where $c_{p,m}$ is the specific heat capacity at a constant pressure of the medium and $\Delta T_m$ is the rise in temperature. At present, absorbed dose calorimetry is most often done using water or graphite as the absorber[3]. Water calorimetry is used because no dose conversion factor is needed and because of the low diffusivity of water, making it possible to obtain point measurements. On the other hand, accurate water calorimetry requires that a number of correction factors be taken into account: (i) the heat defect, $k_{hd}$, that corrects for heat losses or gains due to radiation induce chemical reactions, (ii) the heat dissipation, $k_h$, that corrects for heat loss due to conduction and convection, (iii) the radiation field perturbation, $k_p$, that account the effects of the presence of non-water material in proximity to the measuring volume, (iv) the dose profile non-uniformity, $k_{dd}$, that correct for any non-uniformity in the dose profile, and (v) the density, $k_\rho$, that account for the difference in density of the water between the operating temperature and the reference temperature of 295.15 K.

$$D_{\mathrm{w}} = c_{\mathrm{w,p}}\,\Delta T\; k_{\mathrm{hd}}\; k_{\mathrm{h}} k_{\mathrm{p}} k_{\mathrm{dd}} k_\rho \qquad (1.10)$$

Graphite calorimetry is also widely used and differs from water calorimetry in a number of important ways: Graphite is solid, has a specific heat capacity almost six times smaller than water and has a thermal conductivity coefficient almost six hundred times greater than water. Graphite calorimeter designs often include heating elements allowing measurement

to be acquired in alternative modes of operation (e.g., quasi-adiabatic mode and isothermal mode).[3] The functioning of these two modes will be explained in greater detail in the next chapter.

#### 1.3.3.2. Fricke dosimetry

Fricke dosimetry relies on the change in optical density of a ferrous sulfate solution to determine the dose absorbed. When irradiated, ferrous ions $Fe^{2+}$, are transformed into ferric ions, $Fe^{3+}$, due to an oxidation chemical reaction. Using a spectrometer at a specific wavelength, the quantity of ferric ions can be measured with a precision better than 0.2% in the radiotherapy dose range[3]. The equation below shows how absorbed dose to water is measured using Fricke dosimeter.

$$D_{\mathrm{w}} = \frac{1}{\varepsilon G_{\mathrm{Fe}^{3+}}} \frac{\Delta OD}{\rho l} f_{w,F} \qquad (1.11)$$

Where $\Delta OD$ is the change in optical density, $\rho$ is the density of the solution, $l$ the light pathlength, and $f_{w,F}$ the conversion factor which is almost unity because the solution is water-based. $\varepsilon G_{\mathrm{Fe}^{3+}}$ is the radiation chemical yield constant and can be measured using calorimeters for comparison. The latter constant has a small energy dependence: it varies by 0.7 % ± 0.3 % between $^{60}$Co and 20MV photons. Determining this value accurately is fundamental for Fricke dosimetry.

#### 1.3.3.3. Ionization chamber

The Bureau International des Poids et Mesures (BIPM) has a thick wall parallel plate ionization chamber dose standard (more on ionization chamber is presented in the next section). Knowing precisely the geometry of the chamber and the air volume inside the

chamber, it is possible to calculate an accurate dose, and therefore use it as a primary dose standard. The dose is calculated using the accepted value of $(W/e)_{air}$ and by applying the proper correction factors. Dose to water is related using the following equation:

$$D_{w} = \left(\frac{W}{e}\right)_{air} \frac{Q}{m_{air}} s_{c,air} k_{p} \qquad (1.12)$$

Where $(W/e)_{air}$ is the mean energy to produce an ion pair in air, Q is the collected charge, $m_{air}$ is the mass of air, $s_{c,air}$ is the electron stopping power ratio between the wall composition and air, and finally $k_{p}$ is the cavity correction factor that correct for the presence of the chamber walls.

### 1.3.4. Clinical dosimetry systems

Only clinical dosimeters pertaining to the thesis project will be presented, hence this is not an exhaustive list of clinical dosimetry systems.

#### 1.3.4.1. Ionization chamber

Ionization chambers are the most widely used dosimeters in the radiotherapy clinic. They can be used for both reference dosimetry and relative dosimetry. Ionization chambers are essentially a closed volume of air and two electrodes with an electrical potential applied between them. When radiation passes through the air in the chamber, it creates ions, which are then accelerated along the electrical potential towards the electrodes that collect them. Ion chambers come in a variety of geometries and volumes. A bigger volume will generate a greater signal but will also have a greater volume averaging effect and lower spatial resolution. The two most common types of ion chambers are the cylindrical thimble chamber and the flat parallel plate chamber.

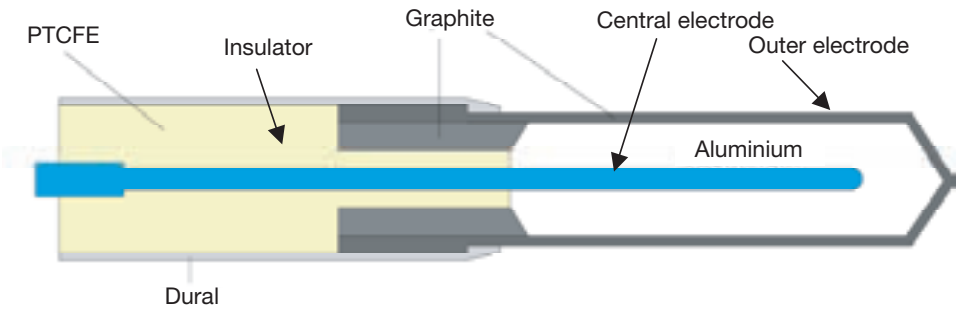


Figure 1.3: Schematic representation of a cylindrical thimble ionization chamber.[7] (Reproduction permission granted by the IAEA)

When doing clinical reference dosimetry, several correction factors are required to be applied to the raw ionization chamber reading, as recommended in clinical dosimetry protocols[4,5]:

$$M = M_{\text{raw}}\, P_{\text{TP}} P_{\text{ion}} P_{\text{pol}} P_{\text{elec}} P_{\text{leak}} P_{\text{rp}} \qquad (1.13)$$

Where,

$M_{\text{raw}}$ is the raw measurement

$P_{\text{TP}}$ corrects for the change in density of the air in the chamber; it corrects for pressure and temperature changes relative to the standard condition.

$P_{\text{ion}}$ corrects for ion recombination effects. It can be quantified by comparing measurement at two different voltages.

$P_{\text{pol}}$ corrects for polarity effects. It can be quantified by comparing measurement at two opposite voltages.

$P_{\text{elec}}$ corrects for any differences in sensitivity between the electrometer that was used for the measurement and the one that was used for calibration.

$P_{\text{leak}}$ corrects for leakage current that occurs when all the equipment is on, but there is no beam.

$P_{\text{rp}}$ corrects for non- uniformity and flatness of the radial beam profile.

#### 1.3.4.2. Diamond detectors

Diamond detectors are, as the name suggests, made of a small diamond[11]. When a voltage is applied across the crystal, a current is measured when irradiated. Because of the small size of the sensitive volume, this detector is well suited for small field relative dosimetry.[2] The sensitive volume of the commercially available microDiamond detector (PTW & model number) is a disc of 1 μm thick and a diameter of 2.2 mm. Because of its tissue-equivalent composition, it exhibits very little energy dependence.

## 1.4. Small field dosimetry

### 1.4.1. Definition of a small field

In order to investigate small field dosimetry, it must first be defined: A field is considered small when one of the three following condition is met[6]:

1) There is a loss in lateral charged particle equilibrium (LCPE) on the beam central axis.
2) There is partial occlusion of the primary photon source on some part of the field made by the collimation.
3) The size of the detector is relatively big compared to the field size.

### 1.4.2. Physics of small field

When dealing with small fields several challenges arise because of both physical and technical reasons. At a specific energy, electrons will have a certain range both in the parallel and perpendicular orientation of the beam axis. In a broad beam and deeper than the build-up region, points on the central axis will have both Transient Charged Particle

Equilibrium (TCPE) and LCPE. As the field gets smaller, there will be a point where LCPE is lost. In order to have a better understanding of at which field size that occurs, we can look the lateral charged particle equilibrium range ($r_{\mathrm{LCPE}}$) which represent the small radius of a circular photon beam where LCPE is achieved on the central axis at a certain depth and energy. When losing LCPE correction, non-water material will behave differently relative to water, then making dosimetry harder and affecting the detector response[12].

Also, by reducing the field size, the penumbra portion of the total field will increase until the field is solely composed of overlapping penumbrae. This is due to the finite size of the photon source. By extension, this results in a non-flat beam profile, further complicating the dosimetry. The figure below illustrates this effect. Reducing the field to such a small size reduces the beam output and will influence the energy spectrum of the beam. It is also important to point-out that miss-alignments of the detector will have a larger relative effect on the measurement given the steep gradients.

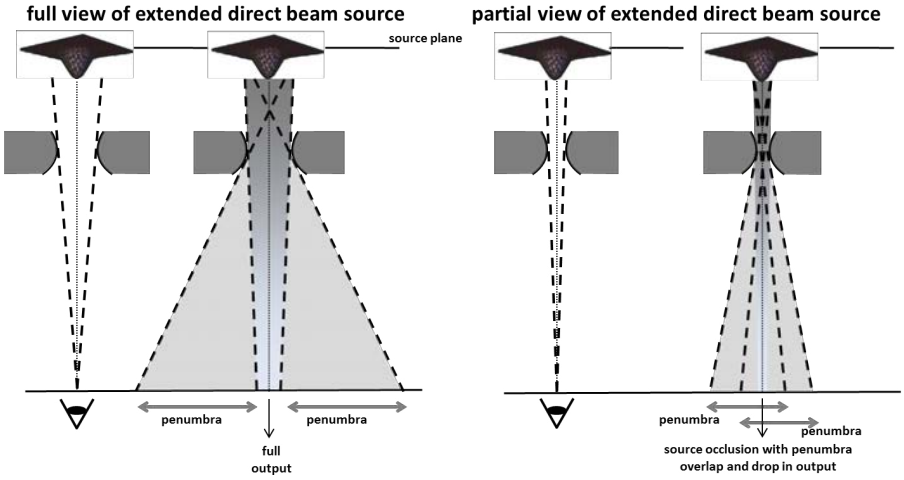


Figure 1.4: Schematic representation of the effect of partial occlusion of the finite size of the primary photon source. (Reproduction permission granted by the Institute of Physics and Engineering in Medicine 2010. IPEM Report 103 Small Field MV Photon Dosimetry[6])

The third condition that makes a field small is when the detector is large compared to the field. Since the detector averages over its sensitive volume, substantial error can be introduced, as shown in the figure below.

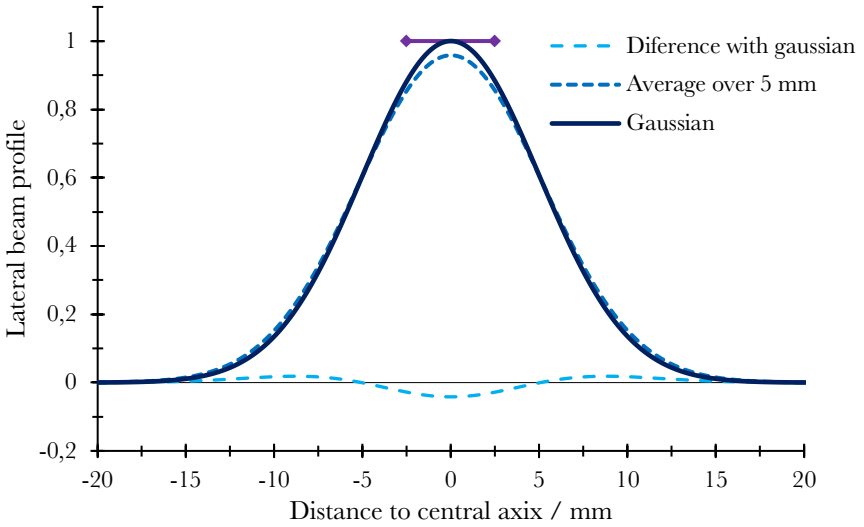


Figure 1.5: Graph showing the effect of volume averaging on a gaussian ($\sigma$ = 5 mm) curve that would have been average over 5 mm.[6]

Also, in smaller fields, when LCPE is lost, the fluence perturbation made by the presence of the detector will be greater and more difficult to model because small inaccuracy will have a greater impact[12]. All of these effects make dosimetry in small field more challenging, and less accurate if no special measures are taken such as beam scanning for alignment and volume averaging correction.

### 1.4.3. Definition of field size

In radiotherapy, field size can be defined in two different way:

1) Geometrical field size is defined as the projection on a plane perpendicular to the beam axis defined by the collimation of the machine.

2) Physical field size is defined as an isodose line in the field on a plane perpendicular to the beam axis.

In general, these two concepts are often confounded or not explicitly defined. This is usually not an issue because they usually agree quite well with each other for large fields. In broad beams, the geometrical field size is equal to the full width half maximum (FWHM) at isocenter, therefore is not very common to have an explicit measurement of the physical field size. When going to smaller fields this assumption cannot be made. Because of conditions 1 and 2 listed in section 4.1, geometrical and physical field sizes are not equivalent, and therefore need to be specified. Physical field size is typically broader than the geometrical field size, and the difference increases as the field size is reduced.

### 1.4.4. Correction factors

As explained in the previous section, when using a detector in smaller fields, some effects will become more pronounced and therefore require corrections to permit an accurate dose measurement. In order to quantify those small field effects, the following formalism was proposed to correct for the detector perturbation[6].

$$\Omega_{Q_{\text{clin}},Q_{\text{msr}}}^{f_{\text{clin}},f_{\text{msr}}} = \frac{D_{\text{w},Q_{\text{clin}}}^{f_{\text{clin}}}}{D_{\text{w},Q_{\text{msr}}}^{f_{\text{msr}}}} = \frac{M_{Q_{\text{clin}}}^{f_{\text{clin}}}}{M_{Q_{\text{msr}}}^{f_{\text{msr}}}} k_{Q_{\text{clin}},Q_{\text{msr}}}^{f_{\text{clin}},f_{\text{msr}}} \qquad (1.14)$$

Where,

- $\Omega$ is the output factor, it represents the ratio of the dose from a specific setup and a reference beam.
- $D$ is a dose.

- $M$ is a measurement made by a detector.
- $k$ is the correction factor.
- $f$ is the field size, it can be defined either as the geometrical or physical provided it's specified.
- $Q$ is the beam quality
- "clin" refers to the clinical beam condition, where our interest is a small field
- "msr" refers to the machine specific reference condition, where for a standard linac is a 10 x 10 field at SSD 100 at a depth of 10 cm.
- "w" refers to a point of water in water

Consequently, $\Omega_{Q_{\text{clin}},Q_{\text{msr}}}^{f_{\text{clin}},f_{\text{msr}}}$ is the output factor for a clinical field with a clinical beam quality. It is a general concept that can be applied for any beam on any machine that has a machine specific reference condition defined.

Therefore, all the corrections for a specific detector at a specific field size are included in the $k_{Q_{\text{clin}},Q_{\text{msr}}}^{f_{\text{clin}},f_{\text{msr}}}$ factor. This factor can be either measured experientially or calculated with a Monte Carlo technique using the equation shown below.

$$k_{Q_{\text{clin}},Q_{\text{msr}}}^{f_{\text{clin}},f_{\text{msr}}} = \frac{D_{\text{w},Q_{\text{clin}}}^{f_{\text{clin}}} \Big/ \bar{D}_{\text{det},Q_{\text{clin}}}^{f_{\text{clin}}}}{D_{\text{w},Q_{\text{msr}}}^{f_{\text{msr}}} \Big/ \bar{D}_{\text{det},Q_{\text{msr}}}^{f_{\text{msr}}}} \qquad (1.15)$$

1.5. Reference


1. Canadian Cancer Society's Advisory Committee on Cancer Statistics. Canadian Cancer Statistics 2017. Toronto, ON: Canadian Cancer Society; 2017. Available at: cancer.ca/Canadian-Cancer-Statistics-2017-EN.pdf (accessed 31-05-2019).

2. Podgorsak, Ervin B. "Review of radiation oncology physics: a handbook for teachers and students." Vienna, International Atomic Energy Agency. Educational reports series (2003).

3. Seuntjens, Jan, and Simon Duane. "Photon absorbed dose standards." Metrologia 46.2 (2009): S39

4. Almond, Peter R., et al. "AAPM's TG-51 protocol for clinical reference dosimetry of high-energy photon and electron beams." Medical physics 26.9 (1999): 1847-1870.

5. McEwen, Malcolm, et al. "Addendum to the AAPM's TG-51 protocol for clinical reference dosimetry of high-energy photon beams." Medical physics 41.4 (2014).

6. Andreo, Pedro. "The physics of small megavoltage photon beam dosimetry." Radiotherapy and Oncology 126.2 (2018): 205-213.

7. International Atomic Energy Agency, IZEWSKA, J. and RAJAN G., "Radiation dosimeters", Radiation Oncology Physics, A Handbook for Teachers and Students, IAEA, Vienna (2005) 71–100.

8. American Cancer Society. Cancer Treatment & Survivorship Facts & Figures 2019-2021. Atlanta: American Cancer Society; 2019

9. Siebers, J., & Hugo, G., "Basic Radiation Interactions, Definition of Dosimetric Quantities, and Data Sources", in Clinical Dosimetry Measurements in Radiotherapy, edited by D. W. Rogers and J. E. Cygler (Medical Physics Publishing, Madison, USA, 2009).

10. Renaud, J. (2012). Development of a graphite probe calorimeter for absolute clinical dosimetry : Numerical design optimization, prototyping and experimental proof-of-concept (Doctoral dissertation, McGill University, 2012). McGill University Libraries.

11. Vatnitsky, S., and H. Jarvinen. "Application of a natural diamond detector for the measurement of relative dose distributions in radiotherapy." *Physics in Medicine & Biology* 38.1 (1993): 173.

12. Seuntjens, S., et al. "ICRU report 91. Prescribing, recording, and reporting of stereotactic treatments with small photon beams." *Journal of the ICRU* 14 (2014): 2.

# Chapter 2 – Absorbed dose calorimetry

## 2.1. Theory

Absorbed dose calorimetry is one of the most direct ways to measure dose in radiotherapy. It based on the assumption that all energy imparted by ionizing radiation will ultimately result in a rise in temperature. The rise in temperature will primarily depend on the specific heat capacity of the absorbing materials. There are different modes in which a calorimeter may be operated; the two modes covered in this work are referred to as quasi-adiabatic and isothermal.

There are mainly two materials used to perform calorimetry, water and graphite, and the technical aspects differ in each case. Water calorimetry can only be done using the quasi-adiabatic mode of operation, whereas graphite calorimetry can be used in both quasi-adiabatic and isothermal modes. The benefit of using water calorimetry is that there is no need for a dose conversion factor because the sensitive volume material is also water. It is typically done using thermistors placed in an inert vessel (commonly quartz or borosilicate glass) filled with high purity water. The contained water is saturated with a specific gas by bubbling in order to control the radiation-induced chemical reactions that occur in the water. Graphite calorimeter comes in different designs, but they all have a graphite sensitive volume (i.e., core) that is thermally isolated from the surrounding environment; this is usually achieved by layering graphite pieces with thermally insulating material. The addition of heating elements are required for isothermal operation. Graphite is chosen because of its availability in pure form, its atomic number, which is similar to water, its relatively low specific heat capacity, and because it has a high thermal conductivity coefficient (usually between 10 to 500 $W \cdot m^{-1} \cdot K^{-1}$)[7].

### 2.1.1. Quasi-adiabatic mode

The quasi-adiabatic mode can be thought of as a passive mode of operation, since the calorimeter effectively acts as a very sensitive thermometer. The sensitive volume of the calorimeter must be placed within an environment in which the temperature is drifting at a rate less than the magnitude of the signal of interest. For high energy photon beams, the signal is typically on the order of 1 mK (for a dose rate of 4 Gy/min, water would rise by approximately 0.95 mK/min, and graphite 5.6 mK/min). When irradiated, a change in the slope of the temperature over time curve will be observed. By accounting for the background drift and measuring the temperature rise, the absorbed dose can be calculated using the following equation:

$$D_{\text{det}} = c_p \, \Delta T_{\text{core}} \prod_i k_i \qquad (2.1)$$

Where $D_{\text{det}}$ is the absorbed dose in the calorimeter, $c_p$ is the specific heat capacity of the medium at constant pressure, and $\Delta T$ is the temperature rise. The figure below illustrates a generic quasi-adiabatic run.

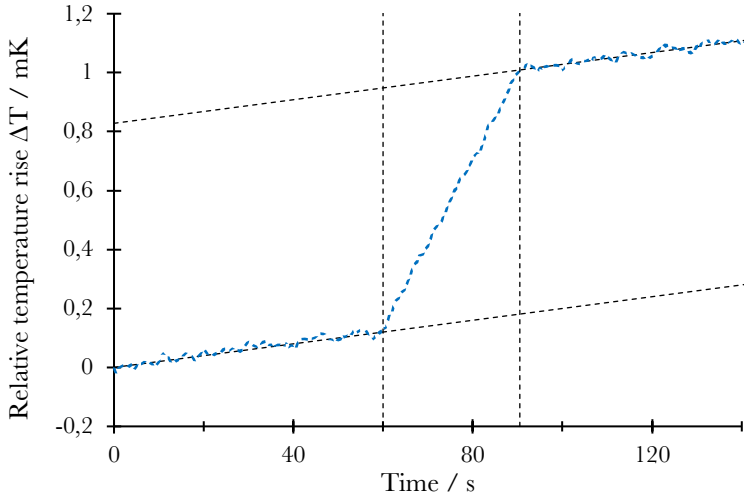


Figure 2.1: Example of a quasi-adiabatic run in water. The curve shows a drift in temperature 0.12 mK/min and the signal shows a temperature rise of 0.828 mK resulting in a dose of 3.48 Gy when using the value of 4204 J $kg^{-1}$ $K^{-1}$ for the specific heat capacity.

### 2.1.2. Isothermal mode

The isothermal mode can be considered an active mode because it uses process-controlled heating to maintain a constant temperature in each graphite layer of the calorimeter. By keeping the temperatures constant, even during the irradiation, absorbed dose can be determined by measuring the electrical power dissipated in the core. When the calorimeter is irradiated, a drop in electrical power necessary to maintain a stable temperature is observed, and this drop is directly proportional to the dose rate absorbed in the sensitive volume. Isothermal-based dose measurement can be described by the following equations:

$$\dot{D}_{\text{core}} = \frac{1}{m_{\text{core}}} \Delta P_{\text{core}} \quad (2.2)$$

$$D_{\text{core}} = \frac{1}{m_{\text{core}}} \int \Delta P_{\text{core}}(t)\ dt \quad (2.3)$$

Where $D$ is the absorbed dose, $m$ is the mass of the sensitive volume, and $\Delta P$ is the power level difference between when the beam is on and off. The figure below depicts a generic isothermal run.

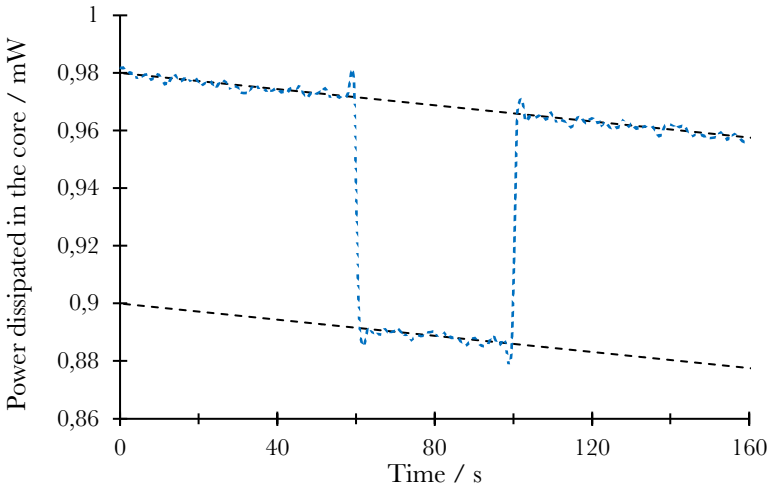


Figure 2.2: Example of an isothermal run showing the power dissipated in the sensitive volume as a function of time. The graph is depicting a drop-in power of 0.08 mW during the 30 s irradiation. For a 400 mg sensitive volume, the corresponding dose rate would be 12 Gy/min.

## 2.2. Heat transfer

Performing accurate calorimetry requires an understanding of the mechanics of heat transfer. There are three different pathways for heat transfer, each with different characteristics, but in all cases, the direction of flow follows the temperature gradient from high to low.[1]

Conduction is the mode of transfer that can dissipate heat through a substance without movement at the macroscopic level. Conduction requires a medium and can occur in both fluid and solid. Thermal agitation diffuses through the medium by molecular collision. The rate of conduction is always proportional to the temperature difference between the two points. In a uniform medium, the rate of conduction $\dot{q}$ will depend on the temperature gradient $\Delta T$ and the thermal conductivity $k$:

$$\dot{q} = -k\,\Delta T \quad \left[\frac{W}{m^2}\right] \qquad (2.4)$$

On the other hand, convection can only occur in fluids. Most of the time, it is the main mode of heat transfer in fluids. Convection can be thought of as heat displacement by the motion of the fluid. It can occur naturally due to the density gradient in a fluid or it can be forced using an external source of motion. Convection can be very difficult to model because of its complexity and chaotic behavior. Convection may be modeled in some relatively simplistic cases, for instance, the heat exchange between a fluid next to a surface: the heat exchange $\dot{q}$ will depend on the temperature of the surface $T_s$ and the fluid $T_f$, and a heat transfer coefficient $h$.

$$\dot{q} = h\left(T_s - T_f\right) \quad \left[\frac{W}{m^2}\right] \qquad (2.5)$$

The third and last mode of heat transfer is radiative. This mode of heat exchange is made by any material and is the only mode that can transfer heat without a medium, meaning that it can happen even under vacuum. The importance of this phenomena strongly depends on the temperature, $T$, as the equation (6) shows. The Stefan–Boltzmann law describes the total power emitted, $E$, by a body, which will depend on its temperature, the emissivity of its surface, $\varepsilon$, and the Stefan–Boltzmann constant, $\sigma$.

$$E = \varepsilon \sigma T^4 \quad \left[\frac{W}{m^2}\right] \qquad (2.6)$$

The emissivity is a number between 0 and 1 that describe how close to a perfect blackbody the medium is (1 being an ideal black body). Stefan–Boltzmann constant is derived from Planck's law and is equal to $5.67 \times 10^{-8}$ W m$^{-2}$ K$^{-4}$.

## 2.3. Measurements

### 2.3.1. Temperature sensing

For temperature sensing in absorbed dose calorimetry, thermistors are usually chosen. They are highly sensitive to temperature changes, and thus provide precise measurements. For a thermistor with a coefficient around 1000 Ω/K, accuracy on the order of μK can be achieved. Also, they are available in sub-mm sizes, making them ideal when it comes to reducing the effect of foreign material (i.e., impurities) in the calorimeter assembly. Thermistors calibration will be covered in the following section.

In order to measure the temperature rise in a calorimeter, a measurement of the thermistor resistance is required. This task is accomplished using a DC Wheatstone bridge and nanovoltmeter (Keithley 2182A) in this work. A Wheatstone bridge is an electrical circuit

made up of four resistive elements, R1, R2, R3, and Rx, and a constant potential, Vs, as shown in the figure below.

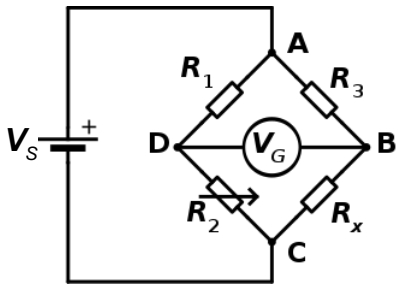


Figure 2.3: Wheatstone bridge circuit diagram[4]. The sensing thermistor would be placed at the $R_x$ position. A nanovolt meter would be used to measure $V_G$.

When $R_1$ and $R_3$ are equal, and $R_2$ set to approximately the value of $R_x$, a small change in the value of $R_x$ will "unbalance" the bridge and result in a change in the value of $V_G$. $V_G$ is the voltage across the bridge and, in this work, is measured by a nanovoltmeter. The value of $V_G$ is related to the resistances through the equation below.

$$V_G = \left(\frac{R_2}{R_2 + R_1} - \frac{R_x}{R_x + R_3}\right) V_s \qquad \Rightarrow \qquad R_x = \frac{R_2 \cdot V_s - (R_1 + R_2) \cdot V_G}{R_1 \cdot V_s + (R_1 + R_2) \cdot V_G} R_3 \qquad (2.7)$$

When the thermistor is placed on the position of $R_x$, an adjustable resistance is placed on the position of $R_2$ and a nanovoltmeter is used to measure $V_G$, a precise measurement of the thermistor resistance can be achieved. Is by combining that precise resistance reading with an accurate temperature-resistance calibration that the temperature can measurement with high precision and accuracy.

### 2.3.2. Calibration

In this work, temperature rise is related to thermistor resistance via a two-step calibration method. The first step is to calibrate one or more resistance temperature detectors (RTDs)

against a mercury thermometer with a calibration traceable to national standards in a thermally-controlled fluid bath. RTDs are like thermistors in that they are thermally sensitive resistors, but they are relatively less sensitive to temperature than thermistors. Calibration is performed by stepping through a relatively wide temperature range (approximately ±15 °C about the calorimeter operating temperature). Measured RTD resistances as a function of temperature over this range is fit with a 2rd degree polynomial.

Once the RTDs are calibrated, the same temperature-controlled bath can be used to calibrate the thermistors. As before, resistance measurements of both the thermistors and RTDs are made while stepping through a range of temperature centered about the operating temperature of the calorimeter. Again, by using a fit on the calibration points, but this time with an 4th degree polynomial, thermistors resistance can be accurately related to temperature.

### 2.3.3. Signal analysis

The signal of interest in the quasi-adiabatic mode is the temperature of the core over time. In order to determine absorbed dose, the first step of the signal analysis is to fit and extrapolate both the pre- and post-drifts toward the midpoint of the irradiation. The temperature rise is then determined by taking the difference between the two extrapolated fits at the midpoint of the irradiation. This temperature difference, along with the specific heat capacity, can then be used to determine the absorbed dose. Using this method, even if the pre- and post-drift have a slightly different slopes, an accurate measurement of the dose can be achieved.[3]

For isothermal operation, the signal of interest is the electrical power dissipated in the core over time. The goal is to measure the reduction in electrical power during irradiation that is required to maintain a constant temperature in the core, hence the name isothermal. There are many ways to determine the total electrical power, one of which is to use a linear fit through the data points. Using the signal prior to and following irradiation (in figure 2.4, points preceding 'A' and points proceeding 'D', respectively), the power dissipation baseline $P_0(t)$ is determined using a linear fit. Then, the points during the irradiation where stability was reached (in figure 2.4, points from 'B' to 'C') are used to determine the power deficit ($P_0(t) - P_i(t)$), which is proportional to the average absorbed dose rate. Using an iterative method, the points are moved by a small power increment $dP$ and a linear fit is done through all the points (except the transient portion, 'A' to 'B' and 'C' to 'D'). The power deficit is recorded when the coefficient of determination $R^2$ is at its minimum. Using the time from which the beam was on (in figure 2.4, points from 'A' to 'C'), the received absorbed dose can be calculated by multiplying the average dose rate to the duration of the beam.

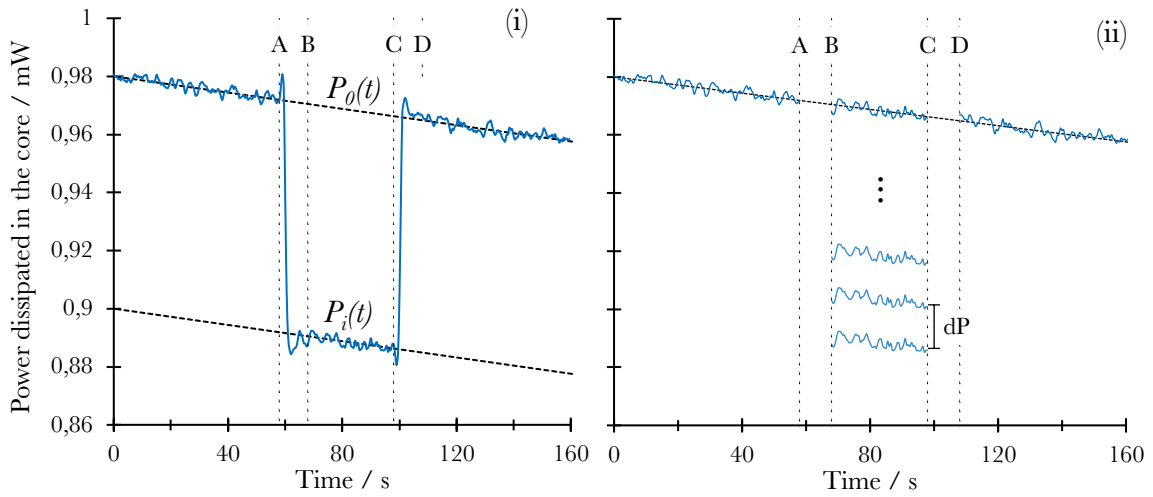


Figure 2.4: Isothermal dose calculation method. Point 'A' corresponds to the beginning of irradiation, point 'B' to the moment when stability is reach while the beam is on, point 'C' is when the beam is stopped, and point 'D' is when stability is reached following beam off. (i) The power dissipated in the core is used to determine the power deficit ($P_0(t) - P_i(t)$). (ii) Illustration of the iterative method in which the points between 'B' and 'C' are shifted by a small power increment $dP$ to calculate the power deficit.

## 2.4. Dose conversion in graphite with Monte Carlo

The goal of calorimetry in radiotherapy is normally to determine the absolute absorbed dose in water. Since the sensitive volume of a water calorimeter consists of water, no additional conversion is needed, however a graphite-to-water dose conversion factor is required for graphite calorimeters. The complexity of the calorimeter composition and geometry means that it is not possible to determine an accurate conversion analytically, rather, numerical modeling is used in this work to calculate the necessary factors.

Modeling and calculation are done by using Monte Carlo radiation transport techniques. Many different MC codes have been developed by the community to perform this task, but for the purpose of this thesis, EGSnrc[2] will be the only code discussed. EGSnrc has been

developed by the National Research Council Canada (NRC) and is a MC-based electron-photon transport toolkit. By modeling the specifics of the calorimeter in EGSnrc, dose convection factors for different setup conditions and beam characteristics (e.g. beam quality) can be determined. Using the egs_chamber user-code of Wulff et al.[5] with the egs++ geometry package.[6], a model of the calorimeter can be made, and the absorbed dose scored in the resulting geometry.

In order to calculate the dose conversion factors needed to go directly from the calorimeter dose to dose to water, two simulations are required: (i) calculating the dose to a small volume of water within a larger water phantom in the absence of the detector, and (ii) calculating the dose to the sensitive volume (core) of the calorimeter submerged at the same point as the small volume of water in (i). For (i), a thin disk of water in a water phantom is used in this work. In general, the smaller the disk, the closer it will be to approximating dose at a point, but also the more computationally-expensive it will be to achieve a given type A statistically accuracy.

For (ii), the dose to the sensitive volume of the calorimeter is calculated using the same setup conditions and beam characteristic as used in (i). Once the detector geometry is modeled, the Monte Carlo calculation is performed in order to score the dose received by volume of interest. Having both doses from (i) and (ii), the dose conversion factor is calculated as the ratio of doses scored in (i) to that of (ii).

## 2.5. Correction factors

In addition to the dose conversion, corrections factors are required to acquire an accurate dose measurement; two correction were used in the scope of this project and are presented in this section.

The first correction that needs to be applied is the impurity correction, $k_{\text{imp}}$. It corrects for the presence of materials different than the absorbing medium in the core (i.e., graphite) of the detector. These include the thermistors, wires, thermal insulation, etc. Depending on the composition of those materials, it can increase or decrease the dose. This correction can be calculated using Monte Carlo techniques or can be approximated using a summation of the mass energy absorption coefficient ratio weighted by the mass contribution of the core as shown in the equation below.

$$k_{\text{imp}} = \frac{m_{\text{core}}}{m_{gr} + \sum_i m_i \cdot \left(\frac{D_i}{D_{gr}}\right)} \approx \frac{m_{gr} + \sum_i m_i}{m_{gr} + \sum_i m_i \cdot \left(\frac{\mu_{en}}{\rho}\right)_{gr}^{i}} \qquad (2.8)$$

The second correction that needs to be applied is the heat transfer correction. For the quasi adiabatic and the isothermal modes, the correction is different due to the nature of the measurements. In the adiabatic case, there are inevitable heat losses to other parts of the calorimeter and to the surrounding environment. Even though those losses may be small, they can generally be determined using a finite element-based evaluation of the calorimeter, the experimental conditions, and heat sources and sinks. In the case of graphite calorimetry, the correction can also be assessed by approximating the amount of heat that is transferred from the core to the second layer (i.e, the jacket) of the calorimeter as shown in the equation

below. This model assumes that the temperature differences within each graphite component are small compared to the temperature differences between components.

$$\Delta E_{\text{tot,thermal}} = E_{\text{rad}} + \Delta E_{\text{transfer}} = m_{\text{core}} \cdot c_p \cdot \Delta T_{\text{core}} \qquad (2.9)$$

$$E_{\text{rad}} = \Delta E_{\text{tot,thermal}} \cdot k_{ht} = \Delta E_{\text{tot,thermal}} + \Delta E_{\text{transfer}} \qquad (2.10)$$

$$k_{ht} = 1 + \frac{\Delta E_{\text{transfer}}}{m_{\text{core}} \cdot c_p \cdot \Delta T_{\text{core}}} \approx 1 + \frac{h_{c,j} \cdot \int_0^t \left(T_{\text{jacket}} - T_{\text{core}}\right) \cdot dt}{m_{\text{core}} \cdot c_p \cdot \Delta T_{\text{core}}} \qquad (2.11)$$

In the isothermal case, the heat transfer correction has two terms. The first one account for the change in internal energy of the sensitive volume over the course of the acquisition. It is calculate using the deviation of the core temperature from the setpoint temperature. The second term accounts for changes in heat transfer over the course of the acquisition.

$$\Delta E_{\text{tot,thermal}} = E_{\text{rad}} + \Delta E_{\text{elec}} + \Delta E_{\text{transfer}} = m_{\text{core}} \cdot c_p \cdot \Delta T_{\text{core}} \qquad (2.12)$$

$$E_{\text{rad}} = \Delta E_{\text{elec}} \cdot k_{ht} = \Delta E_{\text{tot,thermal}} + \Delta E_{\text{elec}} + \Delta E_{\text{transfer}} \qquad (2.13)$$

$$k_{ht} = 1 + \frac{m_{\text{core}} \cdot c_p \cdot \Delta T_{\text{core}}}{\Delta E_{\text{elec}}} + \frac{\Delta E_{\text{transfer}}}{\Delta E_{\text{elec}}} \approx 1 + \frac{m_{\text{core}} \cdot c_p \cdot \Delta T_{\text{core}}}{\Delta E_{\text{elec}}} + \frac{h_{c,j} \cdot \int_0^t \left(T_{\text{jacket}} - T_{\text{core}}\right) \cdot dt}{\Delta E_{\text{elec}}} \qquad (2.14)$$

## 2.6. Uncertainties

Estimating the uncertainty of a measurement is as important as the measurement itself. The uncertainty on a measurement states how much confidence there is on the value of that measurement. In order to correctly state an overall measurement uncertainty, a good understanding of the measurement process is needed, and then a numerical analysis of each of the individual sources of uncertainty. There are two different types of uncertainties: type A and type B. The type A are uncertainties that can be evaluated using statistical tools, the most common of which being the standard deviation and the standard error. In contrast to

type A, type B uncertainties, must be evaluated using methods other than statistical methods.

The main type A uncertainty encountered in calorimetry is the reproducibility and repeatability of the measurement. Due to different sources of noise and variability, each time a measurement is taken, the detector response isn't exactly the same, even though the quantity to be measured hasn't necessarily changed. Quantifying the repeatability and reproducibility of a measuring device is done by taking many repeated measurements and looking at the spread of those measurements, and then having the entire experiment entirely redone by a different user. By increasing the number of repeated measurements, the mean value of the set will approach the "true value".

In calorimetry, there are many different sources of type B uncertainty and in general, a great deal of effort is made by primary dose standards labs to evaluate and minimize them. The following are some examples of type B uncertainty encountered in calorimetry: (i) The uncertainty associated with the proportionality constant used in the determination of the dose (i.e., specific heat capacity, core mass), (ii) the uncertainty associated with each of the correction factors , (iii) error in the temperature calibration of the thermistor can introduce uncertainty in the measurement, and (iv) the uncertainty associated with the MC radiation transport that affects the calculated dose conversion factor used in graphite calorimetry.

## 2.7. Conclusion

All the concepts presented in this chapter are key elements to understanding the rest of this thesis and will be further expanded upon within the specific context of this research project.

## 2.8. References


1. Incropera, F. P., Lavine, A. S., Bergman, T. L., & DeWitt, D. P. (2007). Fundamentals of heat and mass transfer. Wiley.

2. Kawrakow, I. (2000). Accurate condensed history Monte Carlo simulation of electron transport. I. EGSnrc, the new EGS4 version. Medical physics, 27(3), 485-498.

3. Seuntjens, J., & Duane, S. (2009). Photon absorbed dose standards. Metrologia, 46(2), S39.

4. Wikipedia.org/Wheatstone bridge. Material is available under Public License 3.0 Unported.

5. Wulff J, Zink K, Kawrakow I. Efficiency improvements for ion chamber calculations in high energy photon beams. Med Phys. 2008;35:1328– 1336.

6. Kawrakow I. egspp: The EGSnrc C++ class library. NRC Technical Report No. PIRS-899 (National Research Council of Canada, Ottawa, Canada, 2005).

7. Smalc, Martin, et al. "Thermal performance of natural graphite heat spreaders." ASME 2005 Pacific Rim Technical Conference and Exhibition on Integration and Packaging of MEMS, NEMS, and Electronic Systems collocated with the ASME 2005 Heat Transfer Summer Conference. American Society of Mechanical Engineers, 2005.

# Chapter 3 – Graphite probe calorimeter

## 3.1. Introduction

Since 2011, a Medical Physics Unit research group at McGill University has been developing an absorbed dose graphite calorimeter. The project aim is to develop a calorimeter suitable for use in the clinical environment. The probe-format was chosen to resemble an ionizing chamber to minimize the disruption to the clinical workflow. Over several prototype iterations, the graphite probe calorimeter (GPC; also referred to as Aerrow) has been used to perform accurate absorbed dose to water measurements in high energy photon beams, in both quasi-adiabatic mode and isothermal mode.[1]

The following chapter presents the design and operating principles of Aerrow for both the original and the newly-developed miniaturized version.

## 3.2. Aerrow design

Aerrow is made up of three nested cylinders of graphite each separated by a layer of aerogel-based thermal insulation. Temperature sensing is done with thermistors embedded in each of the graphite layers, and resistive heating is achieved with either thermistors or via wires connected to the graphite elements. During normal operation, thermistors are used to either sense or heat, but not both simultaneously. The cylindrical graphite pieces are made from high purity graphite (Isotropic Grade G458, Tokai Carbon Co., $\rho$ = 1.86 g cm$^{-3}$, thermal conductivity = 139 Wm$^{-1}$K$^{-1}$). A cross-section of the probe depicting the geometry is shown in Figure 3.1.A.

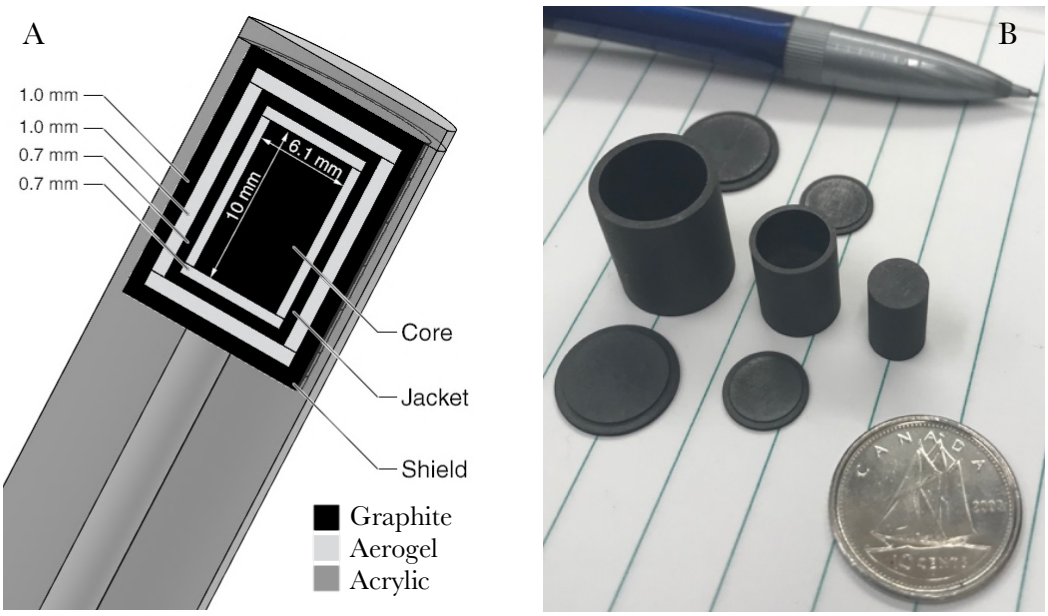


Figure 3.1: (A)Cross-section view of the fifth iteration prototype (MK-V) of the GPC probe with dimension of the pieces. (B)Photo of the graphite pieces used in the MK-V probe. The core goes inside the jacket and then inside the shield. The jacket and the shield are made of three pieces: a hollowed cylinder and 2 caps.

The layers in between the graphite pieces are made of a silica aerogel: the Airloy X103 made by Aerogel Technologies, LLC with a density of 0.2 g $cm^{-3}$. This formulation is used because of its relatively low thermal conductivity, 29 mW $m^{-1}$ $K^{-1}$, combined with its rigidness, which permits accurate machining similar to polystyrene. Also, because it is made mostly of air, it provides some electrical insulation between the graphite layers.

Every graphite layer has an NTC thermistors (A96N4-GC11KA143L/37C, Amphenol Advanced Sensors) with a nominal resistance of 22 kΩ at 25 °C, 44 AWG copper leads, and an encapsulated bead diameter and length of 0.32 mm and 2.29 mm, respectively. The core has two thermistors, one for heating and one for temperature sensing, and the jacket and shield has one each for sensing. The thermistors are placed inside the layer by drilling

a 0.3 mm diameter hole in the graphite, then secured with ethyl cyanoacrylate glue (LOCTITE 404, Henkel, Düsseldorf, Germany). Even though the thermistors act as point heat sources, the temperature is assumed to be uniform throughout the piece due to the relatively high thermal conductivity of graphite.

For the jacket and shield, two options were investigated for the heating. The first one is to simply use thermistors for the heating. To get to the required heat dissipation, more than one thermistor is used in both the jacket and the shield. The other method is to use the graphite element as the resistive element. By connecting the graphite pieces with simple leads, the graphite can be used to dissipate the heat within itself. That method has the advantage of reducing the quantity of non-graphite material inside the probe. The fifth generation prototype (referred as the MK-V) uses thermistor in every layer for heating, and the sixth generation (MK-VI) uses graphite connections for the jacket and the shield heating.

### 3.3. Control and Acquisition software

The control and acquisition software used for Aerrow is LabVIEW v.11.0, National Instruments. LabVIEW is a visual programming software that can be used to control and read-out various electronic instruments. In LabVIEW, there are two coding interfaces, the user interface (GUI), and the wiring diagram interface. In previous work, a complete LabVIEW code and user interface was built to operate Aerrow isothermally[1].

In isothermal mode, the temperatures are kept constant by active control heating done by PID controller. Standing for proportional integral and derivative, PID controller is a

common control loop mechanism used in process that needs constant control modulation. By computing the error between of the desired value and the current value, and calculating the integral and derivative of this error over time, the controller will respond in an effort to minimize the error depending on the user-defined weighting factors applied to each of the three error terms. The coefficient needs to be finely tuned for optimal response in terms of settling time, overshoot, steady-state error and stability.

The LabVIEW GUI contains three main functionalities: an active control of the probe and of the instruments, a data acquisition mode, and a beam emulation function for the PID testing. Within the active control functionality, the different control instruments can be powered on and off, the temperatures and the electrical powers dissipated can be readout in real-time for each component of the probe, the PID setting and the temperature sensing parameters can be adjusted on-the-fly. For the data acquisition mode, the user can initiate the saving of all information relevant to a run (bridge voltages, electrical power dissipations, etc.) into a single ASCII file. While the acquisition is running, the user can still use all the active control functions. The third mode is the beam emulation function for the isothermal mode in which an amount of electrical power equivalent to a user-specified dose rate is dissipated in the detector for a pre-determine duration. This mode permits the user to benchmark the PID response without the need to irradiate the device, and since the PID controllers can be very sensitive to the input parameters, this mode can be used to optimize the response prior to the experiment.

3.4. Acquisition hardware

The acquisition hardware consists of three main components. The first one is three identical 2182A Keithley nanovoltmeter used for the temperature sensing. Each nanovoltmeter is connected to a corresponding Wheatstone bridge circuit. That circuit box containing the Wheatstone bridges is the second component. The third component is National Instrument PXIe-1078 instrument chassis containing three National Instrument PXIe-4138 programmable power supply cards and one PXIe-4110 constant voltage supply card. The three programmable power supplies are used for the heating and are independently driven by the software-based PIDs. The constant voltage supply is used to provide a stable bias across the Wheatstone bridge circuits.

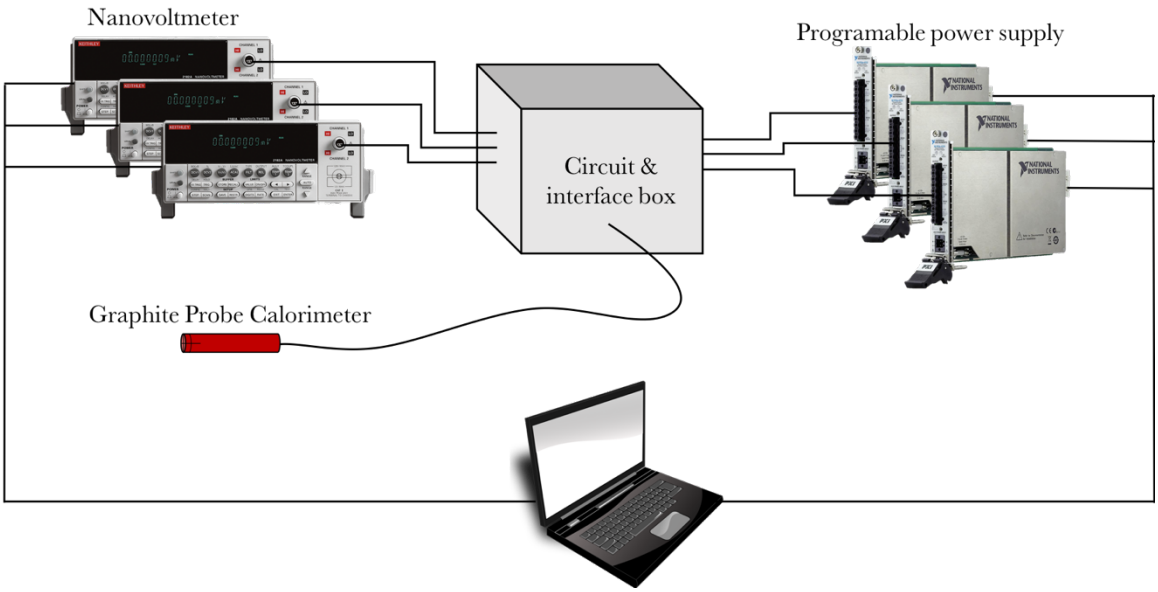


Figure 3.3: Diagram of the hardware components used for control and acquisition. The circuit and interface box contain the three Wheatstone bridges uses for temperature sensing and interface connector for the three components.

### 3.5. Aerrow mini design

Due to the size of the sensitive volume, the original Aerrow design is prone to volume averaging when used in fields smaller than 2 x 2 $cm^2$. The aim of this work is to adapt the original Aerrow design for use in small and composite radiation fields.

The proposed solution was to scale down the original design by a factor of two, resulting in a sensitive volume (i.e. core volume) reduced by a factor of eight. The first step prior to building a prototype was to investigate whether the choice of rigid aerogel formulation could be optimized for use in smaller fields. The following section presents the investigation of the effect of the density of the aerogel on the response of Aerrow in small fields. Aerrow-mini, as it is referred to in this work, has only one thermistor in each of the graphite pieces for temperature sensing, one additional thermistor in the core for heating, and direct in-graphite heating both the jacket and the shield. This configuration represents the minimum amount of non-graphite material required to build a functioning prototype capable of isothermal operation.

#### 3.5.1. Aerogel study

It is known that the composition and the density of the materials that surround the sensitive volume of a detector will have an increased effect on the response at small fields [3,4], but in order to draw a clear picture in the case of Aerrow-mini, simulations were needed. Using Monte Carlo methods, the perturbative effect of composition and density of the aerogel was performed.

Using EGSnrc, Aerrow-mini was modeled. The modeling was done using the egs_chamber usercode[5] with the egs++ geometry package V2017[6]. The model geometry was verified using the egs_view program. The source model used for the simulation was a BEAMnrc model of a Varian Novalis linear accelerator 6 MV beam, which has been previously validated for field sizes down to 0.5 × 0.5 $cm^2$. [3] In the model, the detector was positioned at a depth of 10 cm in a 30 × 30 × 30 $cm^3$ water phantom and aligned vertically on the beam central axis. The vertical orientation was chosen to get the smallest projection of the sensitive volume; in other words, the long axis of the detector was placed parallel to the beam axis. The phantom was placed at an SSD of 100 cm and irradiated with a 6 MV beam. To calculate dose conversion factors, as described in section 2.4, the dimension of the water disk for the dose to water scoring was chosen to an error below 0.1 % on the measured dose value for each field size. Further explanation will be provided in section 4.6.1. The transport parameters were set to: ECUT & AE = 512 keV, PCUT & AP = 1 keV, SMAX = $10^{10}$, ESTEPE = 0.25, XIMAX = 0.5, EM ESTEPE = 0.02 & 0.01 for Aerrow and phantom, EXACT boundary cross algorithm, and PRESTA II electron-step algorithm. The variance reduction technique parameters were: photon cross section enhancement factor = 16, russian roulette survival factor = 256, and ESAVE = 512 keV.

The dose scored in the small disk of water was used along with the dose scored in the graphite core to calculate $k^{f_{clin},f_{msr}}_{Q_{clin},Q_{msr}}$, according to the definition in equation 1.15 presented in chapter 1. The figure below shows the results for two commercially available rigid aerogels: Airloy® X103 (Aerogel Technologies LLC, Boston MA), and Aerozero® (Blueshift Materials Inc, Spencer MA). The names of the different curves represent the product name

and then the density in [g/cm$^3$]. In every case, the investigated aerogel was used for both insulating layers in the probe geometry (between core and jacket, and between jacket and shield).

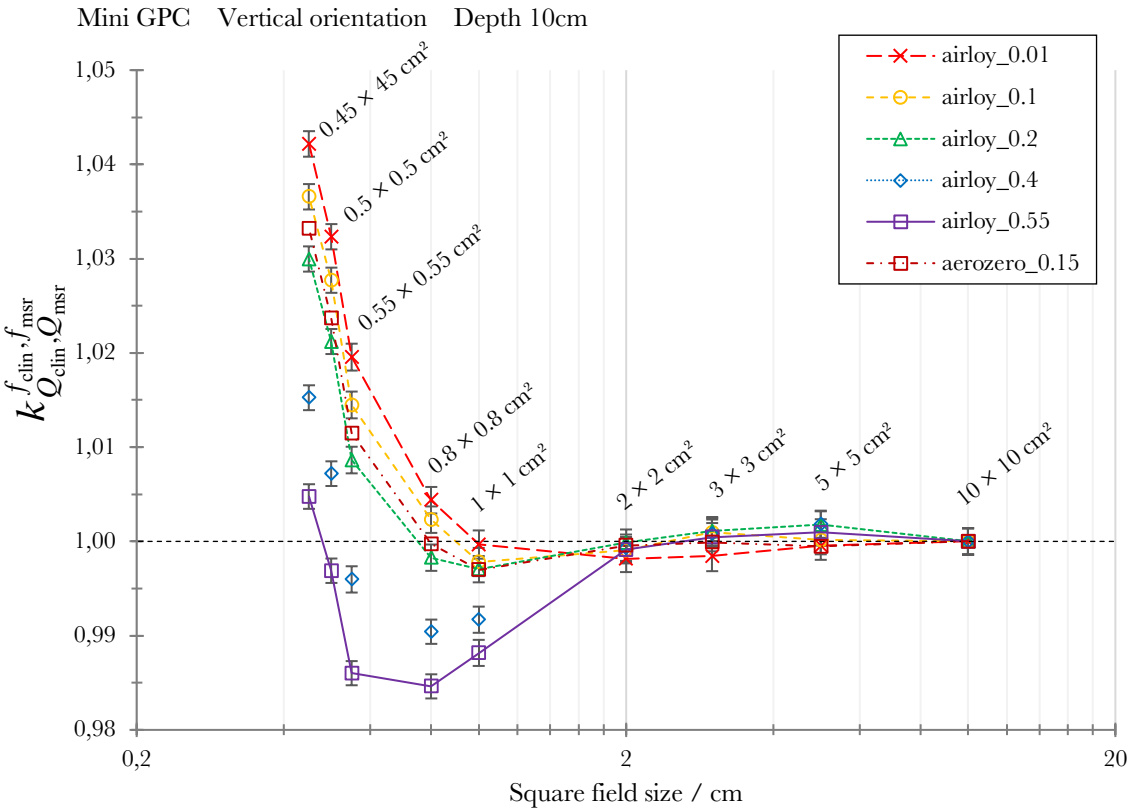


Figure 3.4: Small field detector correction factor as a function of the field size for various commercially available rigid aerogels.

The results in figure 3.4 show that for all investigated aerogels, the correction is practically unity for fields of 2 × 2 cm$^2$ and larger. Below 2 × 2 cm$^2$, the two densest aerogels exhibit a relatively large drop in the correction factor, each reaching a minimum around 0.8 x 0.8 cm$^2$, before increasing beyond unity at the smallest investigated field sizes. The aerogels with a density of less than 0.3 g/cm3 exhibit only a relatively small drop, if any, before a relatively rapid increase as the field size is decreased. It can be inferred from the graph that

the shape of the correction factor curve is less dependent on aerogel composition than on the density. The airloy and the aerozero formulations have a different composition: airloy is made of silica and has a $Z_{eff}$ of around 11.6, while aerozero is made out of an organic polyimide with a $Z_{eff}$ around 6.6, nevertheless, the Aerozero curve (density 0.15 g/cm$^3$) lands directly in between the two Airloy curves (densities of 0.1 and 0.2 g/cm$^3$). The general shape of these curves was also observed by groups studying the PTW 60019 microDiamond detector and was explained by the fact that the correction curve is in fact shaped by two competing effects: a volume averaging effect and a density effect[2]. The density effect is caused by having different density materials surrounding the sensitive volume, and perturbating the charged particle equilibrium. The density effect is dominant at larger field sizes and decreases the correction factor, but is overcome by the volume averaging effect, which results in an increasing correction as the field size is decreased.

Guided by these results, an aerogel selection was made for the construction of the first Aerrow-mini prototype. The purpose of this study was to select an aerogel with a correction factor with the smallest deviation from unity throughout the investigated range of field sizes; by this criterion, the Airloy with a density of 0.4 g/cm$^3$ was selected.

### 3.5.2. Effect of miniaturization

Even though the physical proportions have not changed with the Aerrow-mini, a change in the response is expected because of the reduction of the mass of the core. The relative change in response can be predicted using the proportionality expressions dictating response for both the adiabatic and isothermal mode:

$$\text{Adiabatic: Signal} \propto D/C_p \qquad \text{Isothermal: Signal} \propto D \cdot M_i$$

For the adiabatic mode, because the signal is only proportional to the dose and inversely proportional to the specific heat capacity, no change in response is expected by miniaturizing of the probe. However, for the isothermal mode, the signal is proportional to the dose as well as the mass of the core, therefore by reducing the mass by a factor of eight, the signal is expected to also be reduced by a factor of eight. The result of this decreased signal will affect the signal to noise (SNR) ratio of the acquired data. For reference, the original Aerrow design exhibits a typical SNR of about 85 for a 4 Gy/min irradiation.

Also, by reducing the mass of the overall probe, it can be expected that the thermal inertia of the probe will be reduced by a factor of eight, reducing the response time for the PID controller. On the other hand, it makes the probe more sensitive to perturbations caused by thermal non-uniformities.

## 3.6. Construction

### 3.6.1. Machining

The first step in the construction of the Aerrow-mini was to machine the different aerogel parts. Most of the machining was done in-house on a manual metal lathe. The aerogel cups were made by machining a small cylinder to the desired outer dimension, then a small aluminum ring was placed over top to add some support to the piece. A hole was then bored into the piece with a flat-ended milling bit to the desired depth. The machined piece was then detached from the aerogel blank using a parting tool. Finally, some excess material was removed by hand using sandpaper. The graphite pieces were custom made by the supplier, therefore no additional machining was needed.

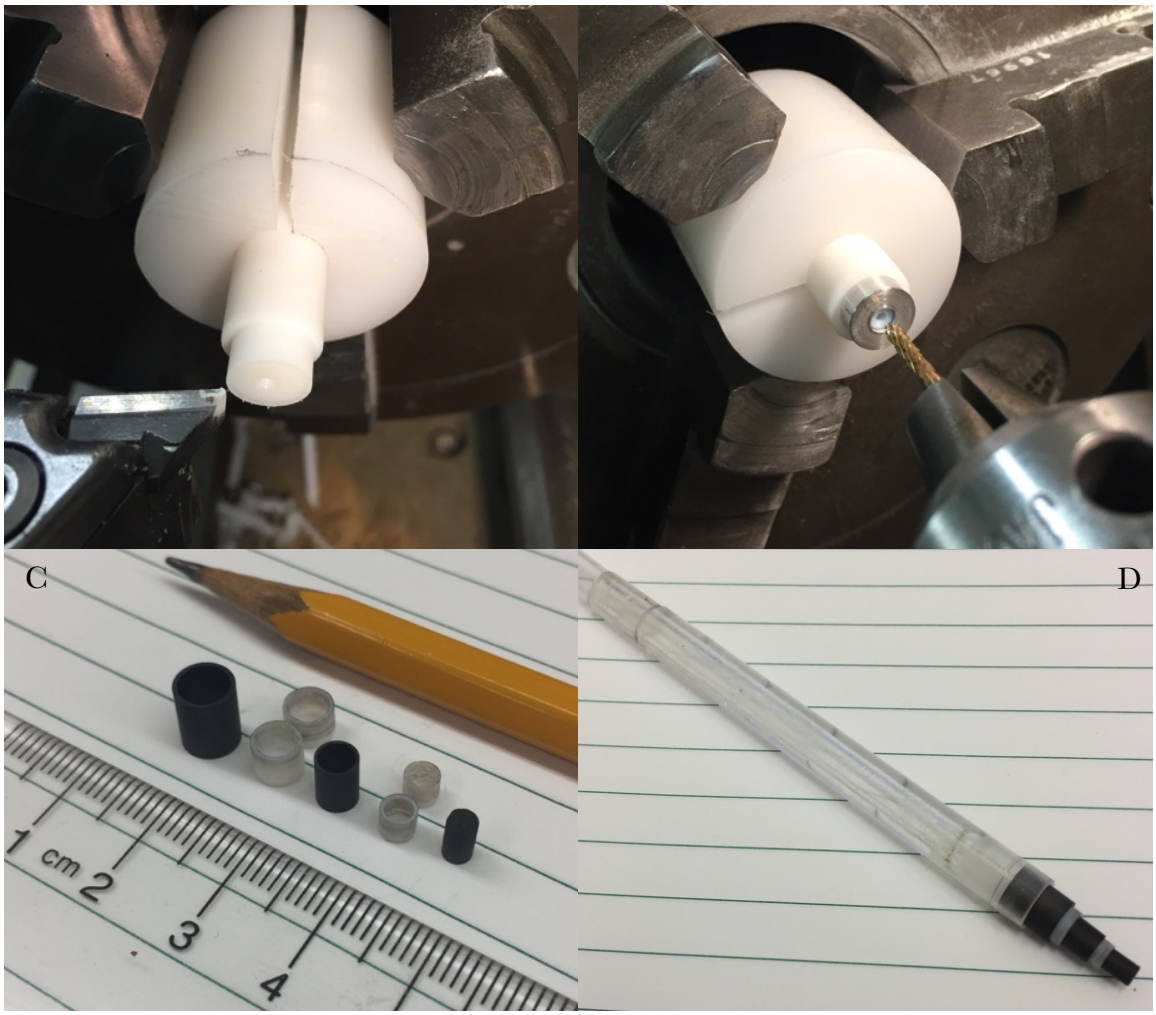


Figure 3.5: Various photos of the machining of the aerogel pieces. A) Machining of the piece to the correct outer dimension. B) Drilling of the piece to the correct inner dimension using a flat-ended milling bit and an aluminium ring for additional support. C) The four aerogel parts (white) next to the graphite pieces (black). D) Example of how the pieces are assembled and inserted in the homemade acrylic stem

Once all the pieces were made to size, four holes of 0.3 mm diameter were drilled to accept the thermistors, two holes of 0.2 mm diameter were drilled in each of the jacket and the shield to accept the stripped heating wire, and finally, holes of 0.3 mm diameter were drilled in both the aerogel and graphite to permit the internal passage of the heating wires. Once all the holes were drilled, the probe was ready for assembly.

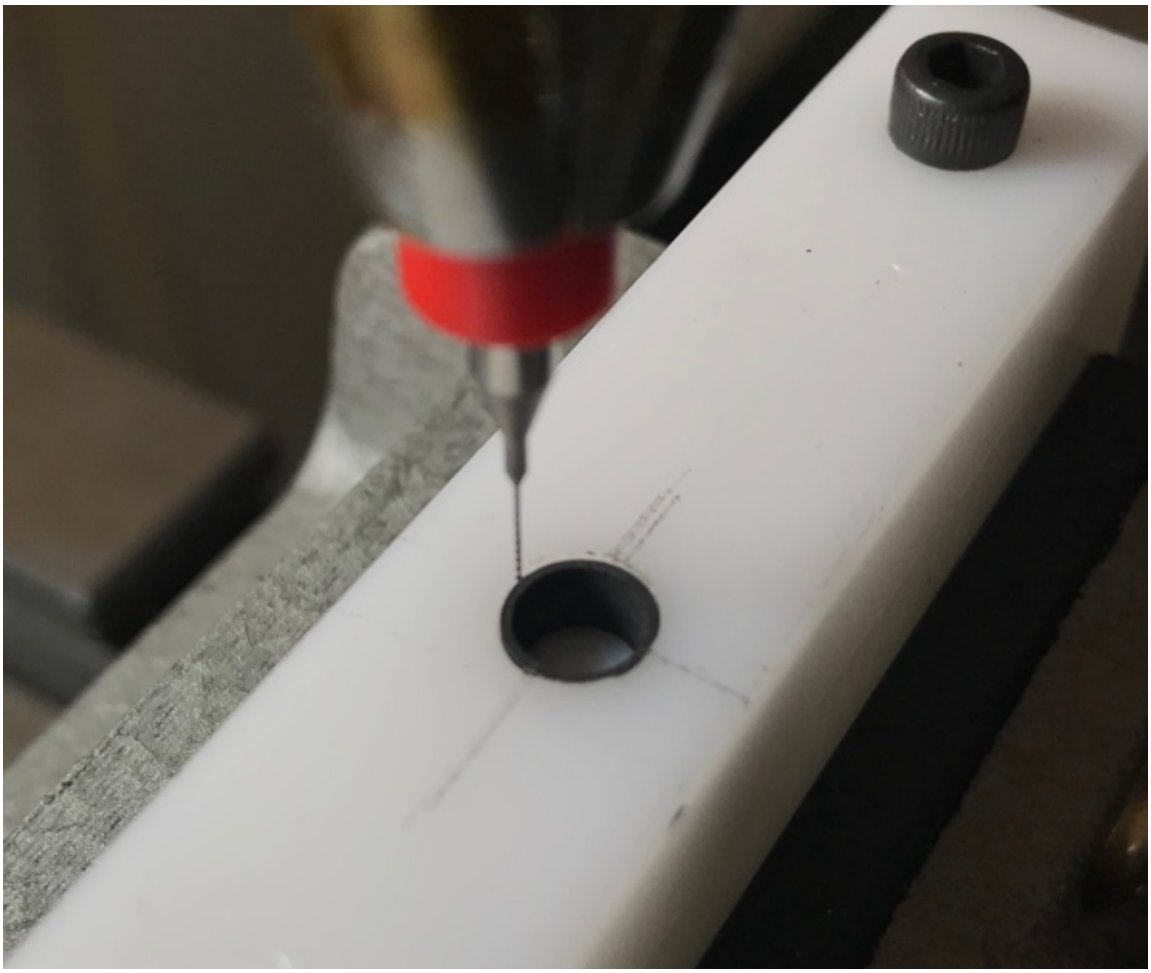

Figure 3.6: Drilling of the thermistor's hole in the shield using a 0.3 mm drill bit.

### 3.6.2. Mass measurements

Prior to the assembly, the mass of each component was measured using a high accuracy scale (Denver instrument, APX-200, nominal sensitivity = 0.1 mg). Having accurate knowledge of the masses, especially of the core and innermost aerogel layer, is essential for accurate dosimetry in the isothermal mode.

| Component | Mass ± 0.1 µg | Component | Mass ± 0.1 µg |
|---|---|---|---|
| Core (drilled) | 66.6 | Aerogel shield 2 | 20.9 |
| Aerogel jacket 1 (drilled) | 8.3 | Shield (drilled) | 137.3 |
| Aerogel jacket 2 | 8.7 | Shield cap 1 (drilled) | 25.8 |
| Jacket (drilled) | 48.6 | Shield cap 2 | 27.5 |
| Jacket cap 1 (drilled) | 9.0 | Average thermistors mass | 0.4 |
| Jacket cap 2 | 9.1 | Estimated amount of glue | 0.8 ± 0.3 |
| Aerogel shield 1 (drilled) | 21.0 | | |

Table 3.1: Mass measurements of every component of the probe measured by a high accuracy scale (Denver instrument, APX-200). The ± 0.1 µg uncertainty comes from the balance precision. The uncertainty from the mass of glue come from the fact that the amount was estimated and not directly measured.

### 3.6.3. Assembly

The assembly was performed under a stereo microscope due to the scale of the task and the required precision. The wires and thermistors were threaded through the perforated pieces of graphite and aerogel in the correct order. Thermistors were then placed in their corresponding hole and secured with cyanoacrylate. The layers were assembled one by one starting with the core and working outwards. Once assembled, the jacket and shield graphite caps were held in place using cyanoacrylate. Once the detector was assembled, the leads were pulled through the waterproof stem and tubing.

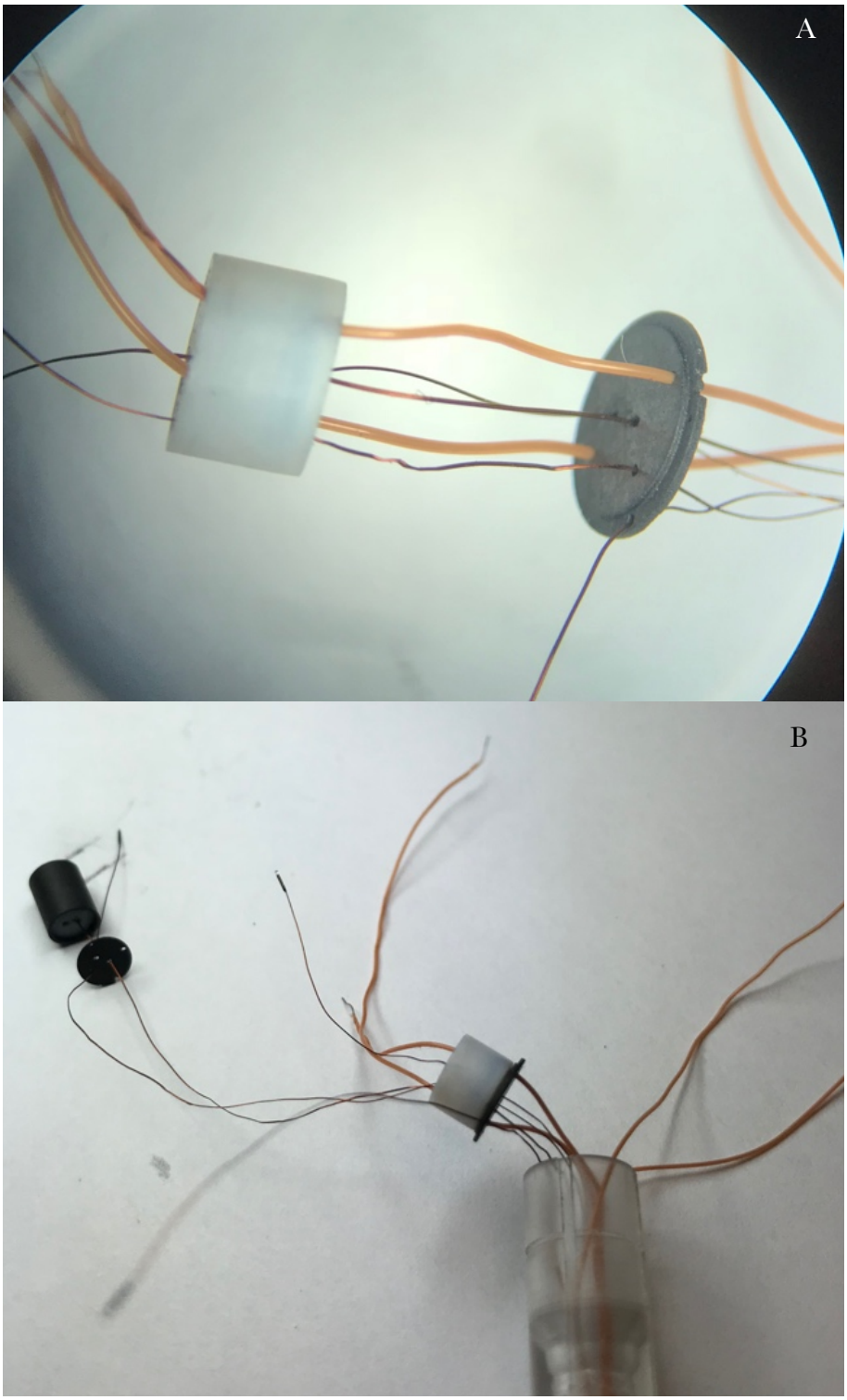


Figure 3.7: Photos of the assembly of the probe. A) Close-up of the wires passing through the shield cap. B) Photo during the assembly, before the second core's thermistor was placed.

3.7. References


1. Renaud, James, et al. "Aerrow: A probe-format graphite calorimeter for absolute dosimetry of high-energy photon beams in the clinical environment." *Medical physics* 45.1 (2018): 414-428.

2. De Coste, Vanessa, et al. "Is the PTW 60019 microDiamond a suitable candidate for small field reference dosimetry?." *Physics in Medicine & Biology* 62.17 (2017): 7036.

3. Papaconstadopoulos, P., F. Tessier, and J. Seuntjens. "On the correction, perturbation and modification of small field detectors in relative dosimetry." *Physics in Medicine & Biology* 59.19 (2014): 5937.

4. Palmans, Hugo, et al. "Dosimetry of small static fields used in external photon beam radiotherapy: Summary of TRS-483, the IAEA–AAPM international Code of Practice for reference and relative dose determination." *Medical physics* 45.11 (2018): e1123-e1145.

5. Wulff, J., K. Zink, and I. Kawrakow. "Efficiency improvements for ion chamber calculations in high energy photon beams." *Medical physics* 35.4 (2008): 1328-1336.

6. Kawrakow, I. "egspp: the EGSnrc C++ class library." *National Research Council of Canada Report* (2005).

# Chapter 4 – Measurement and simulation results

## 4.1. Isothermal acquisition

Once the probe assembly was completed, a calibration was performed to prepare the probe for measurement. Using the two-step temperature calibration (see section 2.3.2), the sensing thermistors were calibrated. The temperature setpoints were set by first using a 20 kΩ balancing resistance (referred as $R_2$ in section 2.3.1) in the core bridge resulting in a corresponding temperature setpoint of (27.213023 ± 0.000005) °C, then similarly setting the jacket and the shield temperature setpoints to approximately 0.1 °C and 0.2 °C lower than the core temperature setpoint, respectively (balancing resistance of 20.4 kΩ and 18.1 kΩ were used for the jacket and shield respectively). After a heuristic PID tuning for the three layers using the emulation mode (see section 3.3) of the LabVIEW GUI, the probe was deemed ready for experimental measurements in the isothermal mode. A combination of Ziegler–Nichols method and fine tuning was used to tune the PID to an optimized response; to achieve better stability at the price response time, the P and D terms were decreased.

The measurements were performed at McGill University Health Center (MUHC) using a clinical Varian TrueBeam linac with a calibrated output of 1 cGy/MU at the depth of dose maximum under standard reference conditions. A field size of 10 × 10 $cm^2$ at SSD 100 cm was set, a 20 × 20 × 23.7 $cm^3$ water equivalent phantom (Solid Water High Equivalency (SWHE) model #557, Sun Nuclear Corp.) was placed at an SSD 100 cm using a calibrated mechanical pointer. The probe was placed in a water-equivalent sleeve positioning the center of the probe at a depth of 10 cm in the phantom. The alignment of the phantom

with the beam's central axis was made with the room's lasers and the light field. The first set of measurements was made on November 7th, 2018. The figure below (4.1) shows a photo of the setup.

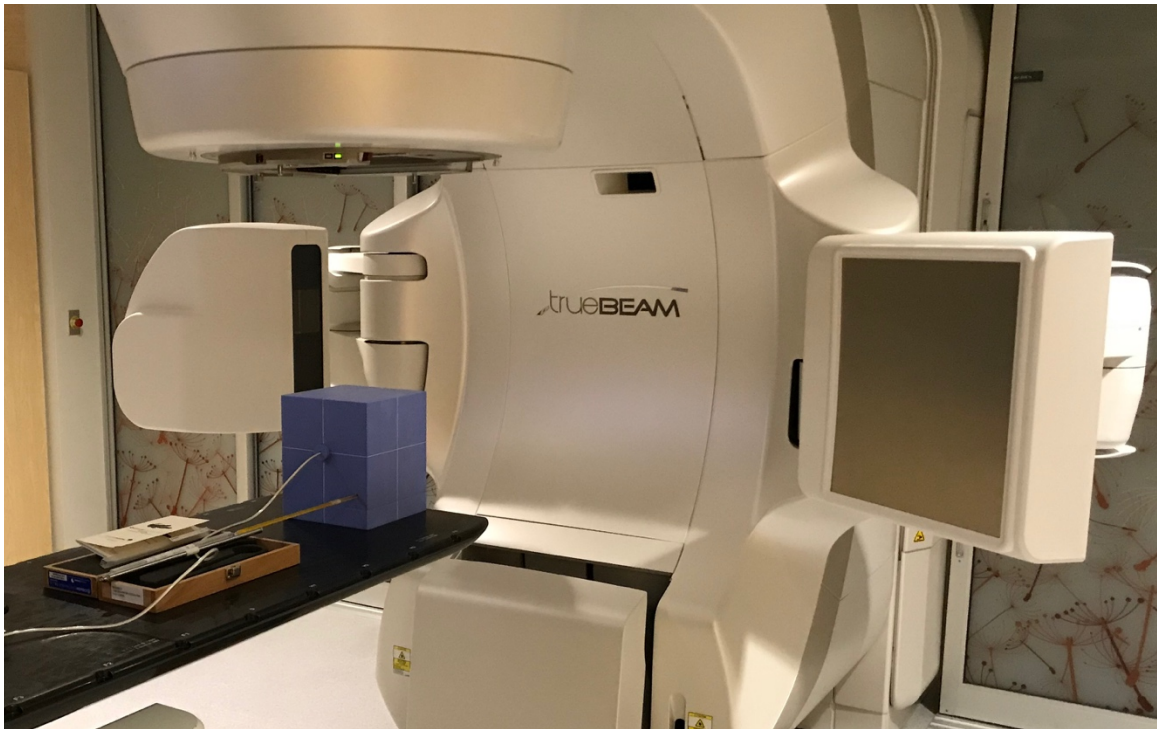


Figure 4.1: Photo of the setup for the first isothermal mode measurements performed on Nov 7th, 2018. The blue water equivalent phantom is placed at SSD 100 cm with its center aligned with the beam axis. The gantry is positioned at a 0° angle. In the center of the phantom, the detector is inserted in a dedicated sleeve to position the center of the core at a depth of 10 cm in phantom. A hole is drilled at the lower corner of the phantom to insert a thermometer.

From the initial set of acquisitions, it was observed that the measured signals did not correspond to the expected isothermal shape (pseudo-square wave). Figure 4.3 shows two of the acquisitions. A 6 MV beam at 600 MU/min was used with at least 600 MU delivered.

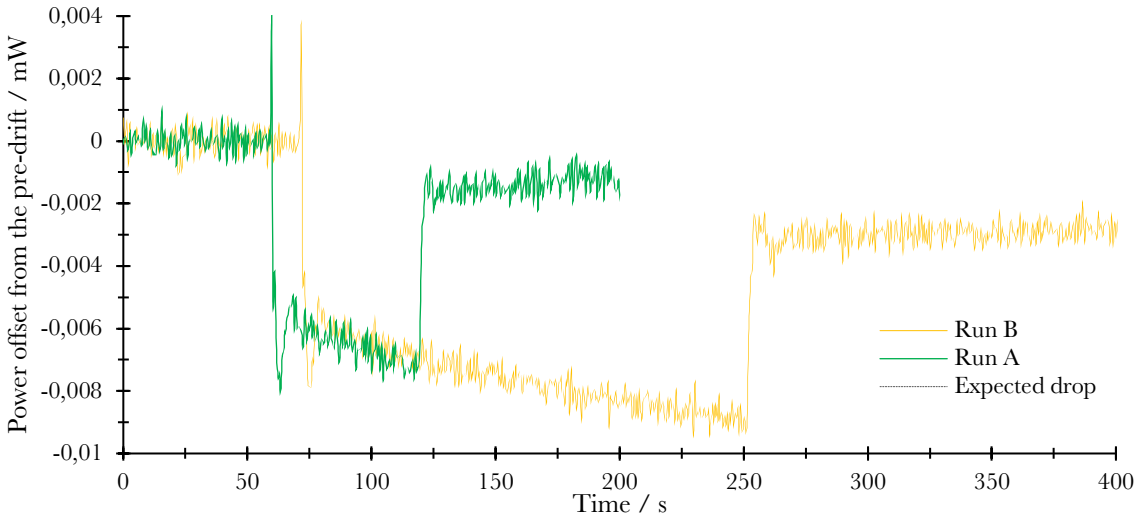


Figure 4.2: Signal of the power dissipated in the core over the time period of acquisition. The irradiation was a 6 MV beam at 600 MU/min. Runs A and B were 600 MU and 1800 MU irradiations, respectively. For both signals, the linear drift in the pre-irradiation portion was removed from the entire acquisition. The expected drop, shown as a dashed line, was calculated using the mass of the sensitive volume (i.e. the graphite core, the airloy jacket, the thermistors and the glue), the expected dose rate from the linac calibration, the Monte Carlo calculated dose conversion factor and the PDD at 10 cm for a 6 MV beam.

From figure 4.2, we can see that the signals from the isothermal runs are larger than expected. Every acquired run exhibited the same behavior: a negative slope during the beam-on time, which results in a post-drift power dissipation that is lower than the pre-drift amount. In figure 4.2, the two slopes during the beam-on period are similar in magnitude, but the offsets of the post-drift relative to the pre-drift appear to be dependent on the beam-on time. This behavior results in an inaccurate dose calculation since the analysis model assumes a constant slope in the power dissipation curve (save the transient portions which occur when the beam is turned on and off). Because of this variable slope, the dose calculated by the model is strongly affected by the amount signal that is neglected post-transient, and by the duration of the beam on time. The following figure shows an example of an analysis using the aforementioned model to determine the power drop in the acquisition.

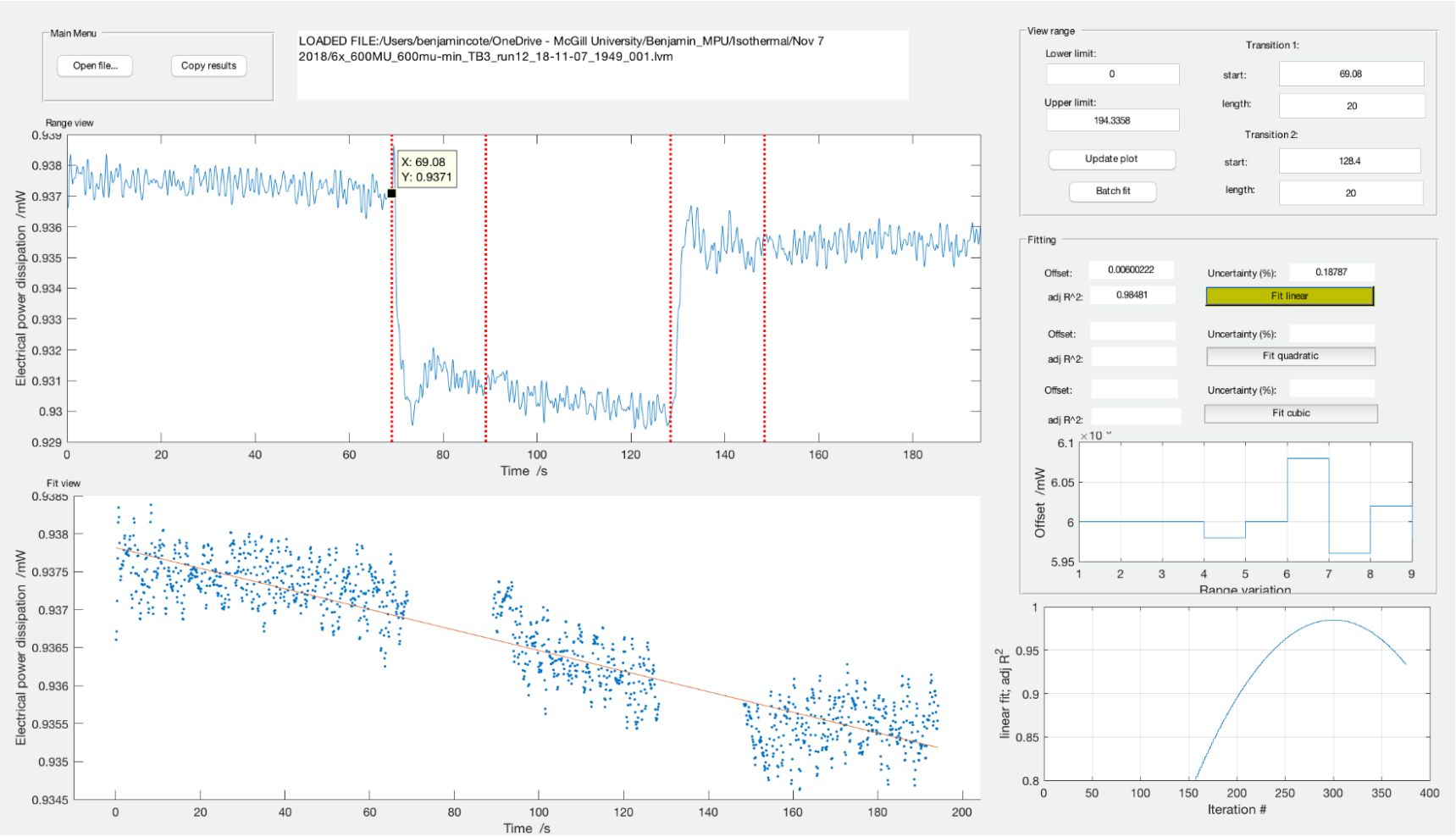


Figure 4.3: Screenshot of the MATLAB GUI used for the isothermal analysis[1]. A 60s run is being analyzed by indicating the beginning and end of the irradiation, and the extent of how much of the signal should be neglected post-transient (depicted visually by the portions of the signal contained within the two sets of vertical dashed lines in the top left plot).

From figure 4.3 the linear fit that is used by the model to calculate the power offset is inaccurate since each section (pre-drift, beam on, and post-drift) of the signal has a different slope. Even though the model is not appropriate to calculate an absolute power, it is interesting to look at the repeatability of the result given a set of measurements. Eleven identical runs performed using a 600 MU irradiation of a 6 MV beam at a repetition rate of 600 MU/min. For the analysis, a 20 s portions of the signal were neglected following beam on and off. Figure 4.4 depicts the repeatability of the measured drop in power dissipation in the core.

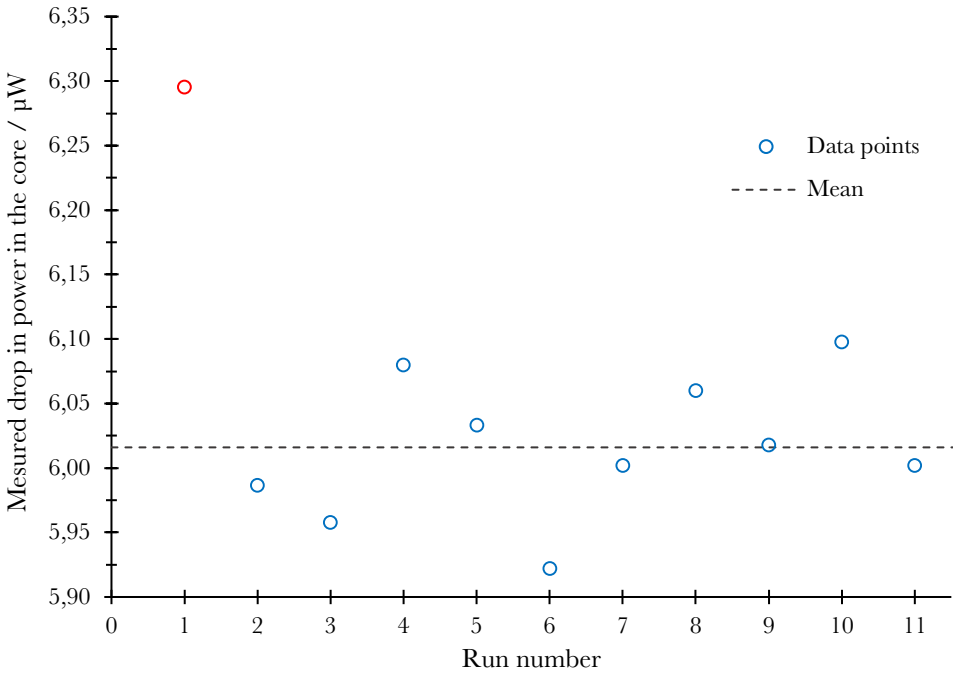


Figure 4.4: Calculated power drop in the core for eleven identical runs. The irradiation was a 600 MU 6 MV beam at 600 MU/min. The first (red) point was excluded from the mean; this outlier can be attributed to the relatively large drift in the power signal (4.6 µW/min vs. < 2.0 µW/min for all other runs).

When neglecting the first run, the measured drop in power has a relative standard deviation of 0.9%. As an exercise, the absorbed dose can be determined from the mean measured

power value of the set of 10 runs (see equation 2.3). Table 4.1 lists the parameters involved in the calculation of the absorbed dose to water at the depth of dose maximum.

| Quantity | Value | Unit |
|---|---|---|
| Mean measured power | 6.016 ± 0.004 | μW |
| Mass of the core | 86.1 ± 0.3 | μg |
| Dose rate | 6.987 ± 0.4 % | cGy/s |
| Beam-on time | 60.08 ± 0.07 | s |
| Dose to core at 10 cm | 69.87 ± 0.5 % | cGy/100MU |
| Dose conversion factor (see section 4.6.2) | 1.1268 ± 0.4 % | water/graphite |
| Dose to water at 10 cm | 78.72 ± 0.7 % | cGy/100MU |
| Dose to water at $z_{max}$ | 118.6 ± 0.8 % | cGy/100MU |
| A1SL chamber measurement | 102.9 ± 1.3 % | cGy/100MU |

Table 4.1: Dose calculation for the first set of measurement done on November 7th. The mass of the core corresponds to the measured mass of the graphite, the Airloy jackets, the thermistors, and the glue. The details of the dose conversion factor calculation are presented in section 4.6.2. The chamber measurement was made in the same solid phantom, was corrected with $k_{TP}$, $k_{ion}$, $k_{pol}$, and the $k_Q$ from TG-51 addendum[6] was used.

As seen in table 4.1, the measured dose to water is approximately 15 % greater than the one measured by a A1SL in the same condition. A discrepancy of this magnitude is almost certainly due to the varying slope problem, which is not well-handled by the analysis model. A complete discussion on the slope problem is presented in the following chapter. Additional measurements were performed on subsequent days to gain more insight into the unexpected response of the probe; irradiation time (60 s to 180 s), beam quality (6 MV and 10 MV flattening-filter free (FFF)) and dose rate (400 MU/min to 2400 MU/min) were varied, but no major differences in signal shape were observed.

During the subsequent measurement sessions, an erratic and irregular behavior in the measured powers and temperatures started to appear. Sudden instability in the probe temperatures and powers was observed without any apparent provocation.

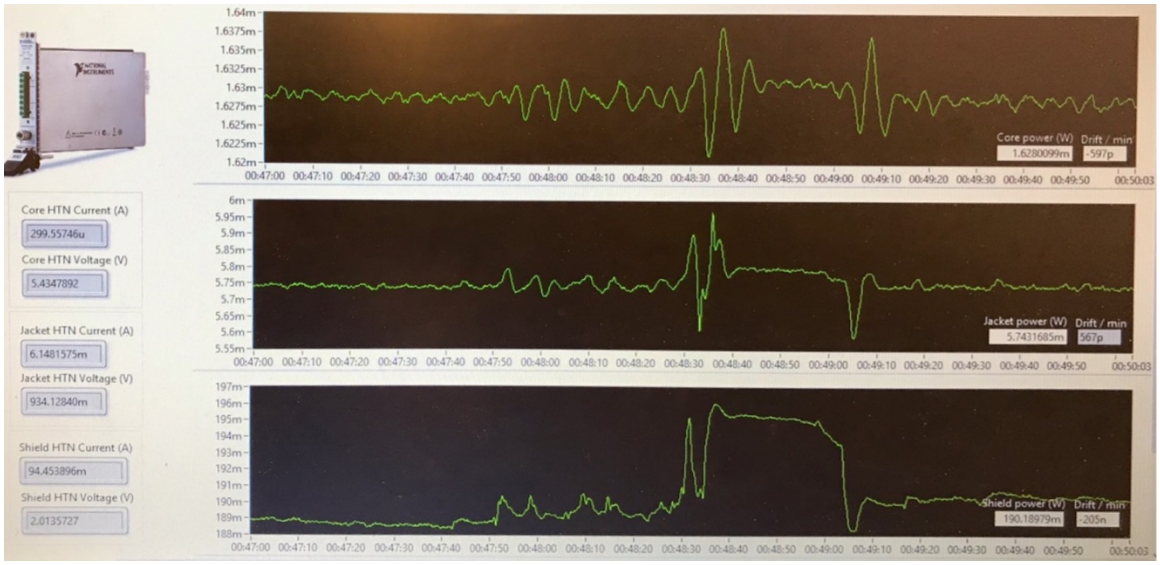


Figure 4.5: Snapshot of the power signal in the three layers. From top to bottom it represents the core, jacket, and shield respectively. The largest perturbation appears to occur in the shield, which then affects the jacket and core.

Figure 4.5 shows an example of the perturbation. This unexplained phenomenon can be described as sharp discontinuity in the shield temperature, which leads to a temporary loss in the equilibrium of the entire probe. The frequency of the perturbations gradually increased with time, to the point were performing isothermal measurements was nearly impossible. Further investigation was needed to characterize and/or eliminate the problem. Those investigations are presented in the following section.

4.2. Acquisition sampling rate

To get accurate and precise measurements with the probe in isothermal mode, the temperature and power stability is a key component. Each layer of the probe is thermally coupled, and instability can propagate from one layer to another. At first glance, the perturbation problem seemed to originate from instability in the shield, as shown in fig 4.5. One hypothesis to explain the cause of this erratic behavior was that the non-constant sampling rate ((8.7 ± 0.2) Hz, value ranging from 10.5 Hz to 5 Hz) controlled by the acquisition software was resulting in a potentially unstable PID controller output. An experiment was thus performed to investigate the possible effect of the sampling rate.

Typically, the LabVIEW code behind the control and acquisition software is set up to achieve a maximum sampling rate (nominally 10 Hz) the only limit being the communication rate between the instruments and the software. To investigate the possible effect of a variable sampling rate, code was added to permit the limiting of the refresh rate. By purposely slowing down the code, it was possible to observe the effect of the sampling rate on the stability of the probe as well as the behavior of the perturbation of unknown origin. For the experiment, the sampling rate was varied between 100 ms to 500 ms. The variation in the measured shield temperature was recorded and the stability of the probe was observed. At each investigated sampling rate, a perturbation was induced on the probe by gently blowing air on it to verify if the probe was able to come back to its stable state.

| Sampling rate | Frequency | Shield temperature variation amplitude | Comment on probe stability |
|---|---|---|---|
| ms | Hz | μK | |
| 100 | 10.0 | ± 20 | Stable, before and after the perturbation |
| 104 | 9.6 | ± 20 | |
| 106 | 9.4 | ± 20 | |
| 109 | 9.2 | ± 30 | |
| 112 | 8.9 | ± 30 | |
| 118 | 8.5 | ± 40 | |
| 125 | 8.0 | ± 40 | |
| 130 | 7.7 | ± 40 | |
| 139 | 7.2 | ± 40 | |
| 150 | 6.7 | ± 50 | |
| 165 | 6.1 | ± 50 | |
| 200 | 5.0 | ± 50 | |
| 250 | 4.0 | ± 60 | |
| 333 | 3.0 | ± 80 | |
| 500 | 2.0 | - | Unstable |

Table 4.2: Effect of the sampling rate on the variation of the shield temperature about its setpoint, and on the probe whole stability. The temperature variation amplitude describes the average peak to peak range of the variation.

The results in table 4.2 suggest that the perturbation is not due to a varying sampling rate, as instability occurred only at a relatively low sampling rate (between 2 - 3 Hz). By reducing the sampling frequency, the amplitude of the variation in the shield temperature steadily increased, but not to a level where it strongly affected the temperature stability in the jacket and core layers.

Given these results, the hypothesized sampling rate effect was excluded from the investigation into the erratic perturbation.

4.3. Electrical coupling

Another hypothesized cause for the perturbation, was electrical coupling in the three heating circuits. This idea was supported by the observation that perturbations occurring in the three graphite layers were often simultaneous (within the sample rate). If the perturbation were thermal in origin, an observable time delay would be expected, given the thermal transfer time constants between the layers of the probe.

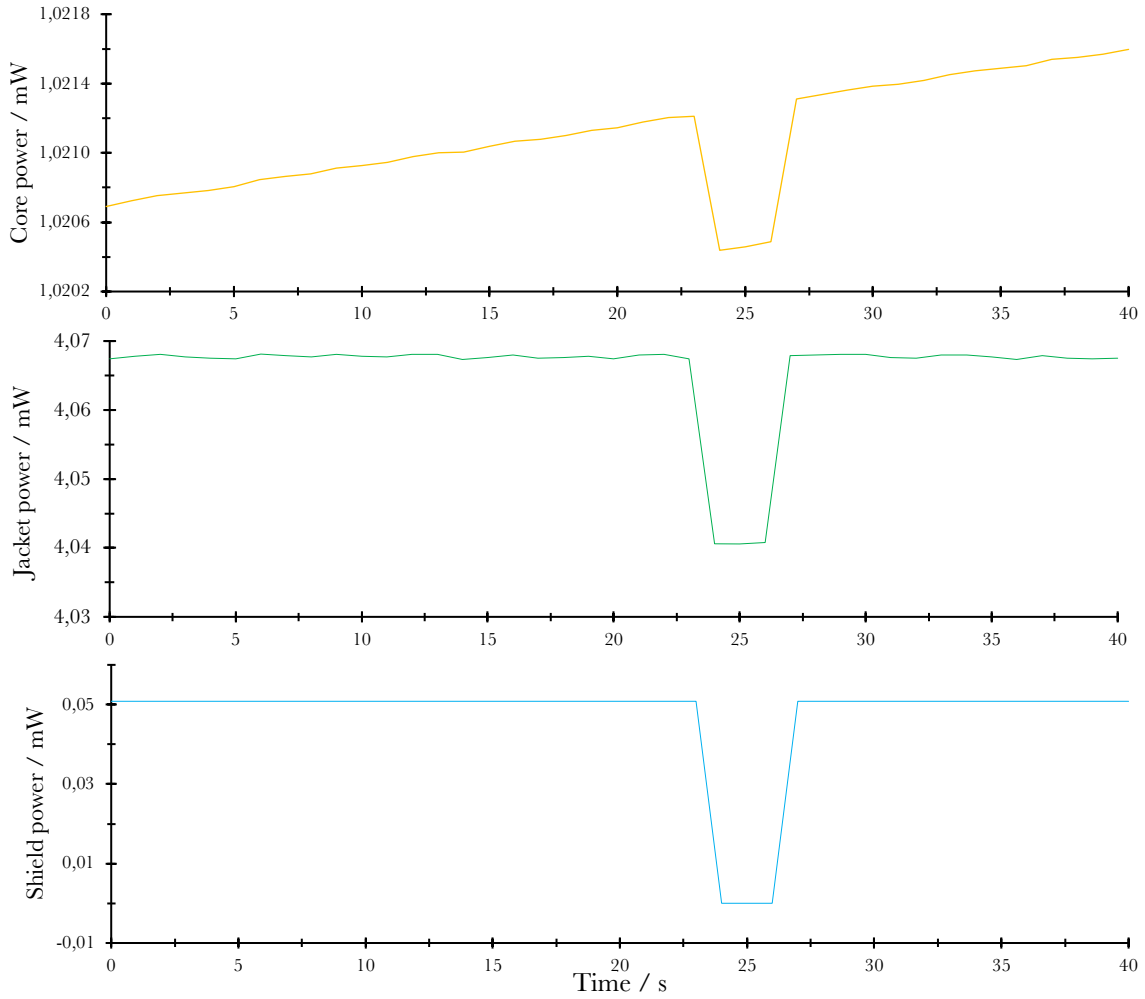


Figure 4.6: Simultaneous recording of the power curves showing the electrical coupling of the three graphite layers of the probe. At the 23 s mark, the current in the shield drops from 1 mA to 0 mA for approximately 3 seconds. The instant effect can be observed on the core and jacket, despite their respective constant current outputs having not changed.

Two different tests were designed to quantify the observed coupling. For each of the two tests, the probe and all the instrument were connected as they would be for normal isothermal operation. In the first test, the heating current in the core and jacket was forced to be 0 mA, and the current in the shield was varied between 0 mA to 160 mA (typically a current of around 90 mA is applied during stable operation). The heating power measured by the SMUs was recorded in each layer. The second test was the same as the first, except that the heating current in the core and jacket was set to a constant value to produce heating powers typical of normal isothermal operation (around 1 mW and 4 mW for the core and jacket, respectively). The current in the shield was again varied between 0 mA to 160 mA, with the same increments as the first test, and the resulting powers in the three layers were recorded.

| Shield heating current | Heating power measured by the SMU | | |
|---|---|---|---|
| mA ± 0.0004 % | Core | Jacket | Shield |
| 0 | 0 ± 20 fW | 0 ± 2 pW | 0 ± 20 pW |
| 1 | 0 ± 300 fW | 0 ± 15 pW | (20.43 ± 0.01) µW |
| 2 | 0 ± 500 fW | 0 ± 40 pW | (83.50 ± 0.02) µW |
| 5 | 0 ± 1.5 pW | 0 ± 100 pW | (528.60 ± 0.05) µW |
| 10 | 0 ± 4 pW | 0 ± 200 pW | (2.1235 ± 0.0002) mW |
| 20 | 0 ± 6 pW | 0 ± 400 pW | (8.5040 ± 0.0005) mW |
| 40 | 0 ± 10 pW | 0 ± 800 pW | (33.922 ± 0.002) mW |
| 80 | 0 ± 20 pW | 0 ± 1.5 nW | (134.46 ± 0.005) mW |
| 160 | 0 ± 40 pW | 0 ± 3 nW | (528.1 ± 0.1) mW |

Table 4.3: Results of the first test showing the heating power measured in each layer as a function of the heating current in the shield. The current in the core and jacket were forced to be at (0 ± 1) nA. The uncertainties presented in this table were estimated to correspond to the standard deviation with a coverage factor of $k = 2$.

Table 4.3 shows that even with increasing the shield heating power, the mean core and jacket heating power does not increase, though the variation about the mean does; it increases relatively linearly with the shield heating current.

| Shield heating current | Heating power measured by the SMU | | |
|---|---|---|---|
| | Core | Jacket | Shield |
| mA ± 0.0004 % | mW ± 0.0001 | mW | |
| 0 | 1.0290 | 4.0450 ± 0.0005 | 0 ± 1.2 nW |
| 1 | 1.0300 | 4.075 ± 0.001 | ( 51.03 ± 0.005 ) µW |
| 2 | 1.0310 | 4.104 ± 0.001 | ( 147.53 ± 0.01 ) µW |
| 5 | 1.0356 | 4.190 ± 0.001 | ( 710.05 ± 0.05 ) µW |
| 10 | 1.0411 | 4.335 ± 0.001 | ( 2.5576 ± 0.0001 ) mW |
| 20 | 1.0509 | 4.620 ± 0.001 | ( 9.6459 ± 0.0003 ) mW |
| 40 | 1.0674 | 5.186 ± 0.001 | ( 37.215 ± 0.003 ) mW |
| 80 | 1.1013 | 6.320 ± 0.001 | ( 144.45 ± 0.03 ) mW |
| 160 | 1.1681 | 8.586 ± 0.001 | ( 557.6 ± 1 ) mW |

Table 4.4: Results of the second test listing the heating power measured in each layer as a function of the heating current in the shield. The current in the core and jacket were forced to be at (0.218000 ± 0.000001) mA and (6.900000 ± 0.000006) mA respectively to approximate typical operating currents. The uncertainties presented in this table were estimated to correspond to the standard deviation of the signal with a coverage factor of $k = 2$.

Passing current through the heating circuits caused a rise in temperature, and a change in the overall resistance of the circuit (around -800 Ω/K for the core and -0.03 Ω/K for the jacket and shield). The variation of resistance was causing a drift in the measured power proportional to the rate of change in temperature. That drift in power due to heating was observed to be much smaller compared to the change due electrical coupling, therefore it

was removed from the measured power levels. All the data presented in this section was corrected for the presence of the drift.

Table 4.4 shows that when the shield current is increased, the heating powers in the other two layers increase. The jacket is more strongly affected than the core; an increase of 4.54 mW is measured in the jacket compared to 0.14 mW in the core when a heating current of 160 mA is passed through the shield. By comparing both tables, it can be seen that the shield does not dissipate the same heating power at a given heating current, which leads one to conclude that the layers are electrically coupled. The physical reason that would explain this behavior is not well understood at this point. It will briefly be covered in the following chapter in section 5.2.

## 4.4. Resistance measurements

In addition to the electrical coupling effect, abrupt changes in heating resistances were also observed and were thought to be responsible for the erratic perturbation described in section 4.1. The figure below depicts one case in which an abrupt drop in shield power was attributed to a change in shield resistance (a constant current was being applied to the shield in this case). An investigation was initiated to identify which part(s) of the heating circuit was responsible for the change in resistance in an effort to resolve the problem.

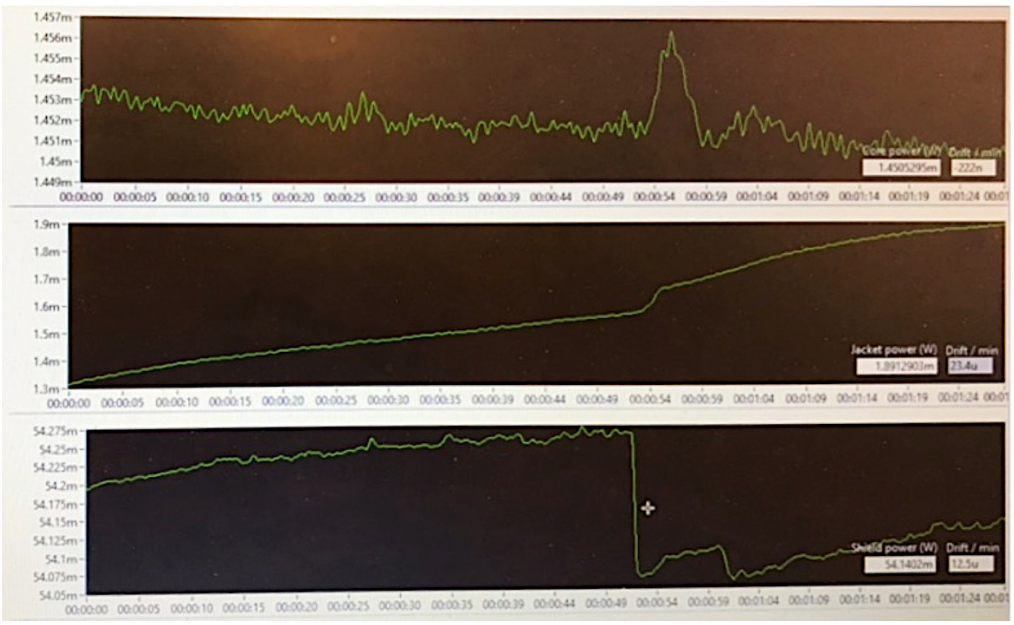


Figure 4.7: Snapshot of the LabVIEW GUI showing an example of resistance instability in the shield and the resulting effect on the other two layers. The three curves from top to bottom correspond to the power dissipated in the core, jacket, and shield, respectively. In this case, the current in the shield was set to a value of 49 mA, and the powers in both the core and jacket were controlled by their respective PIDs. A sudden drop of power is measured in the shield around the 50 s mark, inducing a perturbation in the core and jacket.

The resistance of each heating element was calculated using the current and voltage information provided by the SMUs. For both the shield and the jacket, isolated measurements were made; for the jacket measurement, the heating current for both the core and shield was set to 0 mA and the jacket was set to 5.200 mA. The dissipated power was then recorded for a period of 4 mins. The same procedure was repeated for the shield, with an applied current of 50.00 mA.

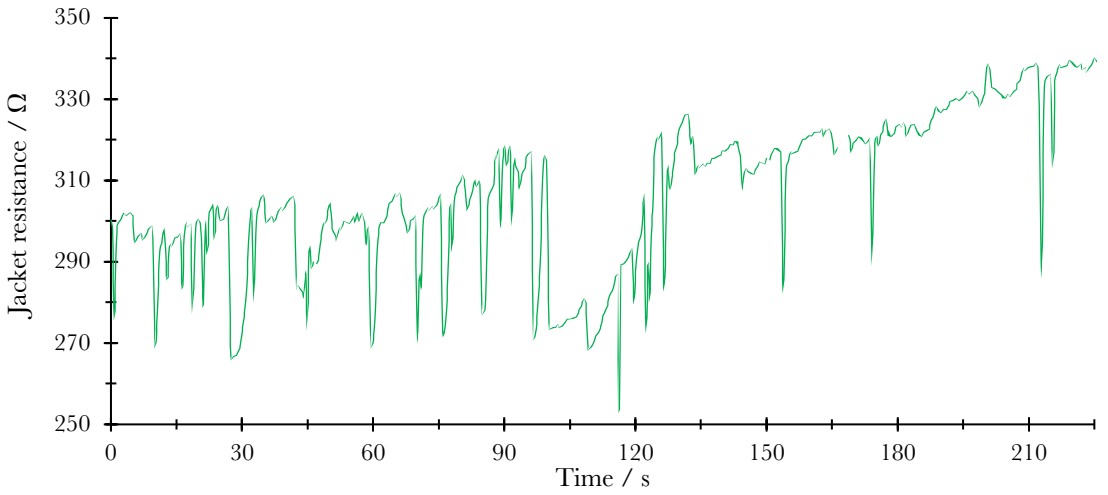


Figure 4.8: Jacket heating resistance as a function of time. The resistance was calculated from the voltage and the current provided by the SMU. A constant heating current of 5.200 mA was set for the jacket, and the other two layers were set to 0 mA.

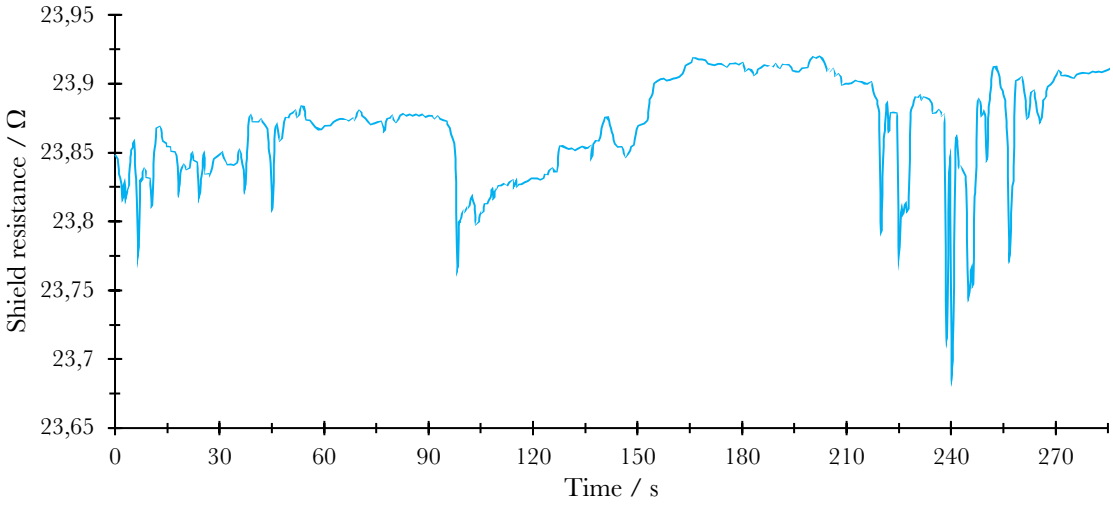


Figure 4.9: Shield heating resistance as a function of time. The current was calculated from the voltage and the current provided by the SMU. A constant heating current of 50.00 mA was set for the shield, and the other two layers were set to 0 mA.

From both figure 4.8 and 4.9, it is clear that the resistance is variable over time in both layers, but the jacket is relatively more unstable compared to the shield; the relative standard deviation over the measurement is 6.1 % and 0.2 % for the jacket and shield respectively.

To verify these results, a second acquisition was made in which all three layer resistances were measured simultaneously. For this measurement, the PID controllers in each layer was enabled to maintain a constant setpoint temperature in each layer. The resistances were once again calculated using the variable current and voltage information measured by the SMUs for each heating circuit.

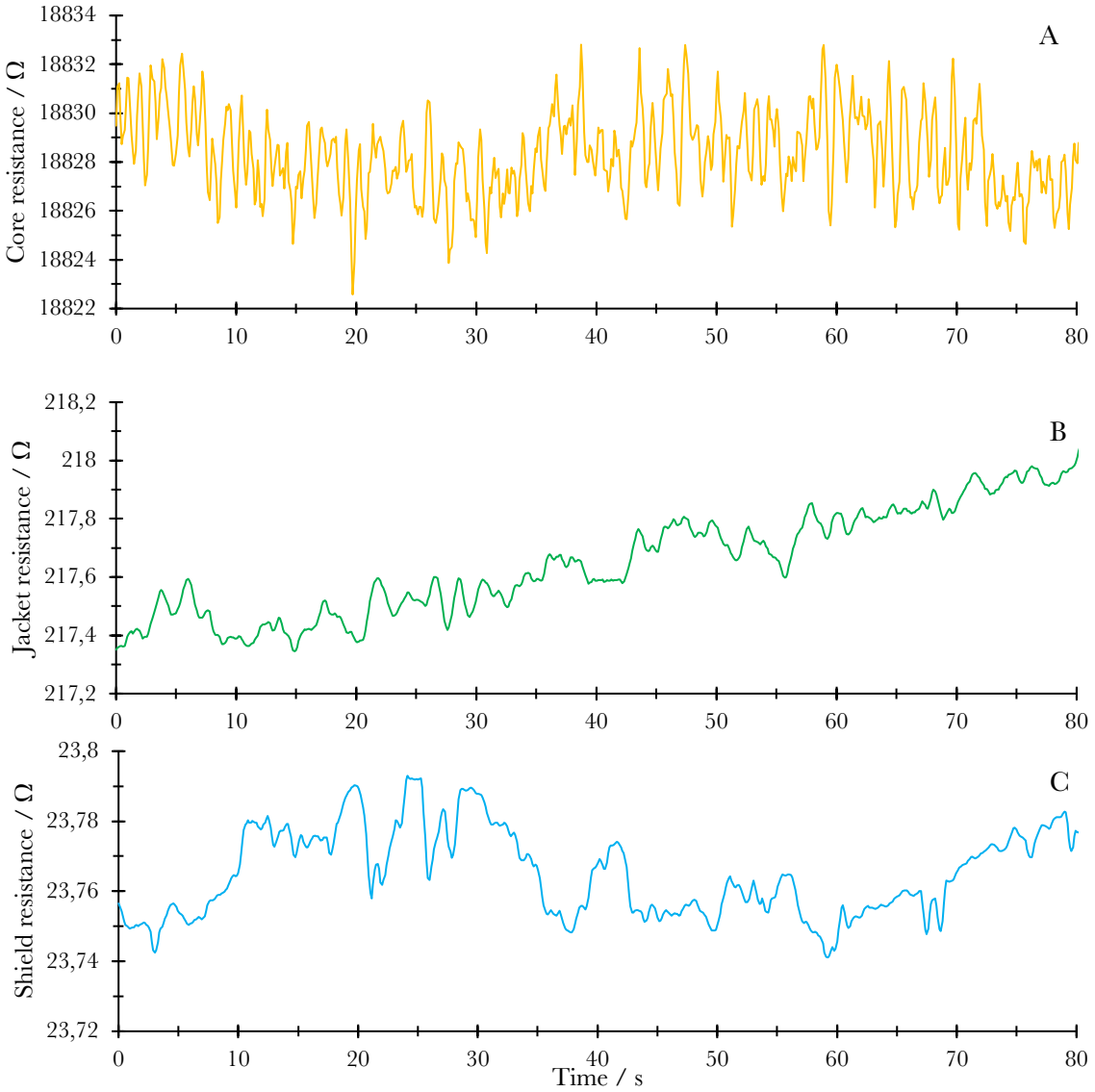


Figure 4.10: Resistance in the three layers as a function of time. The resistances are calculated using the currents and voltages measured by the SMUs. (A), (B) and (C) correspond to the core, jacket and shield layer respectively. The temperature was kept constant in each layer by the PID controllers.

In figure 4.10, the relative standard deviation of the resistance is 0.009 %, 0.08% and 0.05% for the core, jacket, and shield respectively. There is a substantial difference in the shape and relative standard deviation between the two experiments, especially for the jacket. Such a large discrepancy could point to a potentially poor electrical connection.

The resistance of the 50 feet long leads connecting the probe to the SMUs was measured for each of the core, jacket, and shield, along with common ground lead. Using a Keithley multimeter 2002, the resistance of each lead was measured individually as a function of time by connecting a probe to each end of the cable. Figure 4.11 below shows the results.

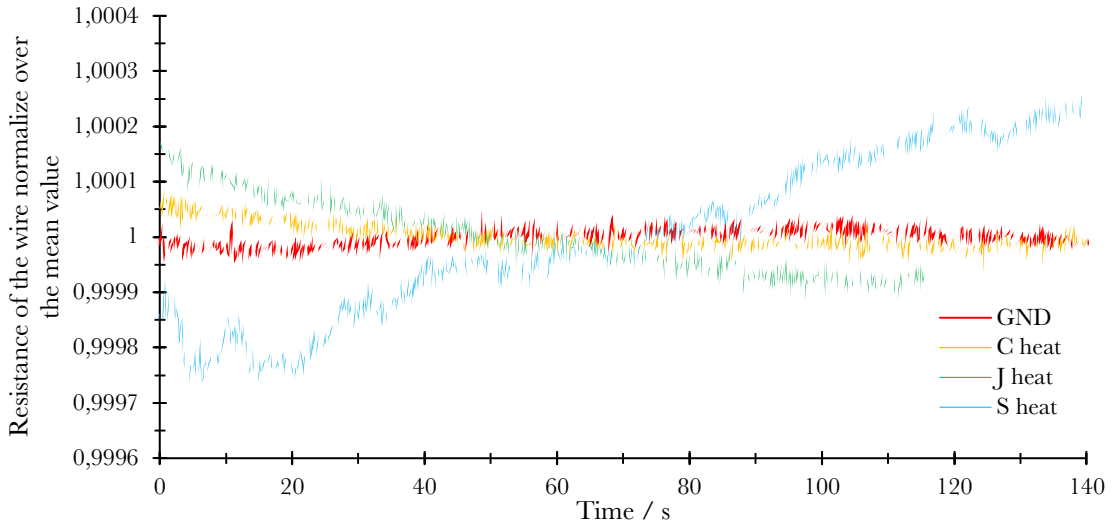


Figure 4.11: Measured resistances as a function of time of the four leads in the 50-ft long cable that is used to connect the probe to the SMUs. GND correspond to the ground common to all three heating circuits. C heat, J heat, and S heat correspond to the core, jacket, and shield positive heating wire, respectively. The signals were normalized for a better representation of the relative variation over time.

The mean measured resistances are 4.16 Ω, 4.15 Ω, 4.21 Ω, 4.41 Ω for the GND, C heat, J heat, and S heat, respectively. Following the same order, the relative standard deviations

of each signal are 0.0018 %, 0.0025 %, 0.007%, and 0.012 %. Figure 4.11 shows that the wire resistances are stable to within ± 0.01% over a period of more than 2 mins, except for the shield wire which is changing within ± 0.03%. In addition, the resistance changes were relatively slow and smooth, unlike the sharp variations as seen previously in figure 4.8 and 4.9. Further measurements were needed to gain a better understanding of the observed resistance variations. Additional resistance measurements were performed, lack of repeatability and consistency between identical or similar measurement sets were seen, nevertheless similar behaviors were observed.

During this period of investigation, the jacket heating circuit suffered a gradual, and eventually, a complete loss of connection. Typical measured resistances went from around 200 Ω to tens of kΩ, to finally > 1 MΩ. This strongly suggests that one or both of the heating wires has been disconnected from the jacket graphite. Losing that heating connection meant that active control of the jacket, and thus isothermal mode measurements, would no longer be possible with that probe. The gradual loss of this connection could potentially explain the lack of repeatability and consistency observed prior to the complete failure of the jacket heating circuit.

## 4.5. Adiabatic measurements

### 4.5.1. Preliminary measurements

Since operating in isothermal mode was no longer an option, the focus was shifted to performing adiabatic mode measurements. The probe was waterproofed using a rubber spray (Plasti-dip™) for submerged use. The thermistors were recalibrated as before in the

range of -2 °C to 12 °C, since the intention was to use the probe in 4 °C water (like a water calorimeter).

Figure 4.12: Photo of the waterproofed probe. A red rubber layer was applied using a liquid rubber spray (Plasti-dip). Five coats were applied to ensure no leaks.

The first set of preliminary measurements were performed on the February 10th, 2019 at the MUHC on a clinical Varian TrueBeam™ linac. An in-house built temperature-controlled water phantom[2] (normally used for water calorimeter measurements) was used to achieve the high level of thermal stability (typically better than 1 mK/min) required for adiabatic measurements. The phantom SSD was fixed at 92.7 cm, since it was placed on a non-adjustable heavy-duty cart. Within the phantom, the probe was positioned at a depth of 10 cm and was aligned with the beam central axis using the light field. Once stabilized, the water temperature was nominally maintained at 4.12 °C. Four different high-energy

photon beams were used: 6 MV, 10 MV, 6 MV FFF and 10 MV FFF. Irradiations from (5 – 30) s were acquired for jaw-defined field sizes ranging in size from 10 × 10 $cm^2$ to 2 × 2 $cm^2$.

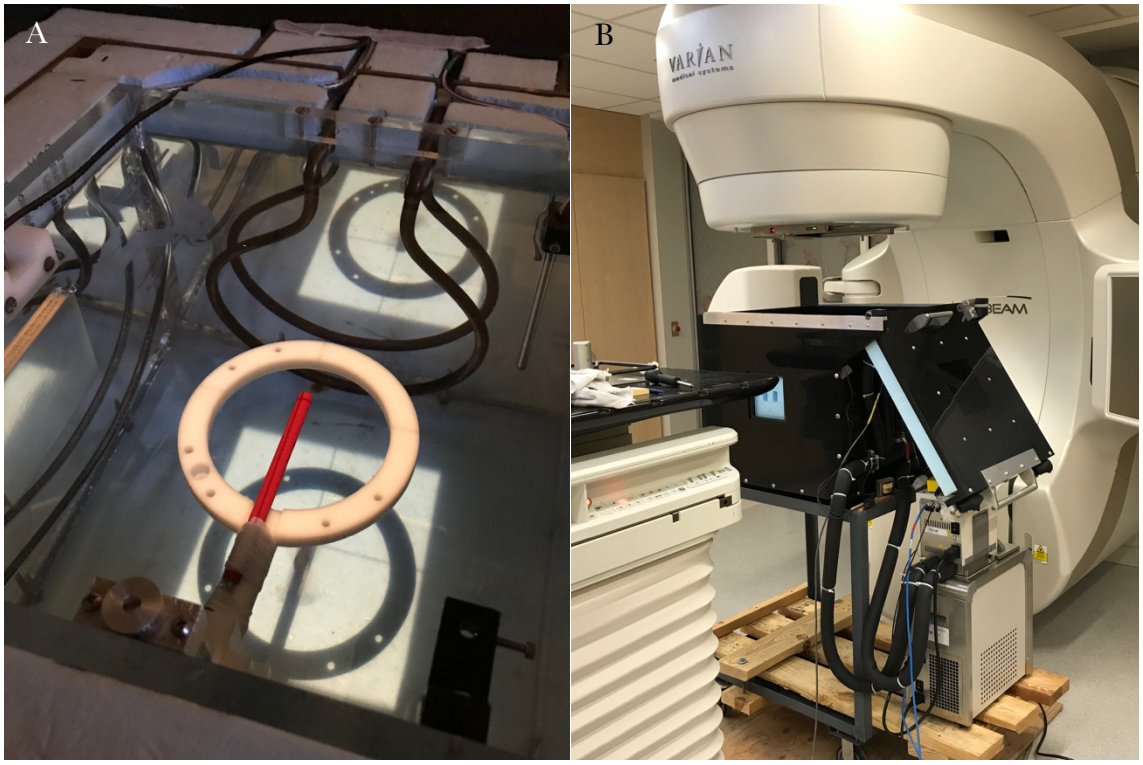


Figure 4.13: Experimental set-up for the adiabatic measurement. (A) The center of the probe (red) is placed at the center of a 10 × 10 $cm^2$ jaw-defined field and at a depth of 10 cm in the water phantom. The adiabatic measurements were done with the phantom lid closed (lid shown in B hanging off the side of the phantom). (B) Overview of the temperature-controlled water phantom placed under the linear accelerator just before measurement.

Upon initial acquisition, it was observed that the temperature signal as a function of time was not shaped as expected. Figure 4.14 shows an example of an acquisition using a 6 MV beam at 600 MU/min with 300 MU.

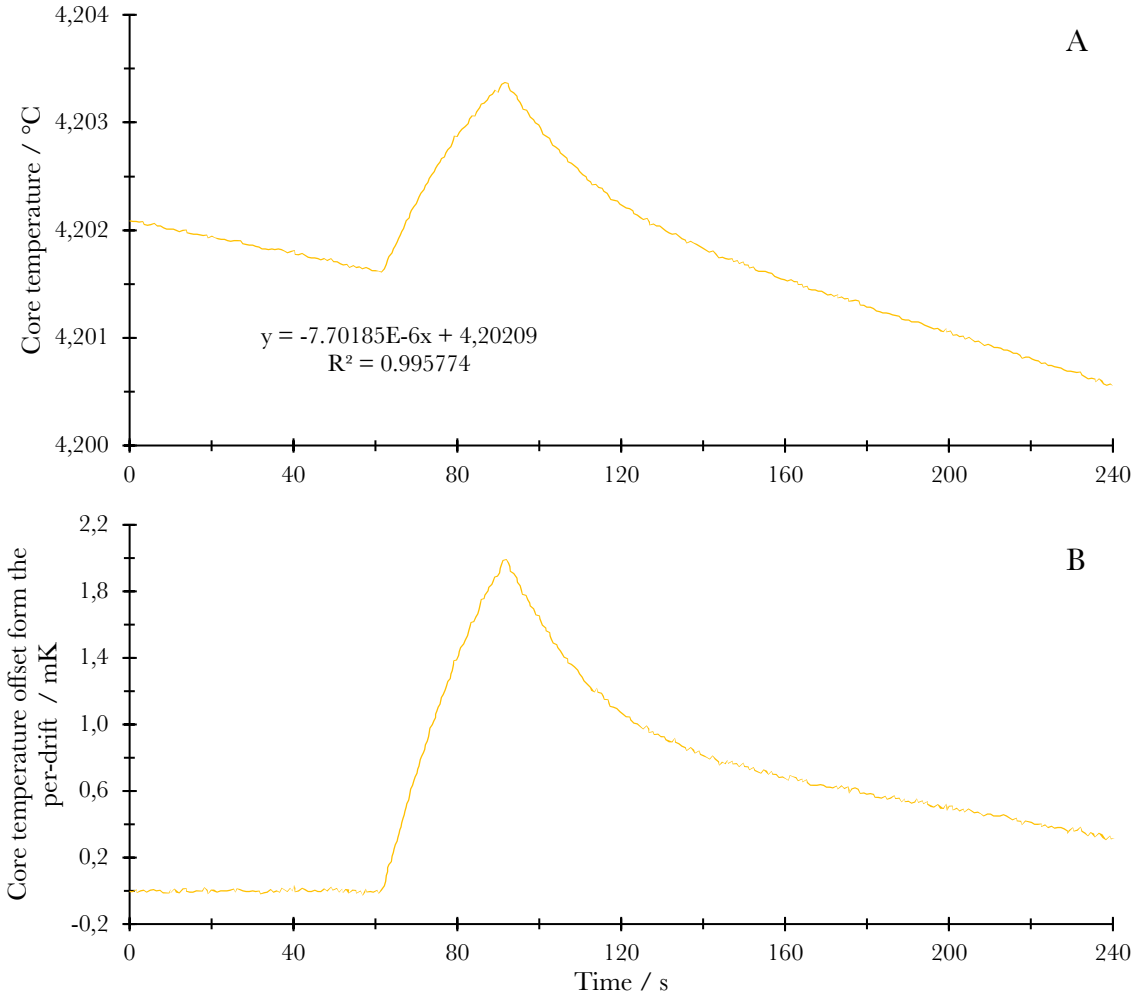


Figure 4.14: Representation of the adiabatic temperature signal. (A) Raw signal of a 30 s irradiation of 6 MV beam at 600 MU/min. A linear fit was made on the first 62 s of the run. (B) Core signal with the pre-drift slope subtracted. The curve is non-linear, which makes the conventional analysis method based on extrapolation impossible.

For ideal adiabatic mode operation, a linear temperature rise during the beam-on period, assuming a constant dose rate, followed by a generally linear post-drift. As seen in figure 4.14.B, the beam on portion of the plot exhibits non-linearity, followed by a decay-shaped fall off. This behavior is most likely due to the heat transfer occurring between the core and the adjacent layers as well as with the cooler surrounding water phantom. The specific heat capacity of water is around six times larger than that of graphite, resulting in a rate of

heating that is six times less than the graphite within the probe. These results suggest that Aerrow-mini contains insufficient thermal insulation to acquire and analyze adiabatic measurements in the conventional way. This isn't unexpected, as Aerrow-mini was originally conceived to be used exclusively in isothermal mode.

### 4.5.2. Dose calculation

In light of the non-linear nature of the temperature acquisitions, an alternative way of analyzing the data was proposed. It consists of using the slope of the beam-on portion of the signal to calculate the dose rate at the beginning of the irradiation and combining that with the duration of the irradiation to determine the dose. In using this method, the assumption that the dose rate is constant throughout the irradiation period is being made. This proposed analysis method is justified since the probe is initially in thermal equilibrium with the surrounding water, therefore, the effects of heat transfer on the measured temperature should be minimized at the very beginning of irradiation. Practically, to calculate the dose rate at the beginning of the irradiation, the pre-drift slope is first removed from the entire signal (herein referred to as the 'corrected' signal), and then the beam-on portion of the signal is fitted with a second-order polynomial. Using the derivative of the polynomial fit, the rate of temperature rise, and hence the dose rate at the beginning of irradiation can be calculated. A second-order polynomial was deemed appropriate since the derivative of the corrected core temperature as a function of time is reasonably linear during the beam-on period, as shown in figure 4.15.

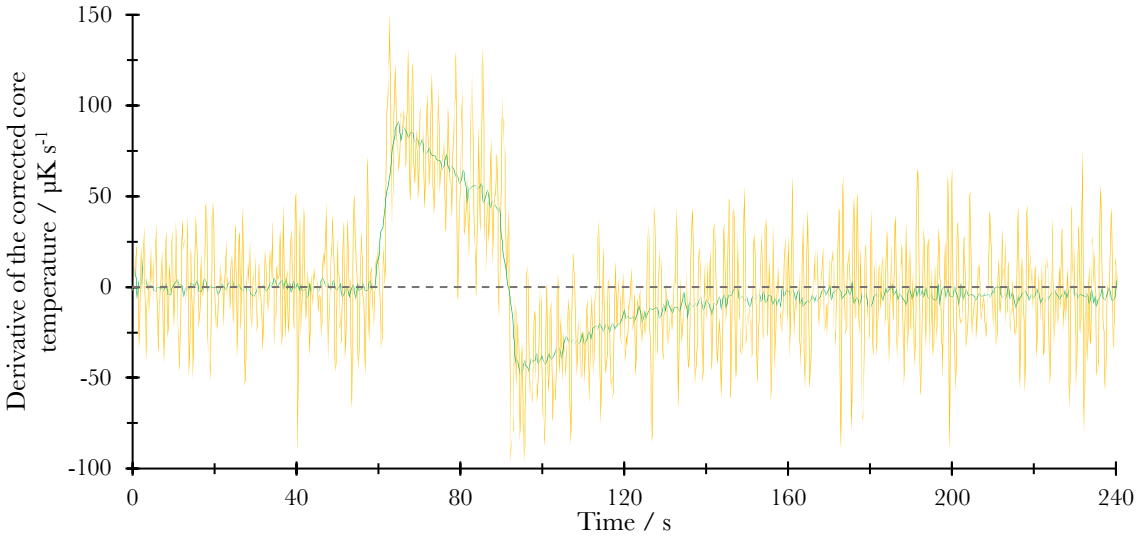


Figure 4.15: Derivative of the corrected core temperature as a function of time for a 300 MU 6 MV photon beam at a repetition rate of 600 MU/min. The orange line represents the raw data, and the green line represents a moving average over a period of 40 points (approximately 4 seconds).

A MATLAB code was then written to automate this process. The steps implemented in the code are as follows:

A. Identify the beginning of the irradiation
    1. Enter an approximation of the pre-drift time slightly lower that the exact value. A precision on the order of 10 seconds is enough.
    2. Fit a 1st order polynomial to the pre-drift (Fit A), excluding some of the last points close to the irradiation. (This fit if only used to identify the beginning of the irradiation.)
    3. Subtract the pre-drift from the entire signal.
    4. Identify the beam-on point by identifying the time at which the signal increases beyond a defined threshold (approximately 2σ of the noise level of the pre-drift)
B. Remove the pre-drift exactly 30 seconds before the irradiation
    1. Fit a 1st order polynomial on 30 seconds previous to the identified start of the irradiation (Fit B). (Only 30 seconds are used to improve the accuracy of the estimation of the temperature drift during the beam-on time.)

2. Correct the signal using Fit B.

C. Calculate the dose rate at the beginning of the irradiation

1. Fit a 2nd order polynomial on the first 14 seconds of the irradiation portion of the signal (Fit C). (14 seconds are used to make sure that only points within the irradiations (approximately 15 seconds) are used in the dose calculations.)
2. Calculate using the fit the moment where it crosses the pre-drift fit, i.e. the zero of the function. (This step is used to make sure that the dose rate is always calculated at the same point, i.e. is less dependent on the identified beginning of irradiation point.)
3. Take the first derivative of Fit C.
4. Calculate the dose rate using the derivative at the zero of the fit.
5. Calculate the duration of the beam using the maximum point of the corrected signal and the previously identified irradiation start time.
6. Calculate the dose using the measured time of irradiation and dose rate.

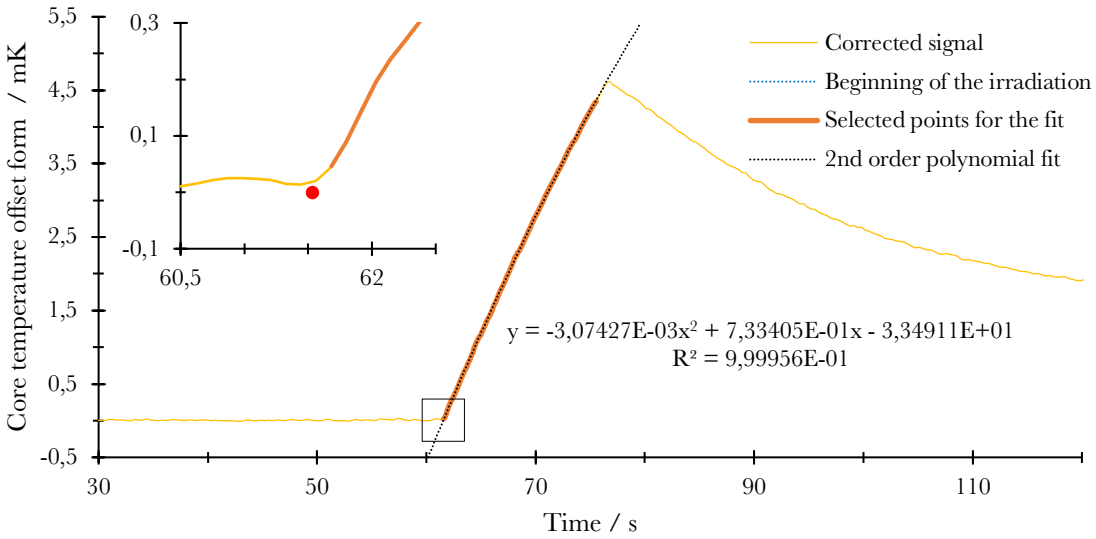


Figure 4.16: Representation of the dose calculation (step B and C of the code). The data correspond to a 15 second irradiation of a 10 FFF beam at 2400 MU/min at SSD 100 cm with a field size of 10 × 10 cm². The zoomed portion shows the point (red) where the dose rate is calculated.

This analysis method was conceived based on the initial adiabatic data set, but in order to verify the accuracy of this proposed approach, a second set of adiabatic measurements was needed. On May 11th, 2019, at the MUHC on a clinical Varian TrueBeam™ linac, adiabatic measurements were acquired using the same temperature-controlled water phantom setup as described in section 4.5.1. The SSD was placed at 100 cm and the center of the detector was positioned at a depth of 10 cm. The detector was placed horizontally with respect to the beam and its center aligned with the beam axis using the linac light field. The measurements were acquired in a water temperature ranging between 4.32 °C to 4.46 °C over a 3 hours period. Three set of measurements were taken: (i)600 MU, 10 MV FFF photon beam at 2400 MU/min with a field of 10 × 10 $cm^2$, (ii) 350 MU, 6 MV FFF photon beam at 1400 MU/min with the same field as before, and (iii) 600 MU, 10 MV FFF photon beam at 2400 MU/min with a field of 2 × 2 $cm^2$. For all three, 15 second irradiations were chosen because it was a trade-off between the amount of usable data and the amount of non-linearity, which increases with beam on time. Shorter irradiations also result in a quicker return to thermal equilibrium, reducing the wait time in between runs.

The following day, ionization chamber measurements were performed under the same conditions as the calorimeter, with the exception that the water phantom was at room temperature. An Exradin A1SL (Standards Imaging Inc., Madison WI) with an absorbed dose calibration traceable to the primary standard lab (National Research Council Canada) was used to determine absorbed dose to water by following the AAPM TG-51[7] (and addendum[6]) protocol. The following table (4.5) summarizes the dose comparison between the A1SL and Aerrow-mini measurements.

| | 10 MV FFF | 6 MV FFF | 10 MV FFF |
|---|---|---|---|
| | $10 \times 10$ cm$^2$ | $10 \times 10$ cm$^2$ | $2 \times 2$ cm$^2$ |
| | Dose to water at $z_{max} \pm k = 1$ | | |
| Aerrow-mini | 100.8 ± 1.0 % | 100.8 ± 1.1 % | 84.4 ± 1.3 % |
| A1SL | 100.4 ± 1.1 % | 100.3 ± 1.1 % | 84.5 ± 1.3 % |
| Difference | 0.4 % | 0.5 % | 0.1 % |

Table 4.5: Dose comparison between Aerrow-mini used in adiabatic mode and the Exradin A1SL used following the AAPM TG-51 protocol[7]. The 10 MV FFF beams were used at 2400 MU/min and 600 MU were delivered in total. The 6 MV FFF beam was used at 1400 MU/min and 350 MU were delivered in total. Doses for Aerrow-mini were corrected for heat transfer and the presence of impurities (detail in section 4.7 and 4.6.4 respectively). Aerrow-mini $2 \times 2$ cm$^2$ value was corrected for small fields using the $k^{f_{clin},f_{msr}}_{Q_{clin},Q_{msr}}$ (section 4.6.3). An uncertainty of 0.2 % was added to the uncertainty budget of the A1SL at $2 \times 2$ cm$^2$ to account for the small field perturbation effect[9]. Both for Aerrow-mini and the A1SL chamber, no FFF correction were needed, because according to TRS-398[8], a collecting volume with a length below 5 mm will present a volume averaging effect below 0.05% in FFF beam compare to flat fields.

As seen in table 4.5, the dose to water measured by the ionization chamber and Aerrow-mini for both beams agree within the combined uncertainties. An estimated uncertainty budget is presented in the following table (4.6).

| Source of uncertainty | Type A [%] | Type B [%] |
|---|---|---|
| SSD setting | 0.2 | |
| Depth setting | 0.2 | |
| Field-size setting | 0.2 | |
| Linac stability | 0.2 | |
| Reproducibility | 0.1 | |
| Thermistor calibration | | 0.2 |
| Dose conversion factor | | 0.4 |
| Specific heat capacity | | 0.7 |
| Heat transfer correction | | 0.2 |
| Impurity correction | | 0.2 |
| Quadratic summation | 0.4 | 0.9 |
| Total uncertainty on $D_w$ | 1.0 | |

Table 4.6: Estimated uncertainty budget for the determination of dose to water using the adiabatic mode of operation. The presented uncertainty corresponds to a coverage factor of $k = 1$. All of the type A uncertainties were estimated using TG-51 addendum[6] as reference. The thermistor calibration uncertainty estimation reflects the uncertainty associated with the fit on the collected data[1]. The dose conversion factor uncertainty estimation reflects the uncertainty associated with the statistical and inherent (e.g., cross sections) nature of the Monte Carlo calculation[1]. The specific heat capacity uncertainty was estimated based on data in the literature. Finally, both corrections uncertainties were estimated using a rough sensitivity analysis, though refinement is needed to achieve a higher level of confidence.

The data suggests that Aerrow-mini can be used perform absorbed dose to water measurements with an accuracy comparable to a calibrated reference class ionization chamber. Furthermore, these results support the validity of the Monte Carlo model of the probe as well as the proposed analysis method. Further discussion on both of these points is provided in the next chapter.

## 4.6. Monte Carlo simulation

Monte Carlo simulations were used at different stages of the project as a tool to score dose deposition inside the probe. Using EGSnrc with the egs_chamber user code, the probe was modeled according to the measured dimensions during construction and placed in a 30 × 30 × 30 $cm^3$ water phantom with an SSD of 100 cm at a depth of 10 cm. Both the horizontal and vertical probe orientations were simulated. This section presents all the simulations performed throughout the project and the associated results.

The Monte Carlo parameters commonly used by the different simulation are presented in the following. NIST ESTAR density corrections were used to generate PEGS4 datasets for all materials. XCOM photon cross sections were used throughout. The transport parameters were set to: ECUT & AE = 512 keV, PCUT & AP = 1 keV, SMAX = $10^{10}$, ESTEPE = 0.25, XIMAX = 0.5, EM ESTEPE = 0.02 & 0.01 for Aerrow and phantom, EXACT boundary cross algorithm, and PRESTA II electron-step algorithm. The variance reduction technique parameters were: photon cross section enhancement factor = 16, russian roulette survival factor = 256, and ESAVE = 512 keV.

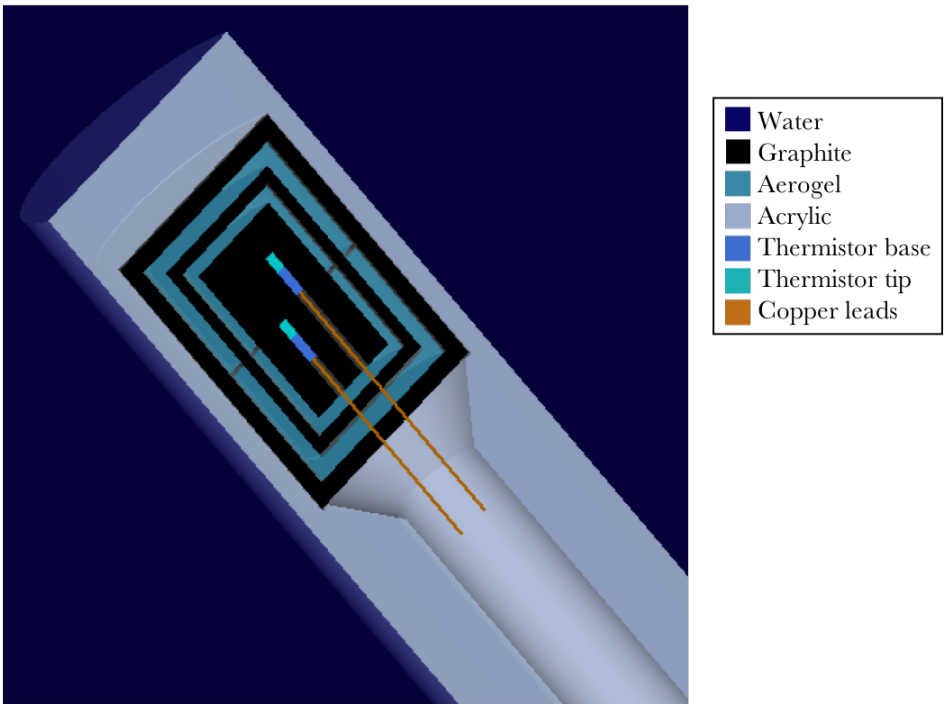


Figure 4.17: Screenshot of the probe egs++ class library model of Aerrow-mini viewed in the egs-view GUI. Inside the core, two thermistors with copper leads were added for accurate dose calculation.

### 4.6.1. Dose at a point in water

The first set of Monte Carlo simulations were performed to establish the appropriate size of the water scoring volume to best approximate dose at a point. In this case, the aim was to score the dose in the detector sensitive volume and compare it with the dose score at "a point" in water centered at the same location in the absence of the detector. For these broad photon beam Monte Carlo simulations, a thin water disk is used as the scoring volume; as the disk is decreased in size, the dose scored in the volume more closely approximates the concept of dose a point in water. Since one aim of this project was to simulate the detector response in small photon fields, a verification of the thin water disk dimensions was performed down to the smallest fields used in the clinical environment (i.e. $0.5 \times 0.5$ cm$^2$).

The verification was done by varying the radius of the 0.25 mm thick disk for two different field size: (1) 10 × 10 $cm^2$, which is the reference condition field size, and (2) at 0.5 × 0.5 $cm^2$, which is the smallest field used in the clinic. The scoring volume was placed in a 30 × 30 × 30 $cm^3$ water phantom at a depth of 10 cm. The radiation source used was a BEAMnrc model of a Varian Novalis linear accelerator 6 MV photon beam, which has been previously validated for field sizes down to 0.5 × 0.5 $cm^2$.[4] The radius was varied in the range of 2 cm to 0.05 cm for the 10 × 10 $cm^2$ field and 1 cm to 0.01 cm for the 0.5 × 0.5 $cm^2$ field. The figure below summarizes the results of these simulations.

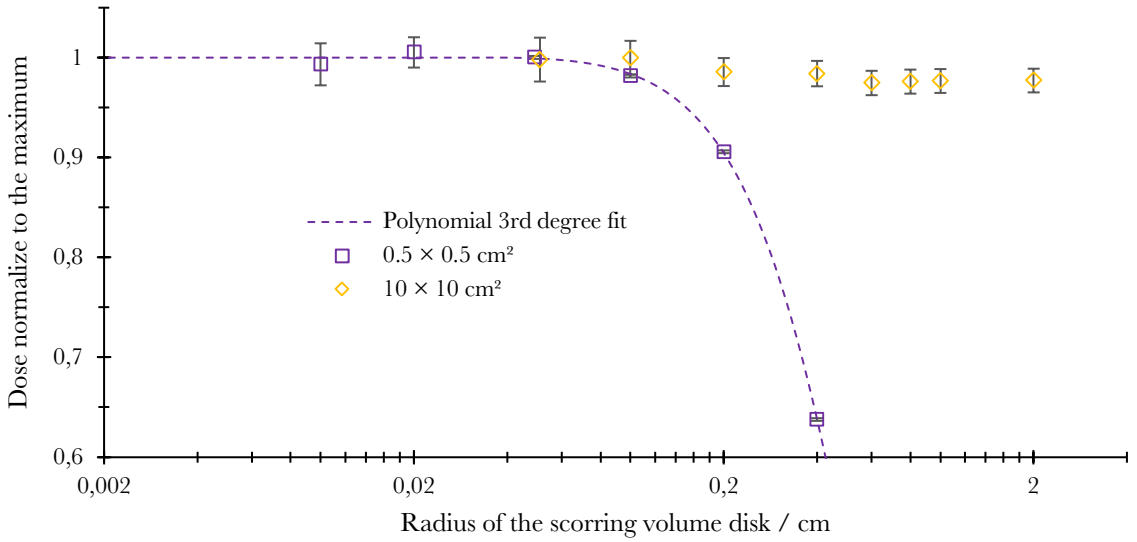


Figure 4.18: Dose normalized to its maximum scored dose as a function of the radius of the scoring volume disk. A 3rd degree polynomial was fit to the seven smallest simulated radii for the 0.5 × 0.5 $cm^2$ field dataset. Some of the points for the 0.5 × 0.5 $cm^2$ field lie beyond the range limits of the graph (> 0.4 cm radius). The error bars shown represent a coverage factor of $k = 2$.

A disk radius of 1 cm was used for the 10 × 10 $cm^2$ as used by other in the same conditions[1]. For the 0.5 × 0.5 $cm^2$ field, increasing the radius beyond 0.1 cm has a relatively large effect

on the scored dose. Using the fit, the maximum radius that results in a scored dose that is within 0.1% of the maximum is 0.051 cm, therefore a radius of 0.05 cm was used in the subsequent dose calculations involving field between 0.5 × 0.5 $cm^2$ and 2 × 2 $cm^2$. The threshold of 0.1% was chosen as the evaluation criteria, since this is the desired type A uncertainty for each simulation.

### 4.6.2. Dose conversion factors

Dose conversion is a required step in determining absorbed dose to water when using any graphite calorimeter. The dose conversion factor is used to convert the dose absorbed in the sensitive graphite volume of the probe to a dose to a point of water centered at the same location in the absence of the probe.

Dose to the core was calculated for four different high-energy photon beam models and was then compared to the dose scored in a water disk of a thickness of 0.03 cm and a radius of 0.5 cm and 1 cm for FFF beam and WFF (with flattening filter) beams, respectively. The four inhouse beam models were commissioned on Varian TrueBeam™ golden data for the 6 MV FFF, 6 MV, 10 MV FFF, and 10 MV beam[10].

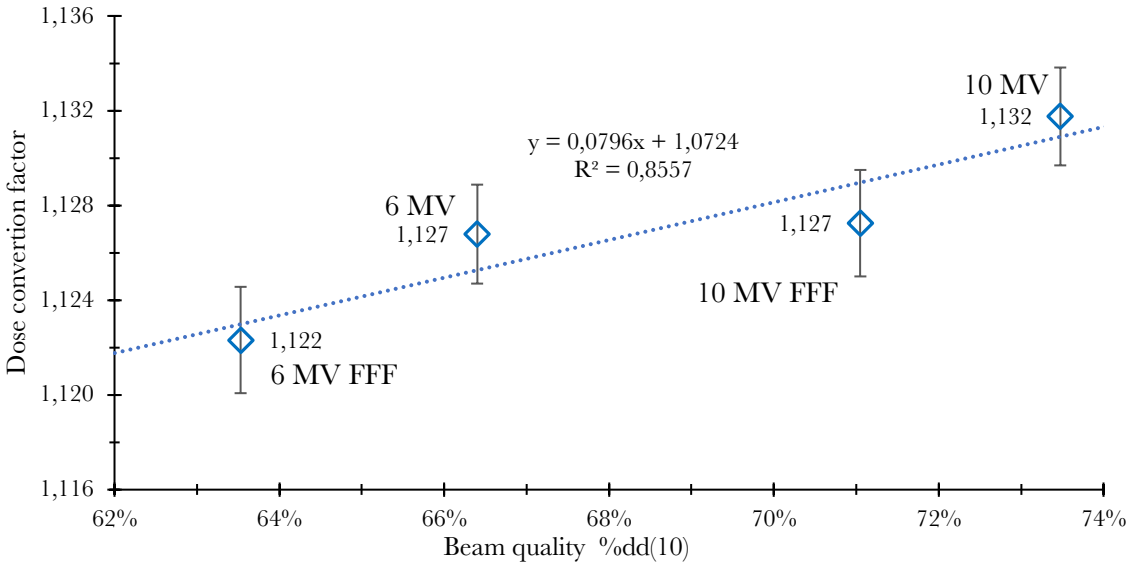


Figure 4.19: Dose conversion factors for the four different beam qualities studied with the probe oriented in a horizontal configuration. The simulated probe was positioned at a depth of 10 cm in water with a 10 × 10 cm$^2$ field and an SSD of 100 cm. The error bars shown represent a coverage factor of $k = 2$.

### 4.6.3. Small field output correction factor $k^{f_{clin},f_{msr}}_{Q_{clin},Q_{msr}}$

As explained in section 1.4.4, a correction factor needs to be applied when a detector is used in small fields. In this work, these field-specific factors were calculated using the Monte Carlo model described in section 3.5.1. The field (always defined at 100 cm from the source) was varied in the range of 10 × 10 cm$^2$ to 0.45 × 0.45 cm$^2$ in an SSD 100 cm setup. The dose to the water disk and to the detector core were scored for each field, and from those results, small field output correction factors were calculated using equation 1.15. The detector was simulated in the vertical orientation to minimize the volume averaging effect due to the radial non-uniformity of the beam. The source model used was the same as the one described in section 3.5.1.

| Field size | $k_{Q_{clin},Q_{msr}}^{f_{clin},f_{msr}}$ |
|---|---|
| $cm^2$ | ± 0.15 % |
| 10 × 10 | 1.000 |
| 5 × 5 | 1.002 |
| 3 × 3 | 1.001 |
| 2 × 2 | 0.999 |
| 1 × 1 | 0.992 |
| 0.8 × 0.8 | 0.990 |
| 0.55 × 0.55 | 0.996 |
| 0.5 × 0.5 | 1.007 |
| 0.45 × 0.45 | 1.015 |

Table 4.7: Aerrow-mini field output correction factors, $k_{Q_{clin},Q_{msr}}^{f_{clin},f_{msr}}$, for 6 MV photon fields with the probe in the vertical orientation at a depth of 10 cm. The stated uncertainty (coverage factor $k = 1$) is the combined type A uncertainty as calculated by the Monte Carlo code.

Table 4.7 lists the calculated field output correction factors with a stated type A uncertainty associated with the Monte Carlo simulated. The function shown in equation 4.1 was fit to the data, the result of which is shown in the figure (4.20) below.

$$f(x) = (1 + e^{-ax+b})(1 - e^{-cx+d}) \qquad (4.1)$$

The coefficients obtained for the fit were: a = 7.073, b = 0.2413, c = 2.480, and d = -2.235.

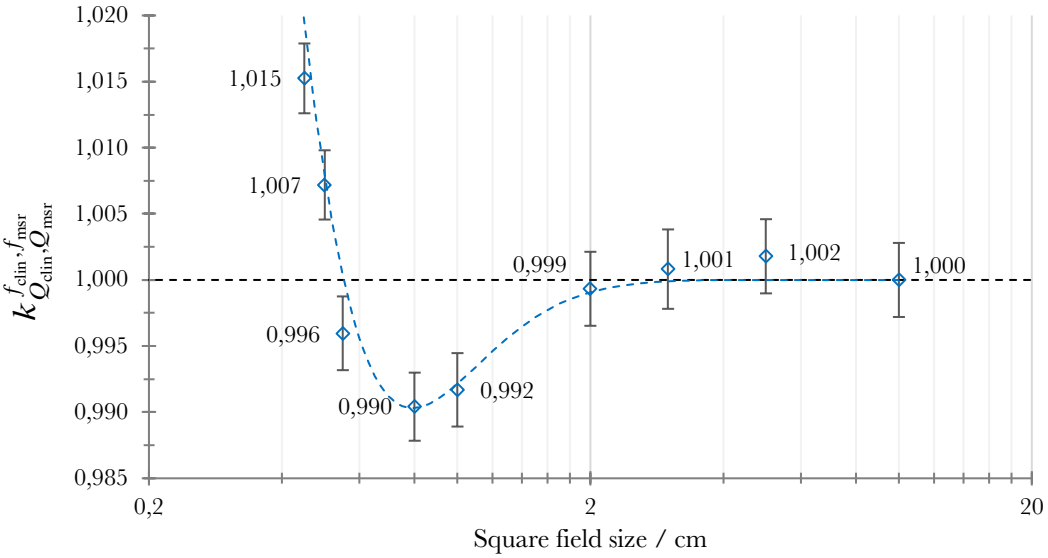


Figure 4.20: Aerrow-mini field output correction factors, $k_{Q_{clin},Q_{msr}}^{f_{clin},f_{msr}}$, for a 6 MV photon beam as a function of field size. The fields are defined at 100 cm from the source and the probe is placed at a depth of 10 cm in the vertical orientation. The error bars shown represent the type A uncertainty with a coverage factor of $k = 2$. The dotted line shown the fitted function shown in equation 4.1.

Using the fit, the effect of field size uncertainty on the field output correction factor was calculated. The impact on $k_{Q_{clin},Q_{msr}}^{f_{clin},f_{msr}}$ due to an absolute field size uncertainty of ± 0.5 mm as a function of field size was calculated for fields of 1 × 1 cm$^2$ and smaller. These results are summarized in table 4.8.

| Field size / cm$^2$ | Uncertainty on $k_{Q_{clin},Q_{msr}}^{f_{clin},f_{msr}}$ |
|---|---|
| 1 × 1 | 0,06% |
| 0.9 × 0.9 | 0,05% |
| 0.8 × 0.8 | 0,004% |
| 0.7 × 0.7 | 0,11% |
| 0.6 × 0.6 | 0,4% |
| 0.5 × 0.5 | 1,0% |

Table 4.8: Uncertainty on $k_{Q_{clin},Q_{msr}}^{f_{clin},f_{msr}}$ due to an absolute uncertainty of ± 0.5 mm on each dimension of the square field as a function of the field size.

Table 4.8 suggests that the jaws positioning uncertainty only becomes an important factor to consider for field sizes of 0.6 × 0.6 $cm^2$ and smaller.

### 4.6.4. Impurity correction

As explained in section 2.5, an impurity correction must be applied to account for the non-graphite materials in proximity to the sensitive volume. Using the EGSnrc model, the dose was scored in each component (the core, the aerogel jacket, the thermistor tip and base, and the thermistor leads) with the Novalis[4] 6 MV photon beam at SSD of 100 cm with the probe in the vertical orientation positioned at a depth of 10 cm. Using equation 2.8, the impurity correction $k_{imp}$ was calculated for various field sizes, with a particular focus on the smallest fields of interest. Table 4.9 summarizes the results of this study.

| Field size | $k_{imp}$ | $k_{Q_{clin},Q_{msr}}^{f_{clin},f_{msr}}$ | $k_{total}$ |
|---|---|---|---|
| $cm^2$ | ± 0,1 % | ± 0,15 % | ± 0,2 % |
| 10 × 10 | 0,999 | 1.000 | 0,999 |
| 2 × 2 | 1,001 | 0.999 | 1,000 |
| 0.55 × 0.55 | 1,013 | 0.996 | 1,009 |
| 0.5 × 0.5 | 1,015 | 1.007 | 1,022 |
| 0.45 × 0.45 | 1,017 | 1.015 | 1,033 |

Table 4.9: Aerrow-mini impurity correction factor at small fields for a 6 MV beam with the probe in the vertical orientation at a depth of 10 cm. $k_{total}$ is the product of $k_{imp}$ and $k_{Q_{clin},Q_{msr}}^{f_{clin},f_{msr}}$. The stated uncertainties correspond to a coverage factor of $k = 1$.

The results show that $k_{imp}$ is negligible within uncertainties for fields sizes down to at least 2 × 2 $cm^2$. At the smallest fields, $k_{imp}$ becomes an important correction and increases the uncertainty associated with the assignment of the total correction factor.

### 4.6.5. Layer perturbation

In order to have a better understanding of the individual effects of each layer of the detector response in small fields, several Monte Carlo simulations were performed using the EGSnrc model. By changing the material of each layer into water, one layer at a time, and scoring the dose to the sensitive volume, the perturbation due to the presence of each individual layer, $P_j$, can be calculated[5]. For the last step, the dose scored in the sensitive volume of the core was compared to the dose scored in a small disk of water to provide a measure of the volume averaging, $P_{vol}$ , of the probe. The product of all the perturbation factors, including the volume averaging, is equal to the dose conversion factor for that radiation field.

$$P_j = \frac{D_{j-1}}{D_j} \qquad (4.2)$$

$$P_{vol} = \frac{D_w}{D_{vol,w}} \qquad (4.3)$$

$$\prod_{j=1}^{N} P_j P_{vol} = \frac{D_{N-1} D_{N-2} \ldots D_1 D_{vol,w} D_w}{D_N D_{N-1} \ldots D_1 D_{vol,w}} = \frac{D_w}{D_{vol,N}} = f_{clin}^{D_{core} \rightarrow D_w} \qquad (4.4)$$

$$P_{j,Q_{clin},Q_{ref}}^{f_{clin},f_{ref}} = \frac{P_{j,Q_{clin}}^{f_{clin}}}{P_{j,Q_{ref}}^{f_{ref}}} \qquad (4.5)$$

$$P_{vol,Q_{clin},Q_{ref}}^{f_{clin},f_{ref}} = \frac{P_{vol,Q_{clin}}^{f_{clin}}}{P_{vol,Q_{ref}}^{f_{ref}}} \qquad (4.6)$$

$$\prod_{j=1}^{N} P_{j,Q_{clin},Q_{ref}}^{f_{clin},f_{ref}} P_{vol,Q_{clin},Q_{ref}}^{f_{clin},f_{ref}} = k_{Q_{clin},Q_{ref}}^{f_{clin},f_{ref}} \qquad (4.7)$$

The subscript *j* indicates the layer and/or component of the detector that is investigated; *j*-1indicate the layer above. $P_{j,Q_{clin},Q_{msr}}^{f_{clin},f_{msr}}$ correspond to the relative layer perturbation factor of the clinical field in respect to the reference field.

For four different field size (10 × 10 cm², 2 × 2 cm², 0.8 × 0.8 cm², and 0.5 × 0.5 cm²), the Novalis[4] 6 MV beam at SSD 100 cm with the probe in the vertical orientation positioned at a depth of 10 cm in a standard water phantom, the probe layers were changed to water one by one, and in each case the dose in the core was scored.

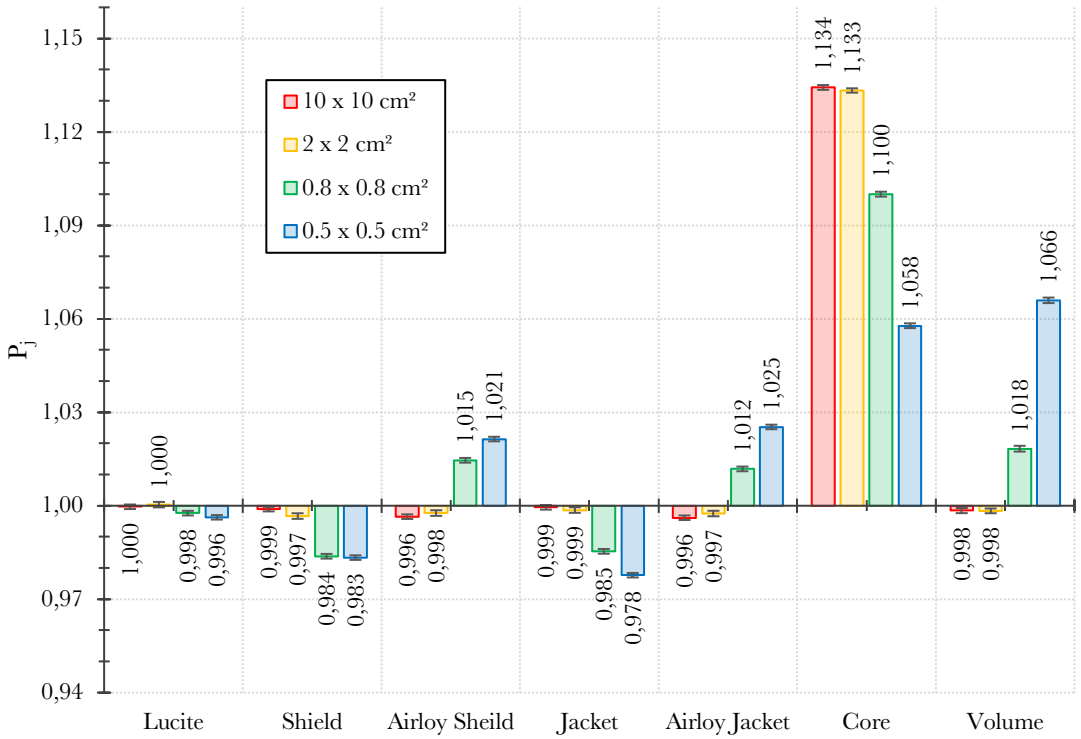


Figure 4.21: Layer perturbation factors for each layer of the probe at four different field size. The uncertainty bars represent the type A uncertainty with a coverage factor of $k = 2$.

From figure 4.21, it can be seen that the two largest individual perturbations come from the presence of the core and the volume averaging effect.

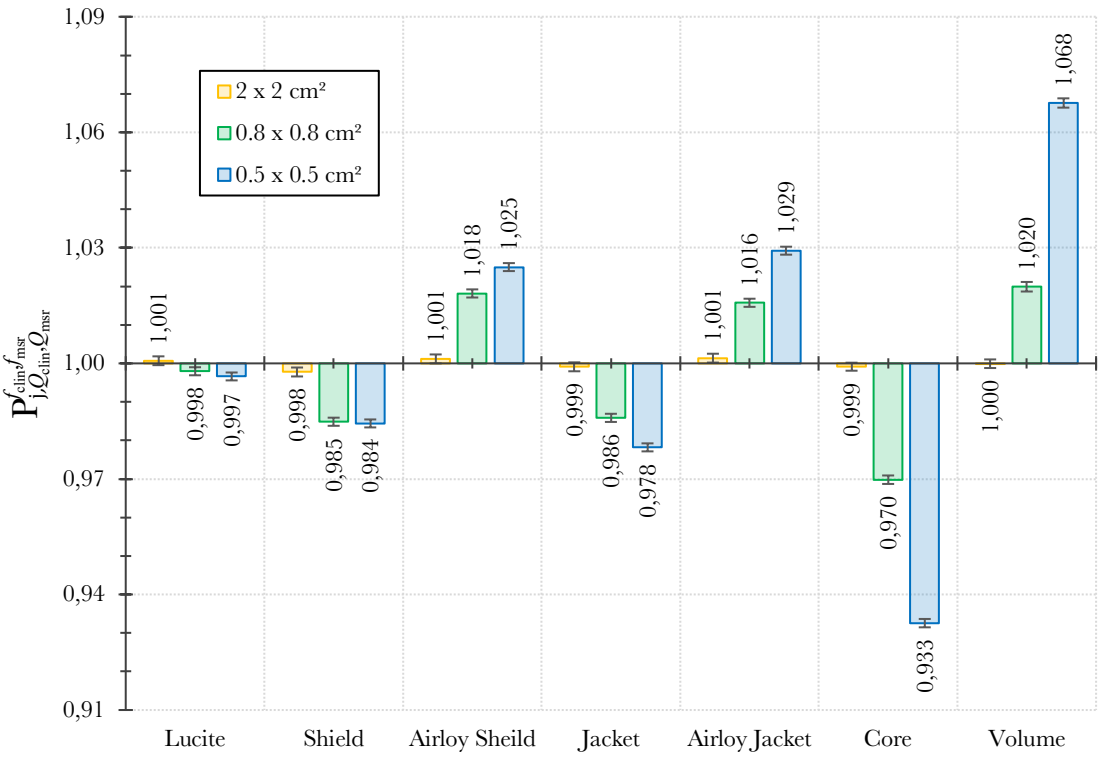


Figure 4.22: Relative layer perturbation factors for each layer of the probe at three different field size. The uncertainty bars represent the type A uncertainty with a coverage factor of $k = 2$.

## 4.7. Adiabatic heat simulation

The next aspect that was explored to gain a better understanding of the behavior of the probe under adiabatic operation was the heat transfer. A relatively simple model was proposed and implemented using a MATLAB code. This approximate model was based on a five-body geometry (core, jacket, shield, acrylic, and thin water layer), in which each body is represented by a single uniform temperature. Each body exchanges heat predominantly with the adjacent bodies, but the model allows heat exchange to occur between any pair of bodies. In addition to the graphite and acrylic layers of the probe, a

layer called "environment" was added to serve as a heat sink for the model; this is meant to represent the large volume of water contained within the phantom that surrounds the probe. Radiation-induced temperature rises were added to the model simulate the state of the bodies when irradiated. Each body was assigned a mass and heat capacity.

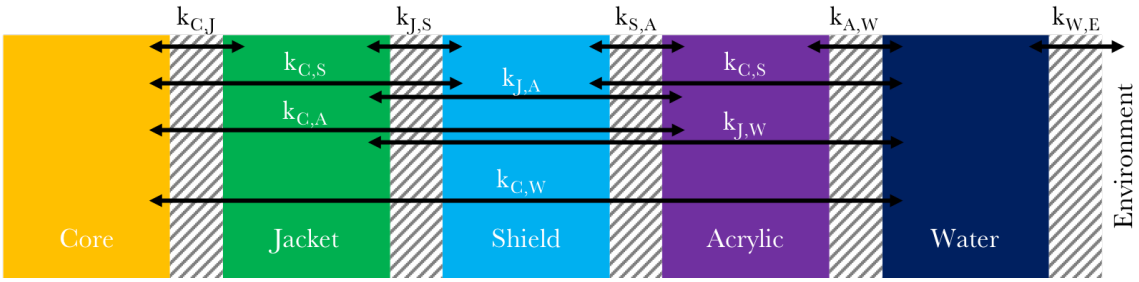


Figure 4.23: Five-body heat simulation model. Each body can exchange heat with every other body with a particular heat transfer rate constant.

The pre-irradiation temperature drifts were removed for each of the three graphite bodies for five identical adiabatic runs (10 MV FFF, 30 second irradiation, 2400 MU/min), and an average temperature curve was calculated for each body. The heat simulation was then calibrated against that data. By manually tweaking the heat exchange coefficients and the thickness of the water layer, the error between the simulation and the measurement was minimized for the core, jacket, and shield.

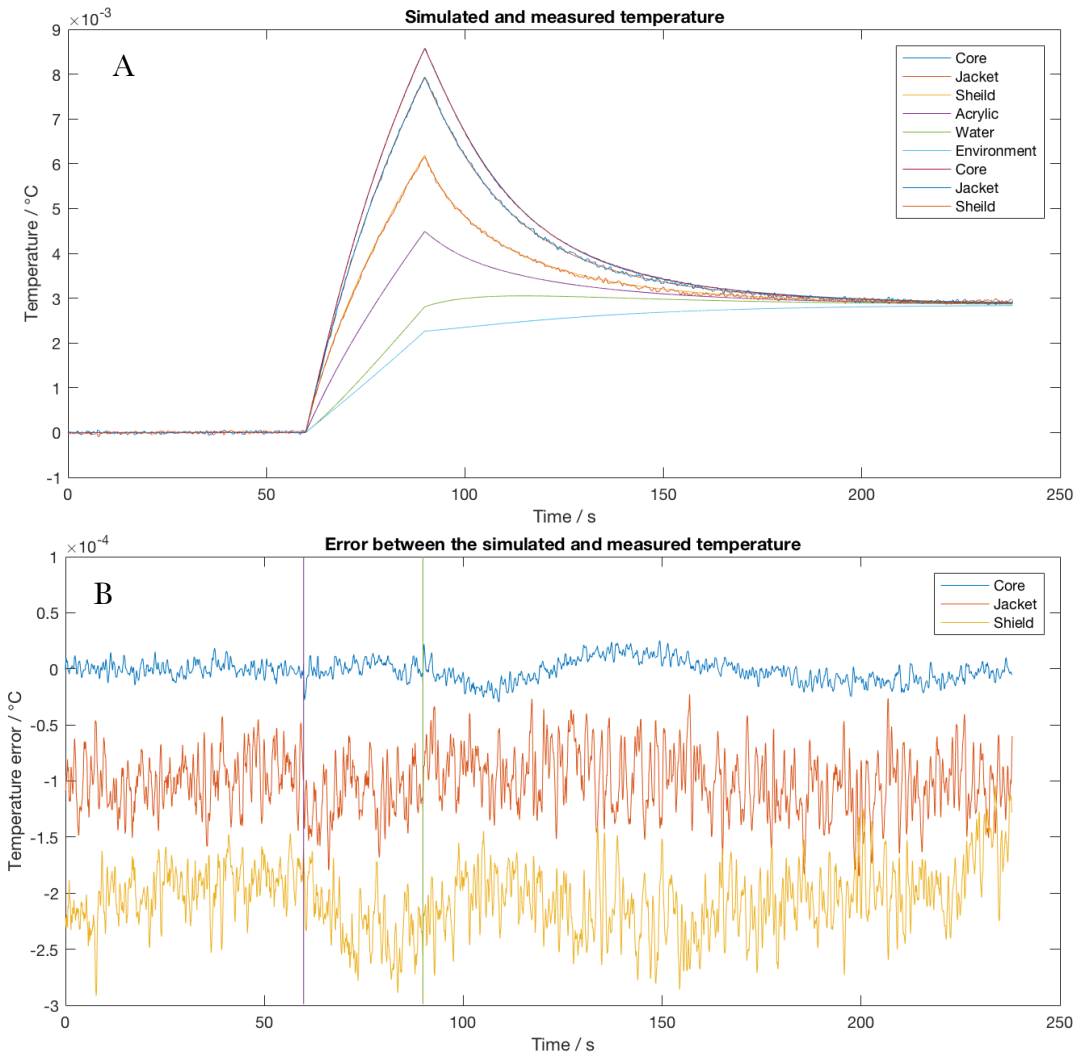


Figure 4.24: Heat transfer simulation in adiabatic mode for a 30 seconds irradiation of a 10 MV FFF photon beam at 2400 MU/min. (A) Simulated and measured temperatures as a function of time for each layer. (B) Difference between the simulated and the measured temperatures over time. The two vertical lines indicate the beginning and end of the irradiation. The jacket and shield data points were shifted down by $2 \times 10^{-4}$ and $4 \times 10^{-4}$ respectively for better visual. The average error value and standard deviation are $\bar{E}_{\text{core}} = 0.8$ µK, $\sigma_{\text{core}} = 9.4$ µK, $\bar{E}_{\text{jacket}} = 1.8$ µK, $\sigma_{\text{jacket}} = 26.6$ µK, $\bar{E}_{\text{shield}} = -3.1$ µK, $\sigma_{\text{shield}} = 28.6$ µK for the core, jacket, and shield respectively.

| Layer | Mass [ mg ] | Heat capacity [ J $kg^{-1}K^{-1}$ ] | $k_{i,i+1}$ [ mJ $s^{-1}$ $K^{-1}$ ] | $k_{i,i+2}$ [ mJ $s^{-1}$ $K^{-1}$ ] | $f_{ref}^{D_{core} \rightarrow D_w}$ |
|---|---|---|---|---|---|
| Core | 67.0 | 715 | 13.2 | 0.34 | 1.127 |
| Jacket | 66.7 | 715 | 10.2 | 0 | 1.128 |
| Shield | 190.6 | 715 | 29 | 0 | 1.139 |
| Acrylic | 224.6 | 1500 | 45 | 0 | 1.036 |
| Water | 462.0 | 4179 | 35 | 0 | 1 |

Table 4.10: Parameters used in the simulation presented in figure 4.24. $k_{i,i+1}$ refers to the heat exchange coefficient between the layer and the following layer (the next to the following layer in the case of $k_{i,i+2}$), e.g. $k_{i,i+1}$ of the core, is the heat exchange coefficient between the core and the jacket. Apart from the those presented in this table, all other heat exchange coefficients were set to 0.

As seen in figure 4.24, the simulated temperatures and the measured temperatures show relatively good agreement following the model calibration, except for a slight rise in the error during the cooling down portion of the signal. To further improve the level of agreement between the simulated and measured temperatures for the core, the jacket and the shield simulated temperatures were forced to equal the measured signal values, (i.e. the measured signals from the jacket and shield were used as the model input to determine the temperature in the core).

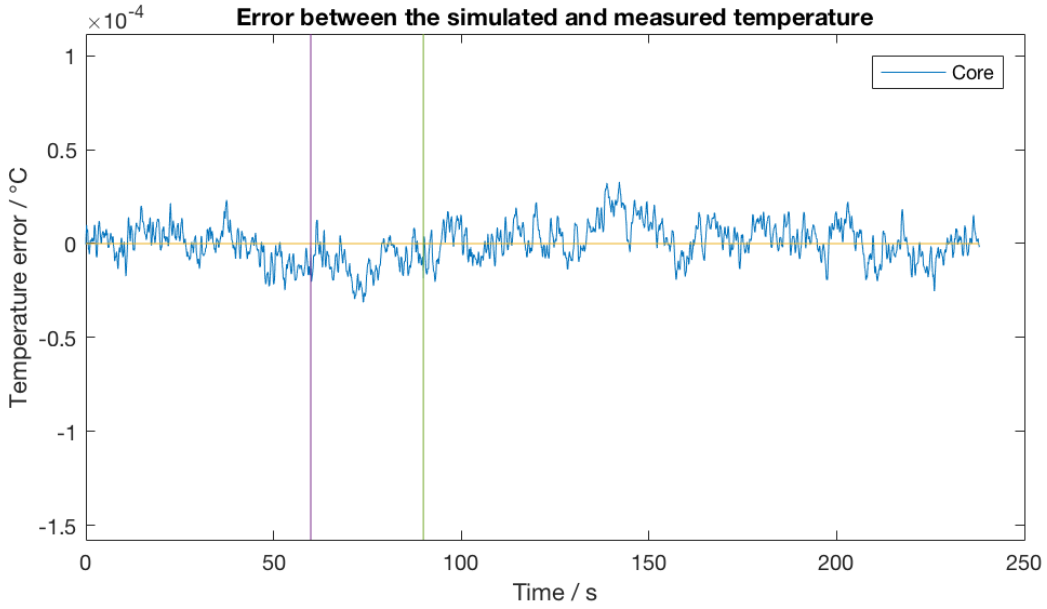


Figure 4.25: Heat transfer simulation of the adiabatic mode for a 30 second irradiation of a 10 MV FFF beam at 2400 MU/min for a 30 seconds irradiation. For this simulation, the experimental jacket and the shield signals were used as the model input. The graph shows the temperature difference between the simulated and the measured core temperatures as a function of time. The two vertical lines indicate the beginning and end of the irradiation. The input parameters of the model are the same as those listed in table 4.10.

The simulation in figure 4.25 shows very good agreement with the measurement, implying that the model is well calibrated against this experimental dataset. The model was then used to calculate the heat transfer correction for the experimental dataset acquired in section 4.5.2. (i) The simulated temperature curve (model output) was analyzed using the analysis method as described in section 4.5.2. (ii) The simulation was then re-run with all heat transfers turned off. The resulting output was again analyzed in the same way. The heat transfer correction was then calculated as the ratio of the doses determined in the two simulations, (ii)/(i). The doses calculated for (i) and (ii) were 8.548 Gy and 8.553 Gy, respectively, resulting in a correction factor of 1.001 ± 0.2 %. The uncertainty was estimated using a loose sensitivity analysis, a thorough verification is needed to improve the confidence of the uncertainty estimation.

4.8. References


1. Renaud, James, et al. "Aerrow: A probe-format graphite calorimeter for absolute dosimetry of high-energy photon beams in the clinical environment." *Medical physics* 45.1 (2018): 414-428.

2. Sarfehnia, A., et al. "Direct absorbed dose to water determination based on water calorimetry in scanning proton beam delivery." *Medical physics* 37.7Part1 (2010): 3541-3550.

3. Rogers, D. W. O., Kawrakow, I., Seuntjens, J. P., Walters, B. R. B., & Mainegra-Hing, E. (2003). NRC user codes for EGSnrc. *NRCC Report PIRS-702 (Rev. B)*.

4. Papaconstadopoulos, P., F. Tessier, and J. Seuntjens. "On the correction, perturbation and modification of small field detectors in relative dosimetry." *Physics in Medicine & Biology* 59.19 (2014): 5937.

5. Seuntjens, J., and D. W. O. Rogers. "Monte Carlo applications in measurement dosimetry." Clinical Dosimetry Measurements in Radiotherapy (2009): 147-80.

6. McEwen, Malcolm, et al. "Addendum to the AAPM's TG-51 protocol for clinical reference dosimetry of high-energy photon beams." *Medical physics* 41.4 (2014).

7. Almond, Peter R., et al. "AAPM's TG-51 protocol for clinical reference dosimetry of high-energy photon and electron beams." *Medical physics* 26.9 (1999): 1847-1870.

8. Palmans, H., P. Andreo P., Saiful Huq M., and Seuntjens J. "TRS-493: Dosimetry of Small Static Fields Used in External Beam Radiotherapy." *IAEA* (2017).

9. Kamio, Y., and H. Bouchard. "Correction-less dosimetry of nonstandard photon fields: a new criterion to determine the usability of radiation detectors." *Physics in Medicine & Biology* 59.17 (2014): 4973.

10. Auto-commissioning GOLDENBEAM, Mcgill internal report for the 6 MV, 6 MV FFF, 10 MV, and 10 MV FFF beam, Berryman A., Renaud M.-A.

## 5.1. Isothermal mode

As presented in section 4.1, the probe has exhibited an unexpected negative slope in the heating power curve during the beam-on period when operated isothermally. For this behavior to occur, heat exchange must be varying during the irradiation. This observed effect cannot be explained by a change in temperature, as the temperature of the graphite bodies (at the sensing point) are measured to be stable as shown in figure 5.1.

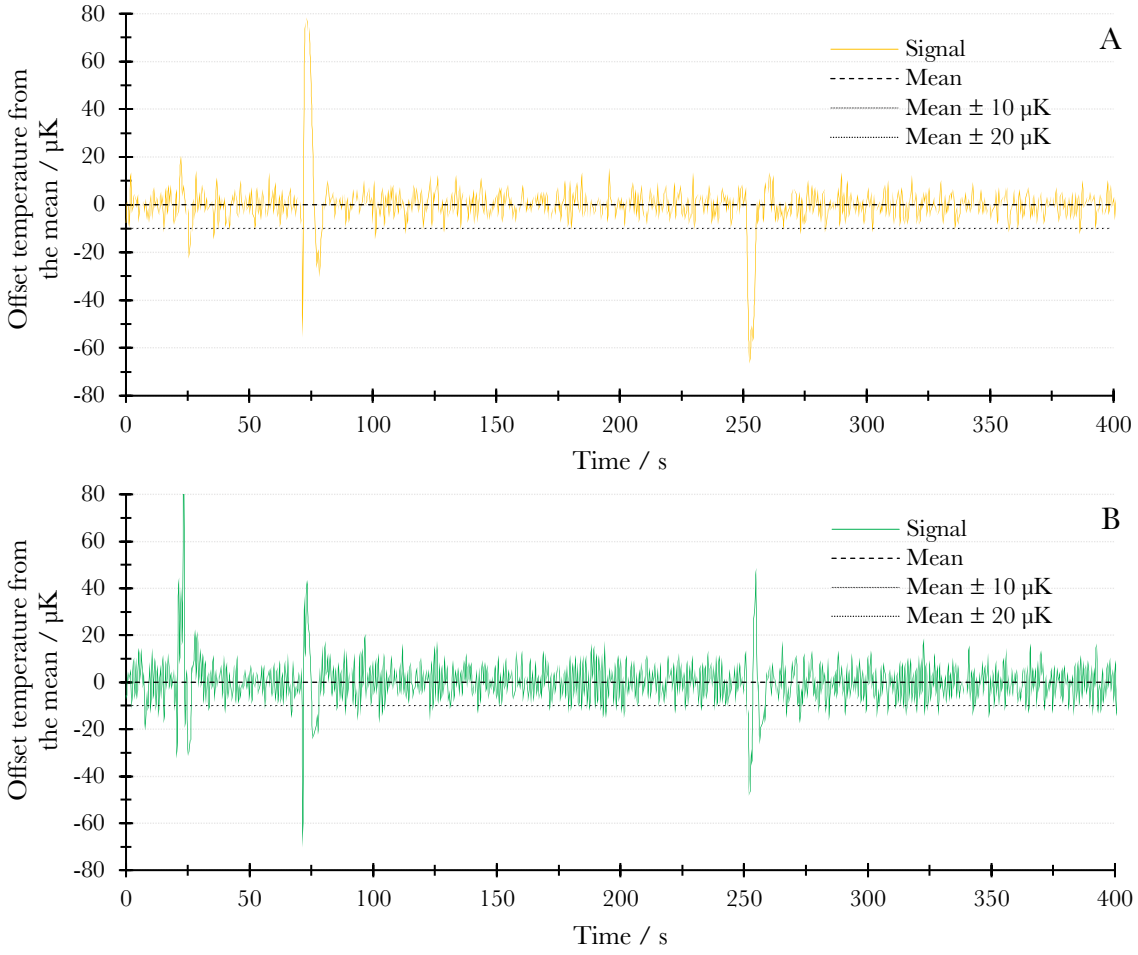

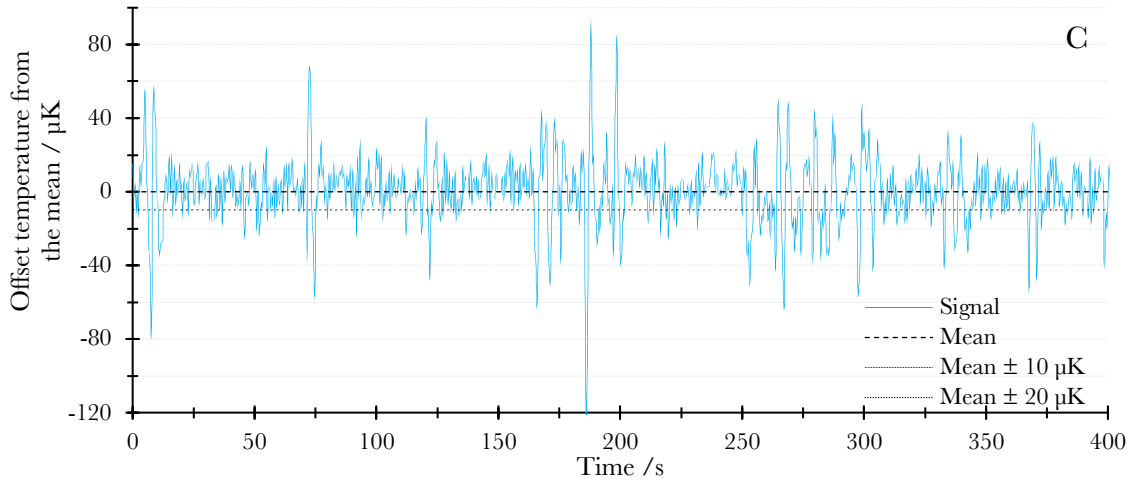


Figure 5.1: Offset temperature from the mean as a function of time in the (A) core, (B) jacket and (C) shield for a 6 MV beam at 600 MU/min, 1800 MU irradiation (run B, figure 4.2). A current on the order of 25 μA is passing through the sensing thermistors at all times. The standard deviation ($k$ = 1) of the temperature is 4.8 μK, 7.9 μK, and 17.6 μK for the core, jacket, and shield, respectively.

The temperature is not only measured to be stable in the core, but also in the jacket and shield. Furthermore, the negative slope on the heating power curve during the beam-on period is seen to occur in all three graphite bodies, with the greatest effect occurring in the shield (outermost body), and the least pronounced effect occurring in the core (innermost body; see Fig 5.2).

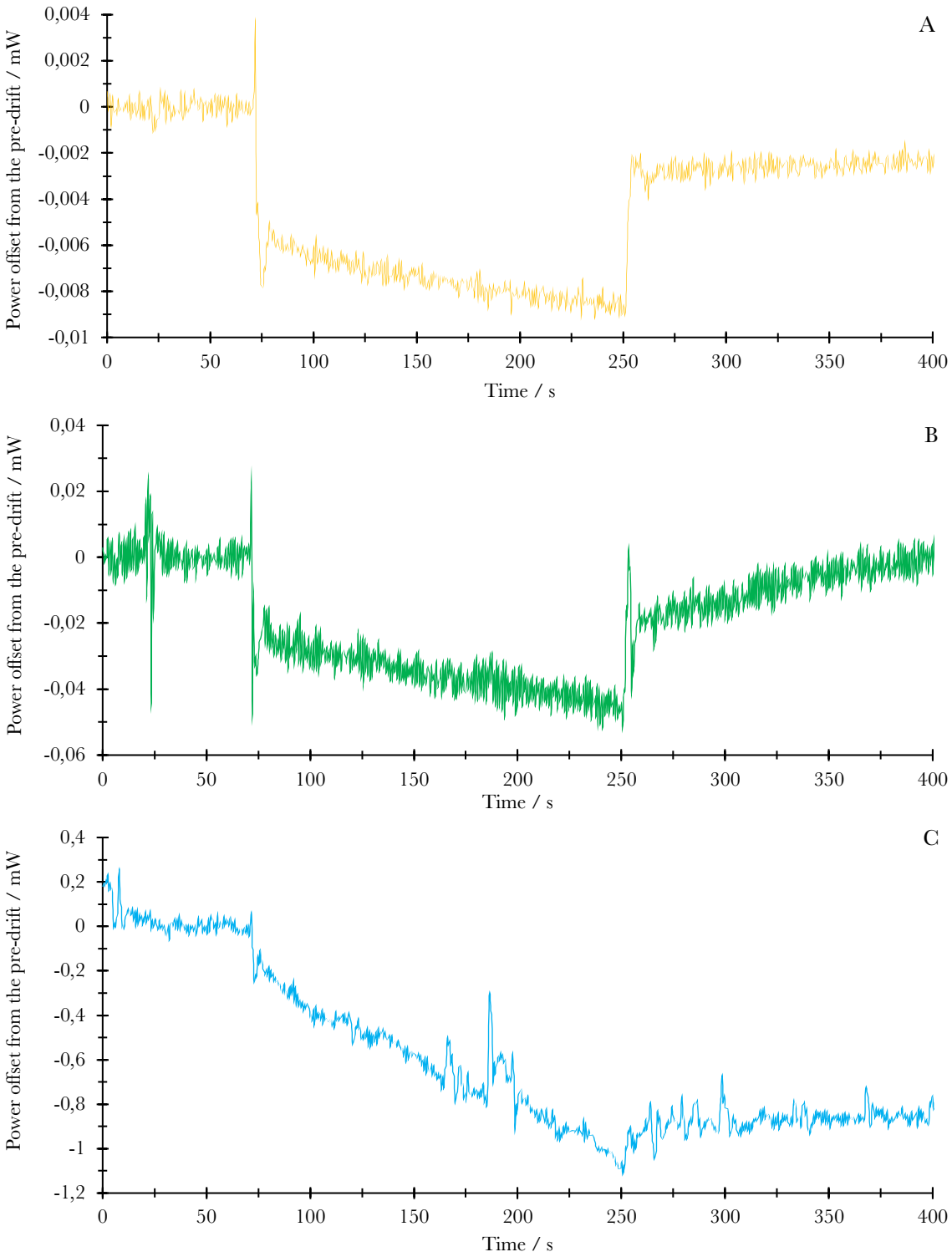


Figure 5.2: Heating power offset relative to the pre-drift as a function of time in the (A) core, (B) jacket and (C) shield for a 6 MV beam at 600 MU/min, 1800 MU irradiation (run B, figure 4.2).

While the beam is on, only the graphite bodies are being thermally controlled, everything that is outside of the shield heats up. This warming of the shield's environment is expected to result in a decrease in the slope in the heating power curve during the beam-on period. Unexpectedly, this environmental heating effect is apparently also influencing the heating power curves of the jacket and core. If the temperature of the shield was constant and uniform, this influence on the jacket and core would not be expected. Therefore, these results suggest that the temperature distribution in the shield is not uniform, and/or that the jacket is exchanging heat with the environment bypassing the shield (*e.g.*, through the thermistor leads and heating wires). To a lesser extent, the same can be said for the core; the jacket may not provide a uniform surrounding temperature for the sensitive volume and/or heat transfer is occurring between the core and the environment. Either of these two hypotheses could explain why the slope of the heating power for the core decreases during irradiation. In short, this behavior might be a sign of insufficient thermal isolation of the probe assembly from the surrounding environment as well as between adjacent graphite layers. Regarding thermal non-uniformity, physical joints between the caps and the cylindrical graphite pieces of the jacket and shield will result in a region of lower thermal conductivity (relative to the bulk graphite), thus contributing to thermal gradients in a given graphite body (*i.e.* in proximity to where the embedded heating and sensing occurs). Design modifications will be discussed in section 5.5.

## 5.2. Jacket and shield heating

Based upon what has been presented in sections 4.3 and 4.4, the in-graphite heating method that was chosen for the jacket and the shield should be reconsidered. Both heating circuits are effectively resistors in series; the circuit consists of the resistance of the leads

connecting the SMU to the probe, followed by the graphite resistance itself. This approach to heating involves a much lower resistance than compared to the core heating, which uses a thermistor as the resistive element (nominal circuit resistance: 18.8 kΩ, 217 Ω, and 23.7 Ω for the core, jacket, and shield, respectively). This means that the portion of the resistance external to the heating element represents a relatively larger proportion of the entire circuit resistance. For the core heating circuit, approximately 99.9 % of the heating occurs in the thermistor. Due to the lower and less stable resistances, the proportion of the total heating power dissipated in the jacket and shield is relatively more uncertain. Even though the power dissipated in jacket and shield are not used directly in the dose calculation, modeling and analysis of the probe's performance is made less certain.

The second observed issue with the probe's heating systems was the electrical coupling of the heating circuits (section 4.3). The data shows that the current flowing through a given heating circuit will affect the amount of current flowing in the other two heating circuits, and that the effect appears to be instant (to within the sampling frequency of 10 Hz). The nature of this behavior is not well understood, but similar phenomena have not been observed in previous probe prototypes, which all use thermistors as heating elements. Currently, it is not evident whether the effect is originating from within the probe assembly or in the outside circuitry. The cause of this effect is not expected to be thermal in nature, as heat production and exchange tend to occur with much longer time constants. One hypothesis to explain that phenomenon could be that the current passing through the graphite pieces can electrometrically induce current in the other circuit, but that has yet to be verified.

The third, and arguably most important issue, is the instability of the heating circuit resistance. Even though the PID controllers can account for slowly varying changes in resistance over time, the resistance changes observed in this work were at times too sharp to be fully compensated by the PID controller. This led to thermal instability within both the jacket and the shield, rendering accurate isothermal measurements impossible to perform. The integrity of the electrical contact between the embedded wire and the graphite is thought to be at least partially responsible for the resistance instability. If further developments are to revisit the in-graphite heating method, new methodologies will be required to ensure a reproducible and high-quality electrical contact is made to prevent the abovementioned issue.

### 5.3. Adiabatic mode discussion

As detailed in section 4.5, accurate dosimetry was performed using Aerrow-mini running in adiabatic mode. For both high-energy photon energies investigated, the measured doses to water agree with reference-class ionization chamber-based dosimetry methods to within 0.5 %. The uncertainties associated with the Exradin A1SL measurements were estimated and calculated using the recommended practices of the AAPM TG-51 addendum[3]. The uncertainties associated with Aerrow-based measurements are presented in table 4.6, which shows that the largest sources of uncertainty come from: (1) the graphite-to-water dose conversion factor calculated with Monte Carlo (0.4 %) and (2) the specific heat capacity of graphite, which has been estimated based on data in the literature (0.7 %). The combined standard uncertainty on the determination of dose to water associated with Aerrow in adiabatic mode is on par (~1 %) with that of an ionizing chamber. Further work to resolve

the issues surrounding isothermal operation are likely to reduce this figure to 0.7 %, the current estimated uncertainty associated with the large-format Aerrow.

The level of agreement between the Exradin A1SL and Aerrow-mini dose measurements supports the validity of the EGSnrc Monte Carlo model used in this work. Furthermore, the agreement shown in experiment suggests that the unconventional signal analysis methodology used in adiabatic mode has merit in situations where the absorbed dose rate is adequately constant. This approach was used out of necessity, as Aerrow-mini exhibited relatively large heat dissipation effects, resulting in a highly non-linear post-drift, that was incompatible with the conventional extrapolation methods. Though the dose rate approach is inherently approximate, it could be useful in other calorimeter designs that deal with similar heat dissipation effects, and ideally high, constant dose rates (e.g., industrial irradiators).

### 5.4. Monte Carlo simulations

Figure 4.20 shows that Aerrow-mini field output factor corrections in a 6 MV beam are within ± 1 % throughout the entire range of field sizes used in the clinic. According to the data showed in TRS-483[2], the same can be said only for plastic scintillator detectors.

Additional simulations can be performed to improve the understanding of the probe's behavior in small fields. Determination of the field output correction factors as a function of field size should be performed for other radiation qualities (e.g., cobalt-60 and 10 MV) and even for specific delivery modalities such as Gamma Knife™ and the Cyberknife™. Detailed impurity correction simulations should be performed at additional field sizes in

the range of 0.8 × 0.8 $cm^2$ to 5 × 5 $cm^2$ in order to gain a better understanding of how this correction varies with field sizes. A set of simulations could also be performed to investigate the effects of the probe depth and orientation (i.e. vertical vs horizontal) on the dose conversion factor and field output correction factors.

### 5.5. Future developments

A few key elements of the probe design should be modified to help resolve the issues surround the isothermal mode of operation. As discussed in section 5.2, the in-graphite heating method of the jacket and shield was shown to be problematic. Using thermistor as heating elements throughout the probe assembly would be a better option in the short term. For the shield, at least two thermistors (connected in series or in parallel) would be required to achieve a comparable power dissipation as the current Aerrow-mini prototype. To reduce the total number of thermistors required, the probe could be run at a temperature closer to ambient, thus reducing the heating power required to achieve and maintain a stable setpoint.

Another recommended change is to increase the thermal isolations of each graphite body. The results in this work suggest that the probe, in its current design, suffers from large heat dissipation effects, especially when present in a water phantom. Increasing the thermal isolation should somewhat reduce the magnitude of these thermal effects. This could be achieved by increasing the thickness to the aerogel, or by switching to a material with a lower thermal conductivity. One candidate material might be the newly available rigid aerogel formulation, Airloy® X56, made by Aerogel Technologies, LLC, which has a density of 0.3 $g/cm^3$ and a thermal conductivity of 23 mW $m^{-1}$ $K^{-1}$. A combination of the

two solution would be an optimal solution to increase thermal isolation. More detailed heat transfer modelling is required to optimize the design of the probe, which may result in a departure from the original Aerrow design proportional first proposed in 2011. In the case that heat dissipation effect could not be reduced to an acceptable level, in order to measure in isothermal mode, a slope commissioning could be a potential solution. By measuring an important number of runs and identifying the limits of the variation of the probe response, a correction on the signal could be applied to achieve better accuracy in the dose measurement. Surly the effect of the dependency on the environmental temperature and PID tuning would need to be quantified; the final accuracy would strongly depend on the order of those dependencies. Further developments could also look at changing the material of the sensitive volume to improve the response of the probe while maintaining a desirable behavior in small fields.

## 5.6. Conclusion

Throughout this thesis, it is been shown that the development of a mini-probe calorimeter has the potential to help meet the need for accurate dosimetry in small fields for radiotherapy clinics. The prototype developed in this work was unsuccessfully used in the isothermal mode, but a great deal of new information was acquired about the behavior and the performance of the probe under various conditions, furthering our understanding of the effects of miniaturization. Measurements were performed using Aerrow-mini in the adiabatic mode, an unanticipated avenue of research, that agreed with a calibrated ionization chamber to well within combined uncertainties. This accomplishment suggests that accurate dosimetry will also be possible in isothermal mode once the technical issues surrounding the heating systems are resolved.

5.7. References


1. Renaud, James, et al. "Aerrow: A probe-format graphite calorimeter for absolute dosimetry of high-energy photon beams in the clinical environment." *Medical physics* 45.1 (2018): 414-428.

2. Palmans, H. SP-0027: New IAEA-AAPM Code of Practice for dosimetry of small photon fields used in external beam radiotherapy. *Radiotherapy and Oncology* 119, (2016).

3. McEwen, Malcolm, et al. "Addendum to the AAPM's TG-51 protocol for clinical reference dosimetry of high-energy photon beams." *Medical physics* 41.4 (2014).